Design and Implementation of a Control Scheme for a MEMS Rate Integrating Gyroscope

A thesis submitted to Newcastle University for the degree of PhD in Mechanical Engineering

By

Stephen Richard Bowles

School of Mechanical and Systems Engineering

Faculty of Science, Agriculture and Engineering

October 2015

Abstract

MEMS gyroscopes are found across a large range of applications, from low precision low cost applications through to high budget projects that require almost perfect accuracy. MEMS gyroscopes fall into two categories – ‘rate’ and ‘rate integrating’, with the latter offering superior performance. The key advantage that the rate integrating type possesses is that it directly measures angle, eliminating the need for any integration step. This reduces the potential for errors, particularly at high rates. However, the manufacturing precision required is far tighter than that of the rate gyroscope, and this has thus far limited the development of rate integrating gyroscopes.

This thesis proposes a method for reducing the effect of structural imperfections on the performance of a rate integrating gyroscope. By taking a conventional rate gyroscope and adjusting its control scheme to operate in rate integrating mode, the thesis shows that it is possible to artificially eliminate the effect of some structural imperfections on the accuracy of angular measurement through the combined use of electrostatic tuning and capacitive forcing. Further, it demonstrates that it is viable to base the designs for rate integrating gyroscopes on existing rate gyroscope architectures, albeit with some modifications.

Initially, the control scheme is derived through the method of multiple scales and its potential efficacy demonstrated through computational modelling using Simulink. The control scheme is then implemented onto an existing rate gyroscope architecture, with a series of tests conducted that benchmark the gyroscope performance in comparison to standard performance measures.

Experimental work demonstrates the angle measurement capability of the rate integrating control scheme, with the gyroscope shown to be able to measure angle, although not to the precision necessary for commercial implementation. However, the scheme is shown to be viable with some modifications to the gyroscope architecture, and initial tests on an alternative architecture based on these results are presented.

Acknowledgements

First and foremost, I would like to thank my supervisory team, Dr BJ Gallacher and Dr ZX Hu for their immense help and support over the course of this project. My heartfelt thanks also go out to United Technologies and Systems for providing the funding for this project, and in particular Chris Gregory, Kevin Townsend and Chris Fell for offering their help and expertise throughout the duration of the project. Furthermore, thanks must be offered to the Microelectronics research group at Newcastle University, members of which have offered considerable help and pastoral support throughout my studies.

Finally, and perhaps most importantly, my thanks go to my parents, Linda and Robert, who have never faltered in their support throughout my education, without which I would undoubtedly have found it impossible to achieve what I have thus far.

Table of Contents

Table of figures

Chapter 1. Introduction

1.1. Project background

Gyroscopes in one form or another have existed for thousands of years, primarily as toys similar to the modern 'spinning top'. Over the course of the past 250 years or so they have been developed for use in instrumentation, beginning with John Serson's Whirling Speculum in 1743, which was used on ocean vessels as a level in poor visibility [1]. Following the invention of the electric motor and therefore a method for sustaining the rotation of a rotor, the late 19th century saw gyroscopes being used in their more familiar role as heading indicators.

However, it was not until the 20th century that their value in navigational applications was fully realised, with them becoming standard components in aircraft and naval systems by World War Two [2]. Following this, the development of unmanned weapons systems, such as ballistic missiles, and their requirement for reliable accurate instrumentation led to gyroscopes being continually miniaturised.

Currently, the smallest gyroscopes available are on the MEMS (microelectromechanical systems) scale and can be found in a large range of consumer electronics such as mobile telephones, video game console controllers and virtual reality headsets, as well as car safety systems and other lower-accuracy applications [3-5]. However, the difficulty in producing a MEMS gyroscope with sufficient measurement precision for military grade measurements currently precludes most current-generation MEMS gyroscopes from such applications.

Due to their potential for inexpensive mass production coupled with small size and high accuracy, there is currently a large amount of work being focussed on the development of tactical grade MEMS gyroscopes. Such a requirement has given rise to this project, which looks to tackle some of the issues surrounding the production of high-accuracy MEMS gyroscopes.

1.2. Gyroscope design

The gyroscope on which this thesis is based has been provided, pre-packaged, by Atlantic Inertial Systems. It consists of a silicon-on-glass ring surrounded by a series of eight equally-spaced electrodes, where the use of silicon-on-glass is common for MEMS gyroscopes due to

the low parasitic capacitances resulting from the manufacturing process [6]. Inside the ring, there are sixteen equally-spaced electrodes used for tuning the resonant frequency of the two modes of vibration that measure the rotation applied to the gyroscope, the method behind which will be discussed later in this chapter.

The gyroscope is constructed using the Deep Reactive Ion Etch bulk silicon process, which is a process that allows deep, steep-sided holes to be etched into wafers [7]. The construction of the gyroscope is such that there are no gaps in the structure that can result in stiction adversely affecting the performance of the gyroscope [8].

Figure 1.1 shows the gyroscope design and electrode layout, with the red electrodes being used to excite and measure two modes of vibration in the ring via capacitive forcing and sensing, and the blue electrodes used to tune the resonant frequencies of the gyroscope's modes of vibrations, a procedure described further in section 4.3.1.

The drive and sense electrodes are 'paired up'. That is, there are two pairs of electrodes that excite the two modes of vibration, with the two electrodes in each pair placed opposite one another across the ring diameter. Note that the physical coordinates q_1 and q_2 are chosen such that they are aligned with the modes of vibration of the gyroscope, (i.e. they bisect the two electrode pairs that are used to excite modal vibration). Each pair of sense electrodes is placed such that it is at 90° to its corresponding mode of vibration.

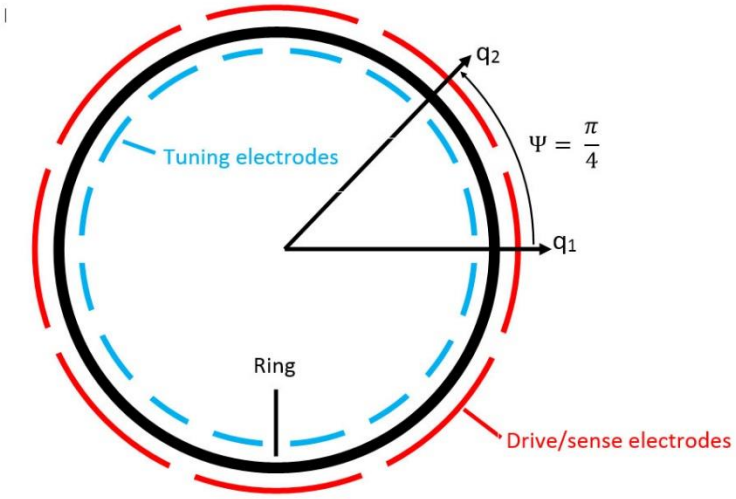

Figure 1.1 - The gyroscope electrode layout with physical axes, where the red electrodes act as drive and pick-offs electrodes while the blue are used for electrostatic tuning

Figure 1.2 is a diagram of a quarter of the ring and details the key dimensions of the gyroscope, where b is the ring width, R its radius and h_0 the gap between the drive and sense electrodes and outside edge of the ring. Note that for clarity the tuning electrode gap has not been included in the diagram, but this is equal to h_0.

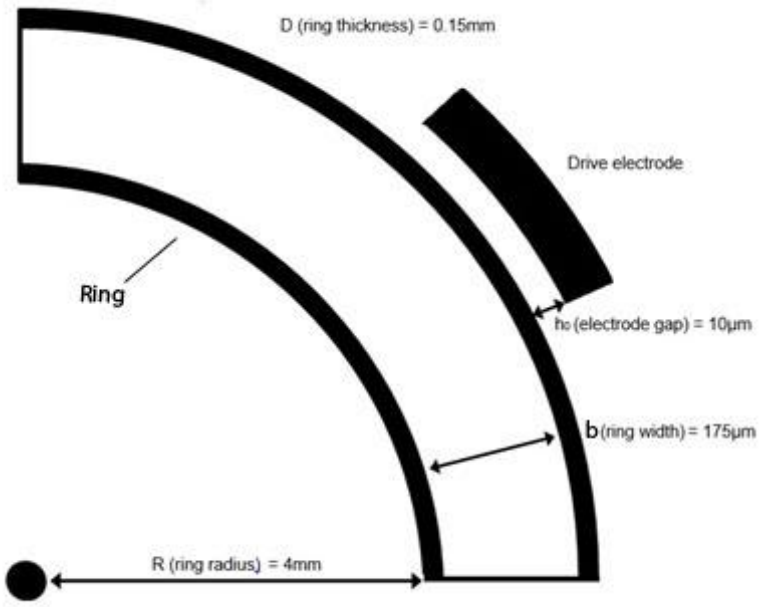

Figure 1.2 – A quarter section of the ring with key gyroscope dimensions

1.3. Operating principles

MEMS gyroscopes utilise Coriolis forces to measure changes in angle and angular rate. Coriolis forces arise within rotating reference frames and are best described by considering an object travelling laterally over a rotating reference frame. From a viewpoint outside of the reference frame, the object travels in a straight line. However, from a viewpoint within the rotating reference frame the object appears to take a curved path, as demonstrated by figure 1.3, which shows a reference frame rotating anti-clockwise, with the trajectory of an object travelling across it represented by a blue arrow and a viewpoint on the object represented by a red dot.

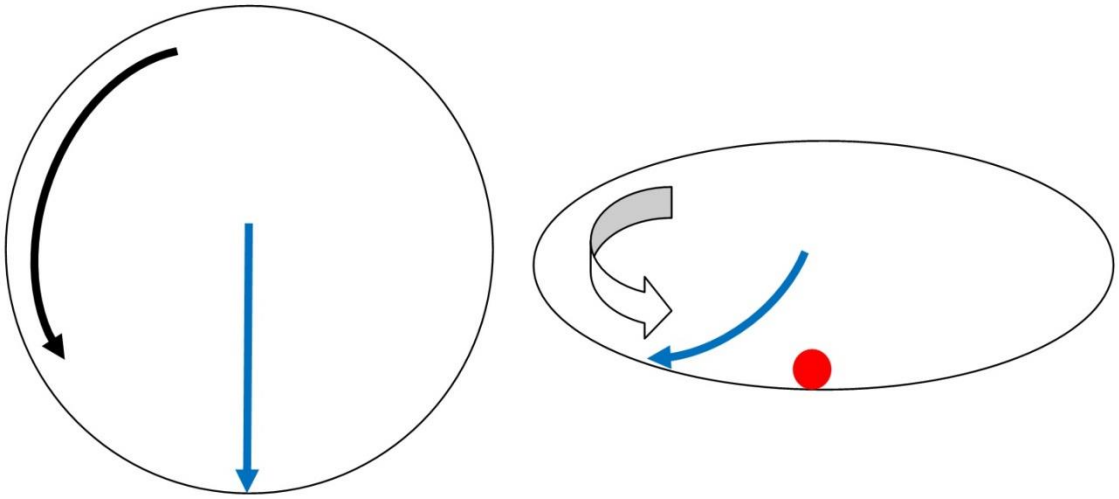

Figure 1.3 - The apparent movement of an object over a rotating surface (blue arrow) when viewed from a non-inertial (i.e. above) reference frame (L) and an inertial (i.e. a point on the disk, red dot) reference frame (R)

Coriolis forces account for this apparent curvature and can be shown to be related to the angular velocity squared [9]. A detailed mathematical description of this behaviour for a three-axis vibrating gyroscope is given in [10] but, following similar principles for a single axis gyroscope, it will be presented here in brief.

The radial and tangential displacement of a point on the centreline of a vibrating ring, u and v respectively, can be shown to be of the form, where q_j represents the contribution of mode j to the motion:

$$u = q_1 \cos n\theta + q_2 \sin n\theta \quad (1.1)$$

$$v = -\frac{1}{n}(q_1 \sin n\theta + q_2 \cos n\theta) \quad (1.2)$$

These can then be used to derive the radial, tangential and axial components of the displacement of a point on the centre of mass of the ring, which for a ring with no axial movement is given by $\underline{r}$, while the rate of turn around the z-axis for the same ring is provided by $\underline{\Omega}$:

$$\underline{r} = (u, v, 0)^T \quad (1.3)$$

$$\underline{\Omega} = (0, 0, \Omega_z) \quad (1.4)$$

These can then be used to calculate the absolute velocity of the centre of mass of any section of the ring, V_s, and this can in turn be used to derive the kinetic energy of the uniform ring, T,

as rotation is applied, where *R*, *b* and *D* correspond to the physical dimensions ring radius, width and thickness, and ρ is the ring density.

$$\underline{V_s} = \underline{\dot{r}} + \underline{\Omega} \times \underline{r} \tag{1.5}$$

$$T = \frac{1}{2}\rho RbD \int_0^{2\pi} \underline{V_s} \cdot \underline{V_s}\, d\theta \tag{1.6}$$

The elastic strain energy for a perfect ring, *V*, is given in equation 1.7. By applying Lagrange's equation with the Lagrangian $L = T - V$, the equations of motion in equation 1.8 can be derived [10, 11]. In these cases, I_{zz} is the polar second moment of area, *E* is the elastic modulus of the ring and the term $\underline{F_D}$ corresponds to electrode forcing along the modes and will be explained later, while m_0, ω_0, ζ_0, *n* and k_0 represent the normalised mass, natural frequency, damping ratio, number of modes and stiffness, respectively.

$$V = \frac{I_{zz}E}{2R^3} \int_0^{2\pi} \left(\frac{\partial^2 u}{\partial \theta^2} - \frac{\partial v}{\partial \theta} \right)^2 d\theta \tag{1.7}$$

$$m_0 \underline{\ddot{q}} + 2m_0\{\zeta\omega_0 - G\}\underline{\dot{q}} + k_0 \underline{q} = \underline{F_D} \tag{1.8}$$

where:

$$G = \begin{bmatrix} 0 & k\Omega \\ -k\Omega & 0 \end{bmatrix} \qquad k = \frac{2n}{(n^2+1)}$$

The angular rate appears in the matrix *G*, and it can be noted that it is derived from the calculation of the ring kinetic energy. This is the manifestation of the Coriolis forces. It should be noted here that acceleration terms Ω^2 and $\dot{\Omega}$ also occur, but have been neglected from the analysis as they are of second order magnitude, and thus unlikely to make any significant difference to the performance of the gyroscope.

When applied to MEMS vibratory gyroscopes, these Coriolis forces can be shown to affect the vibration pattern in one of two ways. The most common method of exploiting these forces is with the 'rate' mode, whereby the gyroscope is excited into one mode of vibration. On rotation, Coriolis forces arise and excite the second mode of vibration orthogonally to the first and, by measuring either the amplitude of this vibration or the force required to null it, it is possible to measure the angular rate of the gyroscope, which is proportional to these

parameters. However, in order to gain a measurement of angle integration of the angular rate is required, and this can introduce large errors.

The ‘rate integrating’ mode of operation requires two orthogonal modes of vibration to be simultaneously excited. As Coriolis forces arise on rotation, they cause a ‘beating’ energy transfer between the two modes, the frequency of which is proportional to the angular rate and angular displacement. This beating is demonstrated in the modelling in section 5.1. The proportionality between the frequency of this beating, which is measurable using the pick-off electrodes, and the angular displacement provides a method for the direct measurement of angle.

1.4. Effect of gyroscope imperfections

The rate integrating gyroscope relies on cross-coupling between the two modes of vibration to produce the beating pattern from which the measurement of angular rate and displacement is obtained. Within a perfect gyroscope Coriolis forcing is the sole cause of such cross-coupling, and hence the only source of energy transfer between the two modes of vibration.

However, current manufacturing practices limit, to a varying degree, the precision with which gyroscopes can be constructed. As such, gyroscopes suffer from imperfections that cause uneven behaviour, and therefore coupling, between the two modes of vibration. This coupling subsequently interferes with that caused by the application of rotation and subsequent energy transfer – as the energy transfer is no longer caused only by the rotation of the device, its frequency is no longer proportional to the rate or angle of rotation.

Although it is possible to remove many of these imperfections post-production, either through manufacturing techniques such as laser ablation or in situ techniques, such as electrostatic tuning, it is not currently possible to remove all imperfections. As such, they must be accounted for and minimised by a control system.

These imperfections can be represented by perturbations in the density and elasticity of the ring, represented as angle-dependent Fourier series:

$$\rho(\theta) = \rho_0 + \sum_{m}^{\infty} \rho_{mc} \cos m\theta + \sum_{m}^{\infty} \rho_{ms} \sin m\theta \quad 1.9$$

$$E(\theta) = E_0 + \sum_{h}^{\infty} E_{hc} \cos h\theta + \sum_{h}^{\infty} E_{hs} \sin h\theta \quad 1.10$$

This leads to the kinetic and elastic strain energy being defined as:

$$T = \frac{1}{2} RbD \int_0^{2\pi} \rho(\theta) (\dot{u}^2 + \dot{v}^2) d\theta \quad 1.11$$

$$V = \frac{I_{zz}}{2R^3} \int_0^{2\pi} E(\theta) \left(\frac{\partial^2 u}{\partial \theta^2} - \frac{\partial v}{\partial \theta} \right)^2 d\theta \quad 1.12$$

By substituting appropriately it becomes possible to derive mass, damping and stiffness matrices, the terms of which represent deviations in these parameters from the ideal ring for each mode of vibration [11]:

$$[M] = m_0 \begin{bmatrix} 1 + \overline{\delta}_1 & \overline{\delta}_2 \\ \overline{\delta}_2 & 1 - \overline{\delta}_1 \end{bmatrix} \quad 1.13$$

$$[\hat{C}] = 2m_0 \omega_0 \zeta_0 \begin{bmatrix} 1 + \overline{\gamma}_1 & \overline{\gamma}_2 \\ \overline{\gamma}_2 & 1 - \overline{\gamma}_1 \end{bmatrix} \quad 1.14$$

$$[K] = k_0 \begin{bmatrix} 1 + \overline{\mu}_1 & \overline{\mu}_2 \\ \overline{\mu}_2 & 1 - \overline{\mu}_1 \end{bmatrix} \quad 1.15$$

where:

$$m_0 = \pi \rho_0 RbD \left(1 + \frac{1}{n^2}\right) \qquad k_0 = \frac{E_0 I_{zz} \pi}{a^3} (1 - n^2)^2 \qquad \overline{\mu}_1 = \frac{E_{4c}}{2E_0} \qquad \overline{\mu}_2 = \frac{E_{4s}}{4E_0}$$

$$\overline{\delta}_1 = \left(\frac{n^2 - 1}{2(n^2 + 1)} \right) \frac{\rho_{4c}}{\rho_0} \qquad \overline{\delta}_2 = \left(\frac{n^2 - 1}{2(n^2 + 1)} \right) \frac{\rho_{4s}}{\rho_0}$$

The application of these matrices is discussed further in section 3.1.1. Due to the precision of the manufacturing processes, it can be assumed that $\rho_{4c} << \rho_0$, $\rho_{4s} << \rho_0$, $E_{4c} << E_0$ and $E_{4s} << E_0$ and, as such, the matrices containing these terms can be considered to be small.

1.5. Project aims

This project demonstrates a control scheme to produce a rate integrating MEMS gyroscope using the architecture described in section 1.2. It will shortly be shown that the primary objective of the control scheme will be to remove the effect of stiffness imperfections on the measurement of angle.

The control scheme described is based upon a perturbation analysis of the gyroscope, using the slow time equations of motion to describe changes in the envelope of vibration as rate is applied. The imperfections also manifest themselves in the behaviour of this envelope, allowing their effect to be measured and therefore reduced through the application of an appropriate control scheme.

The gyroscope behaviour has been described in terms of orbital elliptic parameters, which are in turn composed of invariants that are derived from the real and imaginary responses of the sense electrodes for each mode of vibration. The reasoning behind this is that these parameters can be directly related to total gyroscope energy, level of modal mistuning, angle of gyroscope rotation and the phase of vibration. Consequently, they provide the parameters necessary to define the gyroscope behaviour using measurable parameters and hence develop a control scheme.

Experimental results are provided to support the underlying theory, with these demonstrating the efficacy of the various elements of the control scheme. Primarily they show that, with appropriate development, the control scheme proposed is a viable way of measuring angle using a rate integrating MEMS ring gyroscope. The results also offer an insight into problems with implementing the control scheme derived that must be overcome prior to any commercial production.

A full characterisation of the gyroscope is also undertaken with it operating in rate integrating mode, with the control scheme operated in what is deemed to be the most suitable manner for the gyroscope architecture.

Finally, a novel gyroscope architecture is presented that can be used to overcome the problems encountered during the control scheme development. Initial experimental results are presented, and in particular the potential ease in reducing the modal mistuning is demonstrated.

Chapter 2. Literature Review

2.1. Vibratory gyroscopes

The vibratory gyroscope is a well-established piece of technology, having been commercially available since the 1980s [12]. However, their principles of operation were established as early as 1890, when G.H. Bryan described the changing of beats in a ringing wine glass when it is exposed to rotation [13].

There are a number of designs for vibratory gyroscopes, including the tuning fork [14], vibrating shell gyroscope [15] , ring gyroscope [11] and a variety of suspended-mass gyroscopes [16, 17]. However, all gyroscopes utilise the same underlying principles, whereby Coriolis forces that arise upon rotation cause a change in the vibration pattern of the gyroscope.

Traditionally, this property has been exploited by driving the gyroscope into one mode of vibration. The emergence of Coriolis forces on rotation results in a second orthogonal mode of vibration arising, the amplitude of which is proportional to the rate of rotation. Integration of this to find angular displacement, however, can lead to errors in the calculation of angle [12].

A second application of these principles is in using the Coriolis forces to produce energy transfer between the two modes of vibration. This transfer can be measured, and the frequency of the beating pattern it takes can be shown to be proportional to the rate and angle of rotation, allowing a direct calculation of angle and eliminating the need for numerical integration. Gallacher [11] provides a thorough description of this behaviour.

As well as their use as standalone instruments, gyroscopes can be combined with other devices, such as accelerometers and GPS systems, to provide a highly-refined motion measurement system [18]. However, such a system is beyond the focus of this thesis.

2.2. Elliptic coordinates

Friedland and Hutton [19] discuss a method for describing the motion of a gyroscope in the Cartesian coordinate frame in terms of orbital elliptic parameters. These parameters consist of the length of the semi-major and semi-minor axis of an ellipse, the angle the ellipse makes with respect to the Cartesian coordinate system defined and the orbital phase, a quantity that

describes the position of a point on the perimeter of the ellipse. In their paper, Friedland and Hutton demonstrate that the length of the semi-major axis, *a*, is analogous to the total energy of vibration, while the length of the semi-minor axis, *b*, is equivalent to the orbital momentum. Hence, where *b* is zero, *a* corresponds to the trajectory of vibration, while any change in angle of the ellipse, φ, is proportional to the angle of rotation of the gyroscope when a rate is applied.

Lynch [20] takes this further by proposing a control system whereby such parameters are described by a series of invariants. These invariants are the components of each mode of vibration that are in-phase and out-of-phase with a reference signal. As such, the orbital elliptic parameters are defined in terms of quantities that can be extracted from existing gyroscope architectures. Lynch goes so far as to suggest a control system and describe the forcing required to enact this, however he provides no experimental work to demonstrate its application. However, numerous works have made use of such invariants with varying degrees of success.

Painter and Shkel [21] describe a system that uses a feedforward control akin to electrostatic tuning to remove large structural imperfections, before using a feedback system that applies forcing to null any perturbations that arise during gyroscope operation. The authors note that a dual-stage system such as this is necessary to prevent the feedback control having too great an impact on the precession information. Using Principal Component Analysis, it is shown that feedback controls nevertheless introduce a small error to the device.

2.3. Tuning

For successful operation, it is a necessity that the difference between the resonant frequencies of the two modes of vibration is as small as possible before the application of any control system to reduce the effect of this mistuning. Although this can be done during post-production using a method such as ion-beam trimming, this is undesirable as it causes irreversible changes to the device [22]. As such, a tuning method that can be conducted in situ is highly desirable.

A well-established method to reduce the mistuning without making physical alterations to the device is to use electrostatic tuning or similar [21-23]. This method has routinely been shown to be effective in tuning gyroscopes. The method in [22] in particular details the challenges

and methods behind electrostatic tuning – using the same gyroscope architecture as that used in this project it also proves to be particularly relevant.

By combining electrostatic tuning with novel methods of tuning such as feedback control, recent results have shown tuning to be possible to within tens of mHz [24].

Further to the modal mistuning described, the gyroscope drive signal must operate at the correct frequency. It has been shown that this can be achieved using a conventional phase locked loop, whereby phase information is used to adjust drive frequency by means of a PID or similar controller in order to drive the gyroscope at its resonant frequency [25].

2.4. Performance criteria

2.4.1. Performance measurement criteria

Gyroscope accuracy is assessed according to common criteria, and these are best described in the IEEE Specification and Test Procedure for Coriolis Vibratory Gyroscopes [26]. Although described in more detail later in section 7.2 they will be briefly discussed here.

Bias stability and angle random walk are derived from a plot of the Allan variance of the gyroscope output. Bias instability measures the minimum stability of the gyroscope bias and is the minimum point on the Allan variance curve, and it is a measure of the gyroscope's stability over long averaging times. The angle random walk is a measure of output noise, and is defined as the Allan variance for an averaging time of 1s.

Scale factor is a measure of how closely the output angle of the gyroscope matches the input, thus a scale factor of 1 is ideal, and this should be constant for all rates. Linearity determines the consistency of the scale factor, in that it is a measure of how linear the response is as the input angle is increased. Bandwidth is a measure of the maximum frequency of data that can be processed by the gyroscope, whilst asymmetry describes any difference between the accuracy of the measured output for positive and negative rotation.

By combining these criteria, it is possible to assess the application of a gyroscope, with the gyroscope being categorised accordingly. Although the precise classification scheme can vary between manufacturers and other institutions, vibratory gyroscopes can be broadly separated into three areas - 'rate', 'tactical' and 'inertial' [27].

Rate gyroscopes are used for low precision applications, where large drift and low measurement accuracy can be tolerated (e.g. consumer electronics) whilst tactical grade gyroscopes are of the rate integrating type and can be shown to exhibit considerably enhanced performance characteristics, with their enhanced bandwidth and lower drift being particularly notable. Finally, inertial grade gyroscopes exhibit minimal drift and performance characteristics close to the ideal, and are used where accuracy is of paramount importance (e.g. long term navigation), with the trade-off being higher cost for the equivalent portability [28].

2.4.2. Performance benchmarks

Table 2.1 provides a summary of the approximate performance benchmarks generally attributed to the gyroscope grading system [27]. However, these specifications do not cover linearity error or bias instability, so averages of existing specifications for rate integrating gyroscopes, such as those found in [17, 29-31], are presented in table 2.2.

	Rate	**Tactical**	**Inertial**
Angle random walk ($°/\sqrt{hr}$)	> 0.5	0.5 - 0.05	< 0.001
Bias drift (°/hr)	10 - 1000	0.1 - 10	< 0.01
Linearity (%)	0.1 - 1	0.01 – 0.1	< 0.001
Bandwidth (Hz)	70	100	100

Table 2.1 - The specifications for the three grades of gyroscope

Parameter	**~~Measurement~~ Average**
Bias instability (°/hr)	7.5

Table 2.2 - Additional specifications for a rate integrating gyroscope

2.5. Existing control schemes

Park, Horowitz and Tan [32] provide a thorough review of the dynamics of a rate-integrating gyroscope, providing a proposal for a control scheme that utilises a damping control that matches the energy of both modes coupled with a force balance control to eliminate stiffness inequalities between the two modes of vibration. Simulation results demonstrate the effectiveness of the scheme, although no experimental results are presented.

While Painter and Shkel [21] use orbital elliptic parameters to describe the motion of the device, Pridhodko et al [17] demonstrate the use of the parameters to develop a control system utilising a gyroscope design based on four coupled proof masses, but with the same underlying dynamics to the ring gyroscope so far discussed. The paper measures the accuracy of the gyroscope acting in rate-integrating mode under free vibration, (i.e. there is no sustaining force). However, the control scheme only implements electrostatic tuning, and does not apply a feedback control.

The authors report a bandwidth of 100Hz, with a linearity of 0.4% and a theoretical angular drift of $1°hr^{-1}$, demonstrating a gyroscope with low-end tactical grade performance. While it demonstrates the accuracy of the rate-integrating mode of operation, the lack of a sustaining force means that this gyroscope design is not yet suitable for implementation.

Similarly, the paper by Tatar et al. [33] describes the elimination of errors caused by stiffness imperfections through the use of electrostatic tuning, when applied to a rate gyroscope. It employs a quadrature control loop to adjust the applied tuning voltages with the objective of sustaining the sense mode amplitude at zero. These are then compared to FEM results. The paper finds agreement between FEM analysis of the gyro and experimental test results, reporting an angle random walk, bias instability and linearity of $0.014°h^{-0.5}$, $0.39°hr^{-1}$ and 0.0001%, respectively.

Despite promising results that would place the gyroscope towards the inertial grade end of the spectrum, the paper describes such a control scheme in reference to a rate-type gyroscope.

Rate-integrating gyroscopes have a much tighter error tolerance, requiring a modal mistuning of the order of mHz [24]. The gyroscope reported in the paper has a modal mistuning of 130Hz following the application of the quadrature control loop and as such the research conducted is not relevant to the development of a rate integrating gyroscope control scheme

as it does not consider the important advantages of the rate integrating gyroscope type, for example enhanced bandwidth. While the level of modal mistuning attained in this paper is not of the order of that required for a rate integrating gyroscope, it demonstrates the potential that electrostatic tuning offers in the reduction of the effect of stiffness imperfections.

Gregory et al [34], however, use a system similar to that suggested by Lynch, whereby forcing is used to sustain vibration and null quadrature, with the required forcing dictated by a model derived using elliptic parameters in a manner similar to [20]. Both damping and frequency mismatch errors are tackled in this paper by applying a force that cancels the effect of angle-dependent imperfections.

Although such a system is shown to reduce drift during gyroscope operation, it only tackles the angle-dependent source of error. While this is, in the ideal case, an effective method for reducing the effect of structural perturbations on measured angle, a large difference between the error predicted by the model used to generate the forcing and the measured error is noted, which prevents the control loops from fully settling. This demonstrates that before the implementation of such a system, considerable refinement is required.

2.6. Modelling

Modelling in terms of rate integrating gyroscopes can refer to a range of subjects, including the thermoelastic behaviour of the structure, such as in [35], and modal analysis of given structures using FEM, as in [36]. Although these are crucial areas of research in the development of gyroscope design, the architecture for the gyroscope is already predetermined and, as such, it is pertinent to primarily investigate the position that the modelling of any control scheme has with regards to the literature.

Work by Gallacher has used perturbation analysis to model the behaviour of a rate-integrating gyroscope [11, 37]. While the work in [11] demonstrates the principles behind the operation of a rate-integrating gyroscope through simulations, the work in [37] goes further by using Simulink to provide a model of a gyroscope under electrostatic tuning, providing results that are closely matched to experimental results. However, the paper serves to demonstrate the potential success of a parametric excitation scheme, and does not address the effect of imperfections on the performance of the gyroscope.

Park and Horowitz [38] model a quadrature-compensation algorithm for a rate gyroscope. The algorithm predicts the changes in gyroscope behaviour caused by quadrature that arises as a result of mismatched modal frequencies and is shown to be effective. However, the control algorithm does not take into account structural imperfections, which are expected to be significant factors governing the performance of rate integrating gyroscopes.

The work by Yilmaz et al [39] includes structural asymmetries in their modelling of ring resonator dynamics. Analysis in this work using FEM demonstrates that the effect of perturbations depends on mode azimuth number, with $n = 2$ yielding the smallest effect. This paper also provides a distinct method for the use of FEM in analysing the effect of structural perturbations in a ring gyroscope structure.

2.7. Application of this work to current research

The use of invariant parameters is well-established in the literature in analysing the behaviour of a rate-integrating gyroscope. However, many of the works that exploit these do so through the use of the method of averaging, whereby a dynamic system is converted to a series of time-invariant systems through averaging out the time-dependency of the system. However, similar to the work by Gallacher [11], this thesis exploits the method of multiple scales in the gyroscope analysis, whereby a dynamic system is similarly converted to a series time-invariant systems, but this is achieved by introducing fast and slow time variables in place of time, and treating these as independent. This is discussed in more depth in section 3.1.3. However, the work in [11] is taken further through the application of modelling and the derivation and testing of a control scheme.

Furthermore, this work looks at the control scheme as a whole, investigating complications that arise when the gyroscope is operated with a fully closed-loop control scheme (i.e. the vibration is driven, rather than free as in [17]). Further works have investigated the sustenance of the vibration, but have not incorporated details such as the effect of mistuning between the drive and resonant frequencies. As such, a detailed model of forcing is produced that considers the effect of inappropriately applied capacitive forcing.

Further, the forcing application is presented in a novel and intuitive manner, allowing the creation of a simplified control scheme.

Overall, this thesis demonstrates a control scheme for a rate-integrating gyroscope. It builds on existing work in using orbital elliptic parameters to model and, later, measure and control the vibration pattern of the gyroscope. It is demonstrated that the individual elements of this control scheme are effective, and gyroscope architectures are proposed that are suitable for fully implementing a closed-loop control scheme for a rate-integrating ring gyroscope.

Chapter 3. Gyroscope Dynamics

3.1. Derivation of the equations of motion in the modal frame

3.1.1. General dynamics

Recalling the derivation of gyroscope equations of motion in previous chapters, the gyroscope's behaviour can be described in terms of the physical axes by equation 3.1, where $\underline{q}$ is a displacement vector describing the motion of the ring along the two physical axes and $\underline{F_D}$ is the force applied from the drive electrodes along these axes. The matrices M, $\hat{C}$, $\hat{G}$ and K are composed of the parameters $\overline{\delta}_m$, $\overline{\gamma}_m$ and $\overline{\mu}_m$, which represent imperfections in the mass, damping and stiffness matrices, respectively, and m = 1,2 and represents the direct and cross-terms of the imperfection matrices. The angular rate, Ω, occurs in the rate matrix, G, where it is multiplied by the term $\frac{2n}{(n^2+1)}$. This term is known as the Bryan factor and is defined as the ratio of the rotation of the vibration pattern to that of the gyroscope body, and recall n is the number of modes in the system [39]. It couples the two equations, in addition to the cross terms of the imperfection matrices. Finally, m_0, ω_0, ζ_0, n and k_0 represent the normalised mass, natural frequency, damping ratio, number of modes and stiffness, respectively. Furthermore, it should be reiterated that angular acceleration terms (such as those arising from centripetal acceleration) have been neglected in this analysis due to their small magnitude.

$$[M]\ddot{\underline{q}} + \left[\hat{C} + \hat{G}\right]\dot{\underline{q}} + [K]\underline{q} = \underline{F_D} \qquad 3.1$$

recall, where:

$$[M] = m_0\begin{bmatrix} 1+\overline{\delta}_1 & \overline{\delta}_2 \\ \overline{\delta}_2 & 1-\overline{\delta}_1 \end{bmatrix} \qquad \left[\hat{C}\right] = 2m_0\omega_0\zeta_0\begin{bmatrix} 1+\overline{\gamma}_1 & \overline{\gamma}_2 \\ \overline{\gamma}_2 & 1-\overline{\gamma}_1 \end{bmatrix}$$

$$\left[\hat{G}\right] = 2m_0\frac{2n}{(n^2+1)}\begin{bmatrix} 0 & -1 \\ 1 & 0 \end{bmatrix}\Omega \qquad [K] = k_0\begin{bmatrix} 1+\overline{\mu}_1 & \overline{\mu}_2 \\ \overline{\mu}_2 & 1-\overline{\mu}_1 \end{bmatrix}$$

The cross-coupling between the two modes of vibration caused by the ring's imperfections is clear from equation 3.1, as is the contribution of applied rate to modal cross-coupling. It is obvious that, in order for the angular rate to be the sole source of modal cross-coupling, the contribution of these structural imperfections must be significantly reduced.

In a similar manner to [11] it becomes convenient to describe these equations of motion in terms of the modal coordinates x_m, where m = 1,2 and denote individual modes of vibration. This involves the use of the transformation $\underline{x} = [X]\underline{q}$, $[X]$ being the normalised eigenvectors of the dynamic matrix $[D] = [M]^{-1}[K]$, to recast the equations of motion in terms of the modal coordinates. $[X]$ is described by equation 3.2, where η is the arctangent of the angle between the physical and modal coordinate axes. Clearly, if η is zero, the modal axes are aligned with the physical axes and the cross-coupling between the modes is zero.

$$[X] = \begin{bmatrix} 1 & -\eta \\ \eta & 1 \end{bmatrix} \tag{3.2}$$

As a result of this transformation, the equations of motion in the modal frame are described by equation 3.3, where $\underline{\chi}_N$ is the forcing projected along the normal modes, the derivation of which will be provided later. The mass imperfections described previously are therefore used to develop the expression for the gyroscope tuning in $[D]$.

$$\ddot{\underline{x}} + \left[\overline{C} + \overline{G}\right]\dot{\underline{x}} + [D]\underline{x} = \underline{\chi}_N \tag{3.3}$$

where:

$$\left[\overline{C}\right] = 2\zeta_0\omega_0\begin{bmatrix} 1+\gamma_1 & \gamma_2 \\ \gamma_2 & 1-\gamma_1 \end{bmatrix} \qquad [D] = {\omega_0}^2\begin{bmatrix} 1+\mu & 0 \\ 0 & 1-\mu \end{bmatrix}$$

$$\left[\overline{G}\right] = 2\frac{2n}{(n^2+1)}\begin{bmatrix} 0 & -1 \\ 1 & 0 \end{bmatrix}\Omega$$

Using the modal axes as references for the analysis of the system produces the desirable situation for analysis in which the only modal cross coupling that occurs is caused by the angular rate and the damping imperfections. However, a further term, μ, occurs in the stiffness matrix. This term is the mistuning of each mode from the average resonant frequency, and will shortly be shown to be a significant source of error.

The Q-factor of the gyroscope is of the order 10^4, resulting in the damping ratio ζ_0 being very small. As such, it becomes possible to derive a small parameter, ε, and use this to describe the damping, as in equation 3.4.

$$\zeta_0 = \varepsilon v_0 \qquad 3.4$$

If the parameters are chosen such that $\varepsilon = 10^{-5}$ (and therefore $v_0 = 2.5$), it is possible to scale all small effects using ε:

$$\mu = \varepsilon\xi \qquad \Omega = \varepsilon\phi \qquad \underline{\chi}_N = \varepsilon\underline{F}_N$$

Equation 3.3 can then be expressed in terms of these, to provide equation 3.5. This expression becomes useful for the perturbation analysis described in section 3.1.3.

$$\underline{\ddot{x}} + 2\varepsilon[C + G]\underline{\dot{x}} + [D]\underline{x} = \varepsilon\underline{F}_N \qquad 3.5$$

where:

$$[C] = v_0\omega_0\begin{bmatrix}1+\gamma_1 & \gamma_2\\ \gamma_2 & 1-\gamma_1\end{bmatrix} \qquad [D] = {\omega_0}^2\begin{bmatrix}1+\varepsilon\xi & 0\\ 0 & 1-\varepsilon\xi\end{bmatrix}$$

$$[G] = \frac{2n}{(n^2+1)}\begin{bmatrix}0 & -1\\ 1 & 0\end{bmatrix}\phi$$

3.1.2. Forcing

The structural vibrations are sustained by applying forces from a series of drive electrodes positioned around the ring structure. By first considering the forcing from a single arbitrary electrode placed at angle ψ to the modal axis, as in figure 3.1, the forcing vector in equation 3.6 provides the forcing exerted by the electrode on the physical axes.

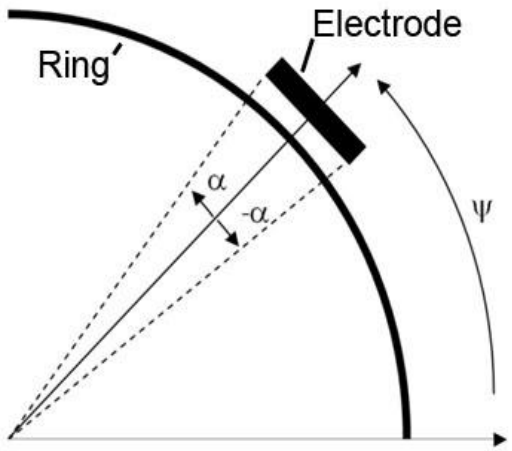

Figure 3.1 - Placement of an arbitrary electrode

$$\underline{F_D} = \check{\beta} V_n{}^2 \begin{bmatrix} \cos n\Psi \\ \sin n\Psi \end{bmatrix} \quad 3.6$$

This is where β is a constant that describes the maximum capacitive force exerted by the electrode and is given by equation 3.7, where it ε_0 is the permittivity of free space and α is the arc angle of an electrode from its centreline, and it can be recalled that R, D and h_0 are the ring radius, thickness and electrode gap, respectively.

$$\check{\beta} = \frac{\varepsilon_0 RD}{h_0{}^3} \sin \alpha \quad 3.7$$

V_n describes the voltage applied at frequency ω to the drive electrode aligned with mode n. It can be noted that the drive frequency is separated from the average resonant frequency (i.e. the ideal drive frequency) by the drive mistuning term λ. Where its associated voltage magnitude is V_{0n}, the voltage delivered to drive electrode n can be expressed as:

$$V_n{}^2 = V_{0n}{}^2 e^{i\omega t} + V_{0n}^*{}^2 e^{-i\omega t} \quad 3.8$$

where:

$$\omega = \omega_0 + \overline{\lambda} \qquad \overline{\lambda} = \varepsilon\lambda$$

By placing the two drive electrodes such that they each align with a physical axis it is clear that, for axes at an angle of $\frac{\pi}{4}$ radians to one another, the forcing exerted by each electrode, as calculated using equation 3.6, can be summed to provide the total forcing from the drive electrodes along each axis, shown by equation 3.9.

$$\underline{F_D} = \check{\beta} \left\{ V_1{}^2 \begin{bmatrix} 1 \\ 0 \end{bmatrix} + V_2{}^2 \begin{bmatrix} 0 \\ 1 \end{bmatrix} \right\} \quad 3.9$$

This can clearly be simplified to:

$$\underline{F_D} = \check{\beta} \begin{bmatrix} V_1{}^2 \\ V_2{}^2 \end{bmatrix} \quad 3.10$$

By considering equation 3.7, it becomes clear that $\check{\beta}$ is small, and as such can be expressed:

$$\check{\beta} = \varepsilon\hat{\beta} \tag{3.11}$$

Further to this, it will prove useful later to divide the forcing described in equation 3.10 into real and imaginary components, providing equation 3.12, which describes the forcing exerted by the drive electrodes along the gyroscope physical axes. The vectors $\underline{g_D}$ and $\underline{h_D}$ describe the real and imaginary components of the forcing magnitude applied from the drive electrode.

$$\underline{F_D} = \varepsilon\hat{\beta}\left\{\underline{f_D}e^{i\omega t} + \underline{f_D^*}e^{-i\omega t}\right\} \tag{3.12}$$

where

$$\underline{f_D} = \underline{g_D} + i\underline{h_D}$$

Evidently, if the modes of vibration are to be used for analysis of the gyroscope, the expression of forcing in equation 3.12 is only valid for forcing along the modal axes if these are precisely aligned with the physical axes of the gyroscope. However, it was established in section 3.1.1 that any perturbations in the stiffness matrix cause the normal modes to be misaligned with the physical axes. Consequently, in the same manner as section 3.1.1 the expression of forcing along the physical axes must be rotated to align with the normal axes. Thus, the expression for forcing along the normal modes of vibration is expressed:

$$\underline{\hat{F}_N} = \varepsilon\hat{\beta}\left\{\underline{\hat{f}_N}e^{i\omega t} + \underline{\hat{f}_N^*}e^{-i\omega t}\right\} \tag{3.13}$$

where

$$\underline{\hat{f}_N} = \begin{bmatrix}(g_{D1} + \eta g_{D2}) + i(h_{D1} + \eta h_{D2})\\(g_{D2} - \eta g_{D1}) + i(h_{D2} - \eta h_{D1})\end{bmatrix}$$

The presence of η in equation 3.13 causes cross-coupling between the components of applied forcing – the forcing applied to one mode has an effect on the other. This has implications in developing a control scheme to sustain gyroscope vibration, as the forcing applied to adjust one mode will inevitably affect the other mode, generating further errors. This effect provides a further motivating factor for ensuring that η is as small as possible.

The perturbation values provided in table 3.1 are conservative estimates for a ring gyroscope provided by [11]. It can be shown that by finding the eigenvectors of the matrix [*D*], as described in section 3.1.1, and entering these parameters for the ring gyroscope described, η has a value of 0.028. Hence, it can be considered a small term and expressed as:

$$\eta = \varepsilon\hat{\eta} \tag{3.14}$$

Parameter	Perturbation	Value
$\overline{\delta}_1$	Mass (direct term)	1×10^{-6}
$\overline{\delta}_2$	Mass (cross term)	5×10^{-7}
$\overline{\gamma}_1$	Damping (direct term)	1×10^{-4}
$\overline{\gamma}_2$	Damping (cross term)	1×10^{-4}
$\overline{\mu}_1$	Stiffness (direct term)	1×10^{-5}
$\overline{\mu}_2$	Stiffness (cross term)	1×10^{-6}

Table 3.1 - Conservative estimates for the perturbation values for a ring gyroscope

3.1.3. Perturbation analysis

To provide a solvable model of the system, perturbation analysis has been used, similar to that in [11, 20, 40]. By expressing the equations in terms of different timescales, it becomes possible to separate the effects of angular rate from any secular terms (i.e. those terms that grow unbounded), thus allowing the behaviour to be efficiently modelled.

To facilitate this, the small parameter ε is used to define *t* in terms of fast and slow timescales, equations 3.15 and 3.16, respectively. In the case of this analysis, the fast timescale corresponds to high frequency behaviour – the ring vibration – whilst the slow timescale corresponds to the movement of the vibration pattern. It will be shown that the separation of the gyroscope behaviour into these two timescales is crucial for successful implementation of a measurement scheme.

$$\hat{t} = t \tag{3.15}$$

$$\overline{t} = \varepsilon t \tag{3.16}$$

Further, the differential operator can be expressed in terms of fast and slow time scales, as in equation 3.17.

$$D = \frac{d}{dt} = \widehat{D} + \varepsilon\overline{D} + O(\varepsilon^2) \tag{3.17}$$

where

$$\widehat{D} = \frac{\partial}{\partial\hat{t}} \qquad \overline{D} = \frac{\partial}{\partial\overline{t}}$$

The solution to equation 3.5 can be expressed as an asymptotic expansion:

$$x(\hat{t},\overline{t}) = x^{(0)}(\hat{t},\overline{t}) + \varepsilon x^{(1)}(\hat{t},\overline{t}) + O(\varepsilon^2) \tag{3.18}$$

Equations 3.5 and 3.18 can then be taken, along with the expressions for the time scales and differential operator, and powers of ε equated to provide two recurrent equations up to the order ε:

$$\frac{\partial^2\underline{x}^{(0)}}{\partial\hat{t}^2} + \omega_0{}^2[I]\underline{x}^{(0)} = 0 \tag{3.19}$$

$$\frac{\partial^2\underline{x}^{(1)}}{\partial\hat{t}^2} - 2\frac{\partial^2\underline{x}^{(0)}}{\partial\hat{t}\partial\overline{t}} - 2[Z_1]\frac{\partial\underline{x}^{(0)}}{\partial\hat{t}} - \omega_0{}^2[Z_2]\underline{x}^{(0)} + \omega_0{}^2[I]\underline{x}^{(1)} = \hat{\beta}\underline{F}_N \tag{3.20}$$

where

$$[Z_1] = \begin{bmatrix} 0 & -\hat{\phi} \\ \hat{\phi} & 0 \end{bmatrix} + \upsilon_0\omega_0\begin{bmatrix} 1+\gamma_1 & \gamma_2 \\ \gamma_2 & 1-\gamma_1 \end{bmatrix} \qquad \hat{\phi} = \frac{2n}{(n^2+2)}\phi$$

$$[Z_2] = \begin{bmatrix} \xi & 0 \\ 0 & -\xi \end{bmatrix} \qquad F_N = \varepsilon\hat{\beta}\left\{\underline{f}_N e^{i\omega t} + f_N^* e^{-i\omega t}\right\} \qquad \underline{f}_N = \begin{bmatrix} g_{D1} + ih_{D1} \\ g_{D2} + ih_{D2} \end{bmatrix}$$

It can be noted here that η no longer appears in the forcing terms as it becomes a parameter of the order ε^2. Parameters of a higher order than ε have been eliminated as they are expected to be of little significance considering that the magnitude of ε is of the order 10^{-5}. In order to

remove any singularities, it is necessary to find a solution to these equations that eliminates any resonance-producing terms. The derivation of this solution is described shortly.

A solution to equation 3.19 is given by equation 3.21, where terms $\underline{\alpha}$ and $\underline{\overline{\beta}}$ are the real and imaginary components of the electrode responses relative to a $\cos(\omega_0\hat{t})$ reference wave. Φ_n represents the phase of mode *n* with respect to the reference wave and χ_n the magnitude of the mode *n* response.

$$\underline{x}^{(0)} = \underline{\alpha}\cos\omega_0\hat{t} - \underline{\beta}\sin\omega_0\hat{t} \qquad 3.21$$

where:

$$\underline{\alpha} = \begin{bmatrix}\alpha_1\\ \alpha_2\end{bmatrix} = \begin{bmatrix}\chi_1\cos\Phi_1\\ \chi_2\cos\Phi_2\end{bmatrix} \qquad \underline{\overline{\beta}} = \begin{bmatrix}\beta_1\\ \beta_2\end{bmatrix} = \begin{bmatrix}\chi_1\sin\Phi_1\\ \chi_2\sin\Phi_2\end{bmatrix} \qquad \underline{\beta} = i\underline{\overline{\beta}}$$

By using this solution to take the appropriate derivatives of $x^{(0)}$ and substituting these into equation 3.20, a new expression solely in terms of $x^{(1)}$ is obtained, where the Coriolis and damping effects appear in $[Z_1]$ and the mistuning effects appear in $[Z_2]$:

$$\frac{\partial^2\underline{x}^{(1)}}{\partial\hat{t}^2} + {\omega_0}^2[I]\underline{x}^{(1)} + \sin\omega_0\hat{t}\left\{2\omega_0\frac{\partial}{\partial\overline{t}}\underline{\alpha} + 2\omega_0[Z_1]\underline{\alpha} + {\omega_0}^2[Z_2]\underline{\beta}\right\} + \cos\omega_0\hat{t}\left\{2\omega_0\frac{\partial}{\partial\overline{t}}\underline{\beta} + 2\omega_0[Z_1]\underline{\beta} - {\omega_0}^2[Z_2]\underline{\alpha}\right\} = \hat{\beta}\underline{F_N} \qquad 3.22$$

The forcing term can also be re-written in a similar way:

$$\underline{F_N} = 2\cos\omega_0\hat{t}\left\{\underline{k}_1\cos\lambda\overline{t} - \underline{k}_2\sin\lambda\overline{t}\right\} - 2\sin\omega_0\hat{t}\left\{\underline{k}_1\sin\lambda\overline{t} + \underline{k}_2\cos\lambda\overline{t}\right\} \qquad 3.23$$

where:

$$\underline{k}_1 = \begin{bmatrix}g_{D1}\\ g_{D2}\end{bmatrix} \qquad \underline{k}_2 = \begin{bmatrix}h_{D1}\\ h_{D2}\end{bmatrix}$$

For a gyroscope where the modal axes are aligned with the physical axes (i.e. no cross-coupling is present) $\eta = 0$ and, for a gyroscope where the drive frequency matches its resonant frequency precisely, $\lambda = 0$. From equation 3.23, it is clear that the presence of drive mistuning

results in the in-phase components of forcing generating some quadrature motion and vice versa. This is compounded by the presence of even limited modal cross-coupling, which has already been demonstrated to result in cross-coupling (albeit small) between the forces applied to each mode of vibration. It is therefore necessary that, as well as ensuring that the modes of vibration are aligned as closely as possible with the physical axes, the drive frequency must also match the average resonant frequency of the ring as closely as possible.

As already established, resonant forcing terms appearing in equations 3.19 and 3.20 would lead to unbounded solutions. Consequently, it becomes necessary to equate all resonance-producing terms to zero, with the conditions for this provided by equations 3.24 and 3.25.

$$\frac{\partial}{\partial \bar{t}}\underline{\alpha} + [Z_1]\underline{\alpha} + \frac{\omega_0}{2}[Z_2]\underline{\beta} + \underline{F_A} = 0 \qquad 3.24$$

$$\frac{\partial}{\partial \bar{t}}\underline{\beta} + [Z_1]\underline{\beta} - \frac{\omega_0}{2}[Z_2]\underline{\alpha} - \underline{F_B} = 0 \qquad 3.25$$

where:

$$\underline{F_A} = \frac{\hat{\beta}}{\omega_0}\{\underline{k_1}\sin\lambda\bar{t} + \underline{k_2}\cos\lambda\bar{t}\} \qquad \underline{F_B} = \frac{\hat{\beta}}{\omega_0}\{\underline{k_1}\cos\lambda\bar{t} - \underline{k_2}\sin\lambda\bar{t}\}$$

These slow time conditions describe the envelope of the gyroscope motion, and hence describe how the high frequency behaviour is adjusted by the slow time effects. As these encapsulate all imperfections, and therefore all sources of error in the gyroscope, it is necessary to describe the control scheme solely in terms of these slow time effects.

It becomes useful to rearrange the forcing expressions $F_{A,B}$ so that they provide a more convenient reflection of forcing behaviour. As opposed to considering the individual forcing terms as variables in their own right, it is useful for the implementation of a drive scheme to consider them as functions of their associated drive phases, where A_n is the forcing magnitude and θ_{Dn} the drive phase of mode n:

$$g_{Dn} = A_n \cos\Phi_{Dn} \qquad 3.26$$

$$h_{Dn} = A_n \sin\Phi_{Dn} \qquad 3.27$$

where:

$$\theta_{Dn} = \omega_o \hat{t} + \lambda \bar{t} + \Phi_{Dn} \tag{3.28}$$

It is then possible to simplify the forcing to provide expressions in terms of a controllable variable, A_n, and a measurable variable, Φ_{Dn}. These prove useful for implementation of the control scheme and are given by equations 3.29 and 3.30.

$$\underline{F_A} = \frac{\hat{\beta}}{\omega_0}\begin{bmatrix} A_1 \sin\left(\Phi_{D1} + \lambda \bar{t}\right) \\ A_2 \sin\left(\Phi_{D2} + \lambda \bar{t}\right) \end{bmatrix} \tag{3.29}$$

$$\underline{F_B} = \frac{\hat{\beta}}{\omega_0}\begin{bmatrix} A_1 \cos\left(\Phi_{D1} + \lambda \bar{t}\right) \\ A_2 \cos\left(\Phi_{D2} + \lambda \bar{t}\right) \end{bmatrix} \tag{3.30}$$

From these expressions, it is clear that the drive mistuning λ moves the forcing away from the measured drive phase, thus slowly degrading the precision of any phase locked loop. This reinforces the importance of the previously stated condition that $\lambda = 0$.

3.2. Description in terms of orbital elliptic parameters

Equation 3.5 provides an accurate representation of the gyroscope dynamics when expressed in the modal frame, while equations 3.24 and 3.25 provide details about the slow time dynamics that are of interest in the development of a control scheme. However, in order to produce a control scheme that can apply forcing appropriately, it is convenient to recast these equations of motion in terms of orbital elliptic parameters. It is worth re-iterating here that the equations following have been derived using the assumption that angular acceleration terms and terms of $O(\varepsilon^2)$ have been neglected as they can be considered to have a negligible effect when compared to those terms of larger magnitude.

As alluded to in section 2.2, the use of orbital elliptic parameters allows the trajectory of the gyroscope to be described in terms of the parameters of an ellipse. Doing so allows errors to be more easily measured and controlled, as well as providing a convenient method for the measurement of gyroscope rotation. These parameters are shown by figure 3.2, where *a* is, for a perfect gyroscope, the trajectory of vibration, while *b* is non-zero in the presence of imperfections. The angle that the ellipse makes with the reference axis is represented by φ, while θ is known as the orbital phase and represents the position of an arbitrary point on the parameter of the ellipse.

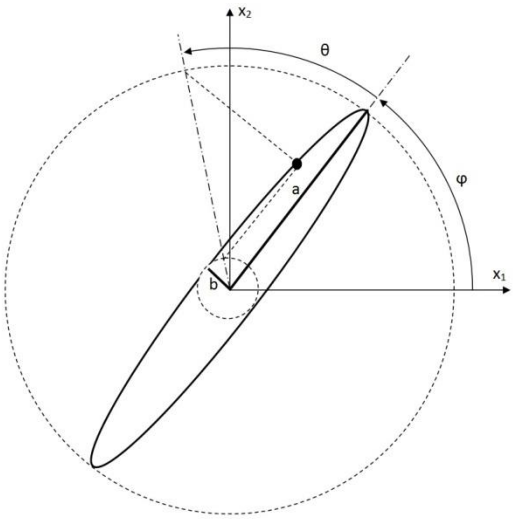

Figure 3.2 - The orbital elliptic parameters used to describe gyroscope vibration

The imperfection that has the dominant effect on the size of *b* is the modal mistuning of the gyroscope [17]. This leads to the conclusion that, for a well-tuned stationary gyroscope the trajectory is almost a straight line, that is $a >> b$. This feature becomes important in devising the control scheme for the gyroscope.

The parameter θ is known as the orbital phase and can be provided by equation 3.31, where Φ_o is the phase difference between it and the reference phase

$$\theta = \omega_0 t + \Phi_o \tag{3.31}$$

It will later be shown that the orbital phase can be used to devise a phase locked loop, the benefits and design of which are described further in section 4.2.

The transformations in equations 3.32 and 3.33 are used to describe cartesian coordinates in terms of orbital elliptic parameters. By differentiating these, as well as the solutions for x_n from equation 3.21, setting like terms in x_n equal to each other and simplifying, it becomes possible to obtain the expressions provided in equations 3.34 to 3.37, where it can be recalled that α_n and β_n can be considered to be the real and imaginary electrode responses for the primary and secondary modal pick-offs, respectively, relative to a $\cos(\omega_0 \hat{t})$ reference signal.

$$x_1 = a\cos\theta\cos\varphi - b\sin\theta\sin\varphi \quad 3.32$$

$$x_2 = a\cos\theta\sin\varphi + b\sin\theta\cos\varphi \quad 3.33$$

$$\alpha_1 = a\cos\Phi_o\cos\varphi - b\sin\Phi_o\sin\varphi \quad 3.34$$

$$\alpha_2 = a\cos\Phi_o\sin\varphi + b\sin\Phi_o\cos\varphi \quad 3.35$$

$$\beta_1 = a\sin\Phi_o\cos\varphi + b\cos\Phi_o\sin\varphi \quad 3.36$$

$$\beta_1 = a\sin\Phi_o\sin\varphi - b\cos\Phi_o\cos\varphi \quad 3.37$$

As the electrode responses are measurable quantities obtained by decomposing the relevant pick-off responses, it becomes possible to take combinations of those expressed by equations 3.34 to 3.37 to form the measurable invariants in equations 3.38 to 3.43. These invariants were derived through a trial-and-error process, using a script to cycle through a number of combinations of electrode response combinations, with those that provided the most convenient measures of ellipse parameters chosen for use in the control scheme.

$$E_1 = {\alpha_1}^2 + {\alpha_2}^2 + {\beta_1}^2 + {\beta_2}^2 = a^2 + b^2 \quad 3.38$$

$$E_2 = 2(\alpha_1\beta_2 - \alpha_2\beta_1) = -2ab \quad 3.39$$

$$E_3 = {\alpha_1}^2 - {\alpha_2}^2 + {\beta_1}^2 - {\beta_2}^2 = (a^2 - b^2)\cos 2\varphi \quad 3.40$$

$$E_4 = 2(\alpha_1\alpha_2 + \beta_1\beta_2) = (a^2 - b^2)\sin 2\varphi \quad 3.41$$

$$E_{5R} = {\alpha_1}^2 + {\alpha_2}^2 - {\beta_1}^2 - {\beta_2}^2 = (a^2 - b^2)\cos 2\Phi_o \quad 3.42$$

$$E_{5I} = 2(\alpha_1\beta_1 + \alpha_2\beta_2) = (a^2 - b^2)\sin 2\Phi_o \quad 3.43$$

As discussed previously, it is assumed that $a >> b$. Therefore, from these it is possible to surmise that $E_1 \approx a^2$, which in turn leads to the conclusion that E_2 is proportional to b. These properties provide convenient measures of a and b. Finally, it is clear that the ellipse precession and orbital phase, φ and Φ_o, can be calculated using equations 3.44 and 3.45.

$$\varphi = \frac{1}{2}\tan^{-1}\frac{E_4}{E_3} \quad 3.44$$

$$\Phi_o = \frac{1}{2}\tan^{-1}\frac{E_{5I}}{E_{5R}} \quad 3.45$$

With equations 3.38 to 3.43 providing measurable quantities, it becomes logical to rewrite the conditions described in equations 3.24 and 3.25 in terms of these invariants. It is first necessary to express these conditions in terms of the orbital elliptic parameters by substituting in the expressions for electrode responses in equations 3.34 to 3.37. By expanding the conditions in equations 3.24 and 3.25 to provide those in equations 3.46 to 3.49, it becomes possible to rearrange them using the processes detailed in equations 3.50 to 3.53 to provide the coupled equations 3.54 to 3.57.

$$A = \dot{\alpha}_1 + v_0\omega_0\{(1 + \gamma_1)\alpha_1 + \gamma_2\alpha_2\} - \hat{\phi}\alpha_2 + \frac{\omega_0\xi}{2}\beta_1 + \frac{\hat{\beta}}{\omega_0}A_1\sin(\Phi_{D1} + \lambda\bar{t}) = 0 \quad 3.46$$

$$B = \dot{\alpha}_2 + v_0\omega_0\{(1 - \gamma_1)\alpha_2 + \gamma_2\alpha_1\} + \hat{\phi}\alpha_1 - \frac{\omega_0\xi}{2}\beta_2 + \frac{\hat{\beta}}{\omega_0}A_2\sin(\Phi_{D1} + \lambda\bar{t}) = 0 \quad 3.47$$

$$C = \dot{\beta}_1 + v_0\omega_0\{(1 + \gamma_1)\beta_1 + \gamma_2\beta_2\} - \hat{\phi}\beta_2 - \frac{\omega_0\xi}{2}\alpha_1 - \frac{\hat{\beta}}{\omega_0}A_1\cos(\Phi_{D1} + \lambda\bar{t}) = 0 \quad 3.48$$

$$D = \dot{\beta}_2 + v_0\omega_0\{(1 + \gamma_1)\beta_2 + \gamma_2\beta_1\} - \hat{\phi}\beta_1 + \frac{\omega_0\xi}{2}\alpha_2 - \frac{\hat{\beta}}{\omega_0}A_2\cos(\Phi_{D1} + \lambda\bar{t}) = 0 \quad 3.49$$

$$\{A\cos\varphi + B\sin\varphi\}\cos\Phi_o + \{C\cos\varphi + D\sin\varphi\}\sin\Phi_o = E \quad 3.50$$

$$\{C\sin\varphi + D\cos\varphi\}\cos\Phi_o - \{A\sin\varphi - B\cos\varphi\}\sin\Phi_o = F \quad 3.51$$

$$\{C\sin\varphi + D\cos\varphi\}\sin\Phi_o + \{A\sin\varphi - B\cos\varphi\}\cos\Phi_o = G \quad 3.52$$

$$\{A\cos\varphi + B\sin\varphi\}\sin\Phi_o - \{C\cos\varphi + D\sin\varphi\}\cos\Phi_o = H \quad 3.53$$

$$E = \dot{a} + a\omega_0 v_0(1 + \gamma_1\cos 2\varphi + \gamma_2\sin 2\varphi) + \frac{1}{2}b\omega_0\xi\sin 2\varphi - F_1 = 0 \quad 3.54$$

$$F = \dot{b} - \frac{1}{2}a\omega_0\xi\sin 2\varphi + b\omega_0 v_0(1 - \gamma_1\cos 2\varphi - \gamma_2\sin 2\varphi) - F_2 = 0 \quad 3.55$$

$$G = \dot{\varphi} - \omega_0 v_0(\gamma_1\sin 2\varphi - \gamma_2\cos 2\varphi) + \frac{b}{a}\left(\dot{\Phi}_o + \frac{1}{2}\omega_0\xi\cos 2\varphi\right) + \hat{\phi} + F_3 = 0 \quad 3.56$$

$$H = \dot{\Phi}_o - \frac{1}{2}\omega_0\xi\cos 2\varphi + \frac{b}{a}\{\hat{\phi} + \dot{\varphi} + \omega_0 v_0(\gamma_1\sin 2\varphi - \gamma_2\cos 2\varphi)\} - F_4 = 0 \quad 3.57$$

where:

$$F_1 = \frac{\hat{\beta}}{\omega_0}\{A_1 \sin\sigma_1 \cos\varphi + A_2 \sin\sigma_2 \sin\varphi\}$$

$$F_2 = \frac{\hat{\beta}}{\omega_0}\{A_1 \cos\sigma_1 \sin\varphi - A_2 \cos\sigma_2 \cos\varphi\}$$

$$F_3 = \frac{\hat{\beta}}{\omega_0}\{A_1 \sin\sigma_1 \sin\varphi - A_2 \sin\sigma_2 \cos\varphi\}$$

$$F_4 = \frac{\hat{\beta}}{\omega_0}\{A_1 \cos\sigma_1 \cos\varphi + A_2 \cos\sigma_2 \sin\varphi\}$$

$$\sigma_n = \Phi_{Dn} + \lambda\bar{t} + \Phi_o$$

By assuming that $a >> b$, so that $E_1 \approx a^2$ and therefore any components of forcing multiplied by b are negligible in comparison to those multiplied by a, extensively rearranging and substituting E_1 and E_2 into these, the equations in 3.58 to 3.61 are derived, where ω_0 is the average resonant frequency of the two modes of vibration, υ_0 scaled damping ratio, γ_n are damping perturbations, ξ is the scaled modal mistuning, $\hat{\phi}$ the scaled applied rate, φ the ellipse precession and F_n is the force applied by the drive electrodes to the relevant parameter.

$$\dot{E}_1 = -\omega_0\upsilon_0(1 + \gamma_1 \cos 2\varphi + \gamma_2 \sin 2\varphi)E_1 + \sqrt{E_1}F_1 \quad 3.58$$

$$\dot{E}_2 = -\omega_0\xi \sin 2\varphi\, E_1 - 2\omega_0\upsilon_0 E_2 - \sqrt{E_1}F_2 \quad 3.59$$

$$\dot{\varphi} = \omega_0\upsilon_0(\gamma_1 \sin 2\varphi - \gamma_2 \cos 2\varphi) - \left(\frac{1}{2}\omega_0\xi \cos 2\varphi\right)\frac{E_2}{E_1} - \hat{\phi} - \frac{1}{\sqrt{E_1}}F_3 \quad 3.60$$

$$\dot{\Phi}_o = \frac{1}{2}\omega_0\xi \cos 2\varphi - \{\omega_0\upsilon_0(\gamma_1 \sin 2\varphi - \gamma_2 \cos 2\varphi)\}\frac{E_2}{E_1} + \frac{1}{\sqrt{E_1}}F_4 \quad 3.61$$

These coupled equations describe the envelope of the gyroscope vibration, crucially allowing its angle to be extracted. It is clear from these that, in the absence of imperfections and forcing, $\dot{\varphi} = -\hat{\phi}$ and hence the input angle to the gyroscope is proportional to the change in angle of the ellipse. It therefore becomes clear that any control system must be focussed on

removing as many imperfections as possible, while ensuring that any force used to do so is appropriately nulled.

Chapter 4. Control scheme description

4.1. Control scheme design

Equation 3.60 states that, in the absence of any imperfections in the structure of the gyroscope and in the absence of forcing, the rate of precession of the ellipse is proportional to that of the gyroscope. Consequently, the angle of gyroscope rotation is proportional to the angle of precession of the ellipse. As such, any control system must eliminate the effect of these imperfections as far as possible, while ensuring that any forces that arise as a result of doing so do not have any influence on the ellipse angle.

Due to the high Q-factor of the device, it can be assumed that the damping perturbations are far smaller than the mistuning perturbations. Consequently, a scheme for increasing the accuracy of the gyroscope should primarily focus on reducing the effect of mistuning.

The mistuning manifests itself in the form of the mistuning parameter, ξ, which is the scaled quantity that describes the level of mistuning between response frequencies of the two modes of vibration. For angular rate to be the dominant effect in the behaviour of the ellipse precession, the input rate must be much greater than the term $\frac{\omega_0 \xi E_2}{2E_1}$ in equation 3.60, where E_2/E_1 corresponds to the ratio of minor axis to major axis of the measurement ellipse. Although the precise magnitude of the minimum rate varies according to the level of mistuning, for a gyroscope similar to that described in this project with no control scheme applied the rate must exceed 1rad.s^{-1} to achieve an error of less than 10%, with the rate applied in practice generally being much higher than this [11].

While ξ can be reduced by using an offline tuning method such as electrostatic tuning, as described in section 4.3.1, it also becomes clear from equation 3.60 that its effect on measured precession angle can be minimised further by driving the ratio $\frac{E_2}{E_1}$ to zero.

As stated previously, if the major axis of the ellipse, a, is much greater than its minor axis, b, $E_1 \approx a^2$. Therefore, maintaining E_1 at a constant value will ensure that a is constant, in which case it becomes clear from equation 3.39 that E_2 is proportional to b. Hence, a control system to reduce the effect of stiffness imperfections on the measurement of gyroscope angle should involve the reduction of modal mistuning, the sustenance of E_1 at a constant value and the minimisation of E_2 to reduce the effect of modal mistuning on ellipse precession. It is clear

that, if E_2 is proportional to b, this control scheme has the effect of flattening the ellipse described by figure 3.2.

The effectiveness of such a control scheme is studied further in chapter 5.

4.2. Phase locked loop

The analysis in section 3.1.2 indicates that to achieve an appropriate response, the forcing applied via the drive electrodes must have a frequency that is equal to the average resonant frequency of the two modes of vibration, ω_0. The use of a phase locked loop, (PLL), is a convenient method to achieve this.

The orbital phase, Φ_o, has been chosen as the parameter to be used in controlling the drive frequency. This has the advantage of not relying on the response phases, which vary as rotation is applied to the gyroscope, so provides a stable parameter to be used for the control of drive frequency. Furthermore errors inherent in the system, such as electronic delays, result in the phase values of both modes of vibration being away from their expected values of 90º. Coupling this with the requirement that the gyroscope must be driven at the average resonant frequency of the two modes of vibration to achieve equal modal amplitude, Φ_o becomes a convenient parameter to achieve this, as it is not dependent on the phase of either mode.

Nevertheless, it can be noted from equation 3.61 that the orbital phase is modulated by $\cos(\varphi)$, that is it is dependent upon the angle of ellipse precession, φ, and is acted upon by the forcing term F_4. The $\cos(\varphi)$ term is multiplied by the mistuning parameter, which should be minimised prior to production using electrostatic tuning, so can be considered of little importance when compared to the F_4 term. It is likely that F_4 would have a considerable effect on the behaviour of Φ_o and as such must be nulled if the phase locked loop is to be a success.

Section 6.1 provides experimental results that demonstrate the effectiveness of such a PLL when implemented. Finally, section 6.4.4 describes the performance of the PLL while under rate.

4.3. Modal tuning

4.3.1. Initial tuning

As described previously, it is a necessity for a successful control scheme that the modal mistuning, along with any cross-coupling present, must initially be as small as possible. Due to the proportional relationship between mistuning and ellipse width, it is this condition that makes the assumption a>>b valid, and as such is of crucial importance to any control scheme that is derived using orbital elliptic parameters (as this makes possible the use of the relationships $E_1 \approx a^2$ and E_2 is proportional to b).

In order to achieve a small level of modal mistuning electrostatic tuning has been implemented. This method, as described in [22], uses a series of tuning electrodes around the inside of the ring to apply electrostatic forces that act upon the stiffness matrix in equation 3.1 to independently adjust the direct mistuning terms and the cross terms. The electrostatic forces can therefore be represented as a modification to a stiffness matrix, where for a single electrode placed at angle ψ from the modal axis and with arc angle α this modification is provided in equation 4.1, where V_j is the voltage applied through the electrode.

$$[K_{Ej}] = \breve{\beta} V_j^{\,2} \begin{bmatrix} 2\alpha + \frac{1}{n}\cos 2n\psi_j \sin 2n\alpha & \frac{1}{2n}\sin 2n\psi_j \sin 2n\alpha \\ \frac{1}{2n}\sin 2n\psi_j \sin 2n\alpha & 2\alpha - \frac{1}{n}\cos 2n\psi_j \sin 2n\alpha \end{bmatrix} \qquad 4.1$$

The gyroscope tuning arrangement consists of sixteen tuning electrodes placed around the inside perimeter of the ring in pairs such that each pair is bisected by the direct response of its corresponding drive or pick-off electrode. The placement of such a pairing is shown in figure 4.1. There are two sets of tuning electrodes, with each set consisting of four pairs positioned at 90° from one another. Note that ψ is chosen such that it provides the simplest solution to the stiffness matrix.

By taking combinations of the voltages applied through these electrodes, as detailed in [22], the terms in equations 4.2 to 4.4 are derived, which in turn can be applied to the electrostatic stiffness matrix to provide equation 4.5. This matrix can then be expressed in terms of the calculable C_n and D_n, as in equation 4.6.

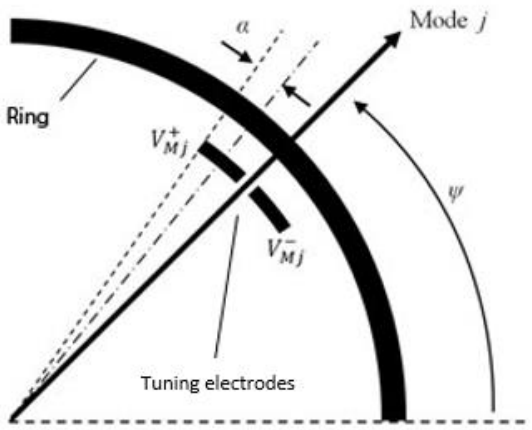

Figure 4.1 - The placement of a pair of tuning electrodes relative to a modal axis

$$K_{11} = \check{\beta}\left\{2\alpha\left({V_{M1}^{+}}^2 + {V_{M1}^{-}}^2 + {V_{M2}^{+}}^2 + {V_{M2}^{-}}^2\right) + \frac{1}{n}\sin 2n\alpha \cos 2n\alpha \left({V_{M1}^{+}}^2 + {V_{M1}^{-}}^2 - {V_{M2}^{+}}^2 - {V_{M2}^{-}}^2\right)\right\} \quad 4.2$$

$$K_{12} = K_{21} = \check{\beta}\frac{1}{2n}\sin 2n\alpha \cos 2n\alpha \left({V_{M1}^{+}}^2 - {V_{M1}^{-}}^2 - {V_{M2}^{+}}^2 + {V_{M2}^{-}}^2\right) \quad 4.3$$

$$K_{22} = \check{\beta}\left\{2\alpha\left({V_{M1}^{+}}^2 + {V_{M1}^{-}}^2 + {V_{M2}^{+}}^2 + {V_{M2}^{-}}^2\right) - \frac{1}{n}\sin 2n\alpha \cos 2n\alpha \left({V_{M1}^{+}}^2 + {V_{M1}^{-}}^2 + {V_{M2}^{+}}^2 + {V_{M2}^{-}}^2\right)\right\} \quad 4.4$$

$$[K_E] = \begin{bmatrix} K_{11} & K_{12} \\ K_{21} & K_{22} \end{bmatrix} \quad 4.5$$

$$[K_E] = \begin{bmatrix} \varrho_1(C_1 + C_2) + \varrho_2(C_1 - C_2) & \varrho_3(D_1 - D_2) \\ \varrho_3(D_1 - D_2) & \varrho_1(C_1 + C_2) - \varrho_2(C_1 - C_2) \end{bmatrix} \quad 4.6$$

Where:

$$\varrho_1 = 2\check{\beta}\alpha \qquad \varrho_2 = \frac{\check{\beta}}{n}\sin 2n\alpha \cos 2n\alpha \qquad \varrho_3 = \frac{\check{\beta}}{2n}\sin 2n\alpha \cos 2n\alpha$$

$$C_1 = {V_{M1}^{+}}^2 + {V_{M1}^{-}}^2 \qquad C_2 = {V_{M2}^{+}}^2 + {V_{M2}^{-}}^2 \qquad D_1 = {V_{M1}^{+}}^2 - {V_{M1}^{-}}^2$$

$$D_2 = {V_{M2}^{+}}^2 - {V_{M2}^{-}}^2$$

Using this method, both cross and direct stiffness perturbations can be nulled by adjusting the relevant voltages to achieve suitable values of D_n and C_n respectively. The procedure employed involves tuning the gyroscope in rate mode (i.e. exciting the first mode of vibration only to resonance), and then first reducing the second mode amplitude to zero by adjusting the cross terms of the stiffness matrix. The ratio of the real to imaginary components of the second mode response is then maximised by adjusting the direct terms. This method has the effect of reducing coupling between the first and second mode of vibration first through the elimination (as far as possible) of the 'undesired' mode, and then by rotating this second mode to a more desirable alignment.

By following this method, the gyroscope has been electrostatically tuned to a low level of modal mistuning, which is demonstrated to be of the order of mHz in section 6.1. This is a very small difference in resonant frequency between the two modes and provides a convenient starting point for the implementation of the control scheme described.

4.3.2. Application of E_2 to tuning

The width of the ellipse described in section 3.2 is primarily affected by the level of modal mistuning [20], which leads to the result that the size of E_2 is proportional to the level of modal mistuning within the gyroscope, as it was previously established that $E_2 \propto b$. This behaviour can be observed by the contour plot of the ratio E_2/E_1 in figure 4.2. This clearly shows that, when the gyroscope is described in terms of its physical coordinates (i.e. by using equation 3.1), E_2/E_1 exhibits a minimum where the cross coupling and direct mistuning fall to zero.

This relationship suggests that it may be possible to devise an algorithm that can automatically tune the gyroscope by searching for the minimum value of E_2 as the cross and direct terms are independently adjusted by using the tuning electrodes described in section 4.3.1. However, this relationship is complicated somewhat on the application of angular rate. It is clear from figure 4.3 that the value of E_2/E_1 at any given level of modal mistuning is modulated by the ellipse angle. Nevertheless, this problem only arises if rotation is applied to the gyroscope while tuning is in progress.

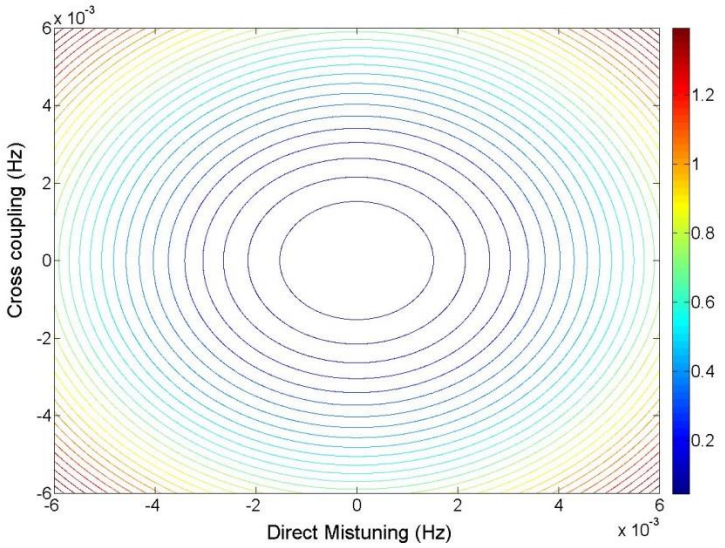

Figure 4.2 - Contour plot of E_2 showing the effect of mistuning in the stiffness matrix

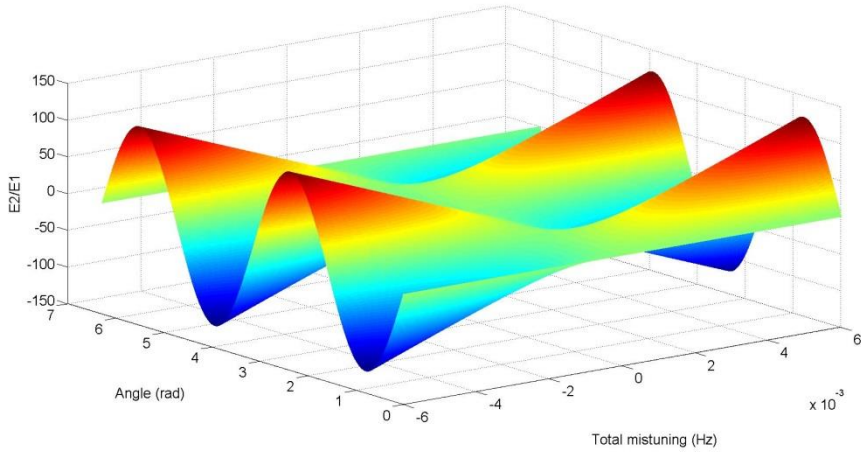

Figure 4.3 - Plot of E_2/E_1 showing the effect of angle at a range of levels of modal mistuning

Consequently, it becomes clear that, while there is no rotation applied to the gyroscope, it is possible to produce a control scheme that can utilise E_2 to maintain a high degree of tuning within the gyroscope through adjustment of the electrodes used for the electrostatic tuning described previously. Although not practical to tune the gyroscope in real-time, the scheme provides a reliable post-production automatic tuning method.

Due to the complexity imposed by the effect of rate, the implementation of such a scheme is beyond the scope of this project but is a very useful avenue for future research.

4.4. Control scheme implementation

The gyroscope is mounted onto a custom printed circuit board, which is in turn connected to an Analog Devices ADSP 21469 processing board. The signals to and from the gyroscope are processed using a combination of C and assembly code, with the control scheme being implemented in a C program. For experimental purposes, a Matlab-based graphical user interface is used to operate the program and log data.

As discussed in section 4.2 the orbital phase, Φ_o, has been used to construct a PLL. This PLL uses a conventional PID control to adjust the drive frequency according to Φ_o, the required value of which is discussed in section 6.1.

The conditions required of E_1 and E_2 are achieved through the use PID controls that alter the gains of the two drive electrodes, A_1 and A_2, which are used to control E_1 and E_2 respectively. The set point of E_1 has been chosen such that it produces a clear modal response but does not approach the limit of the ring's vibration, while the set point of E_2 is zero. The drive phases have been chosen such that the size of E_2 is reduced as far as possible before activation of the control scheme. For this gyroscope, that is equal drive phases, (i.e. $\Phi_1 = \Phi_2$, hence $\sigma_1 = \sigma_{2)}$.

Finally, it has been established previously that, in order for the measurement of angle to be as accurate as possible, there must be no forcing acting upon the precession of the ellipse. Similarly, there must be no forcing acting upon the orbital phase if it is to have a consistent value when the ring is vibrating at resonance.

The conditions described in equations 4.7 and 4.8 can be implemented (subject to the phases described above being used in the forcing) to ensure that forcing on the ellipse precession and orbital phase is zero.

$$A_2 = A_1 \tan\varphi \qquad 4.7$$

$$A_1 = -A_2 \tan\varphi \qquad 4.8$$

It is clear that, with just the two drive electrodes in A_1 and $A_{2,}$ it is not possible to operate a control loop for E_2 while ensuring that the force exerted on the precession and orbital phase is zero. However, it will be possible to activate all three conditions separately in order to demonstrate their effectiveness if extra control electrodes were to become available. Possible gyroscope designs that would facilitate this control scheme are described in chapter 8.

Furthermore, where $\varphi = 45°$ these conditions ensure that there is no forcing on the orbital phase or precession angle if $A_1 = A_2$. This is a useful condition for stationary tests, such as the frequency sweeps and phase locked loop assessment described in chapter 6.

At this point, it may be postulated that a control scheme can be devised that only nulls E_2, and ignores the value of E_1, as equation 3.58 indicates that any gain used to do so will elicit a response in E_1. Such a scheme would therefore allow the required degrees of freedom in the system to be reduced and hence aid simplification of the control scheme.

However, recall from section 4.1 that, in order for E_2 to be proportional to b (a requirement for the proposed control scheme), a must be constant. Therefore, as E_1 is proportional to a^2, E_1 must be sustained at a constant value and, as a result, all four drive gains must be controlled.

Chapter 5. Gyroscope Modelling

5.1. Simple model

In order to take advantage of the ease with which continuous systems can be modelled, Simulink has been chosen to produce a simulation of the control scheme described in chapter 4.

Initially, the gyroscope motion described by equation 3.3 has been modelled assuming that the gyroscope design is perfect, (i.e. there is no cross-coupling). The intention behind this model is to demonstrate the basic principles behind the operation of the rate integrating gyroscope. The model incorporates the realistic properties derived from those in table 3.1 to model the gyroscope, these being provided in table 5.1. The Simulink model produced is shown in figure 5.1.

Parameter	Parameter Name	Value
ω_0 (rad.s^{-1})	Average resonant frequency	$2\pi 14259$
ε	Scaling parameter	10^{-5}
ζ_0	Damping ratio	5×10^{-5}
$\gamma_{1,2}$	Damping perturbations	10^{-4}
μ (Hz)	Modal mistuning	10^{-5}
$\check{\beta}$ (N)	Capacitive force from electrodes	1.4×10^{-8}

Table 5.1 - Parameters used in the gyroscope model

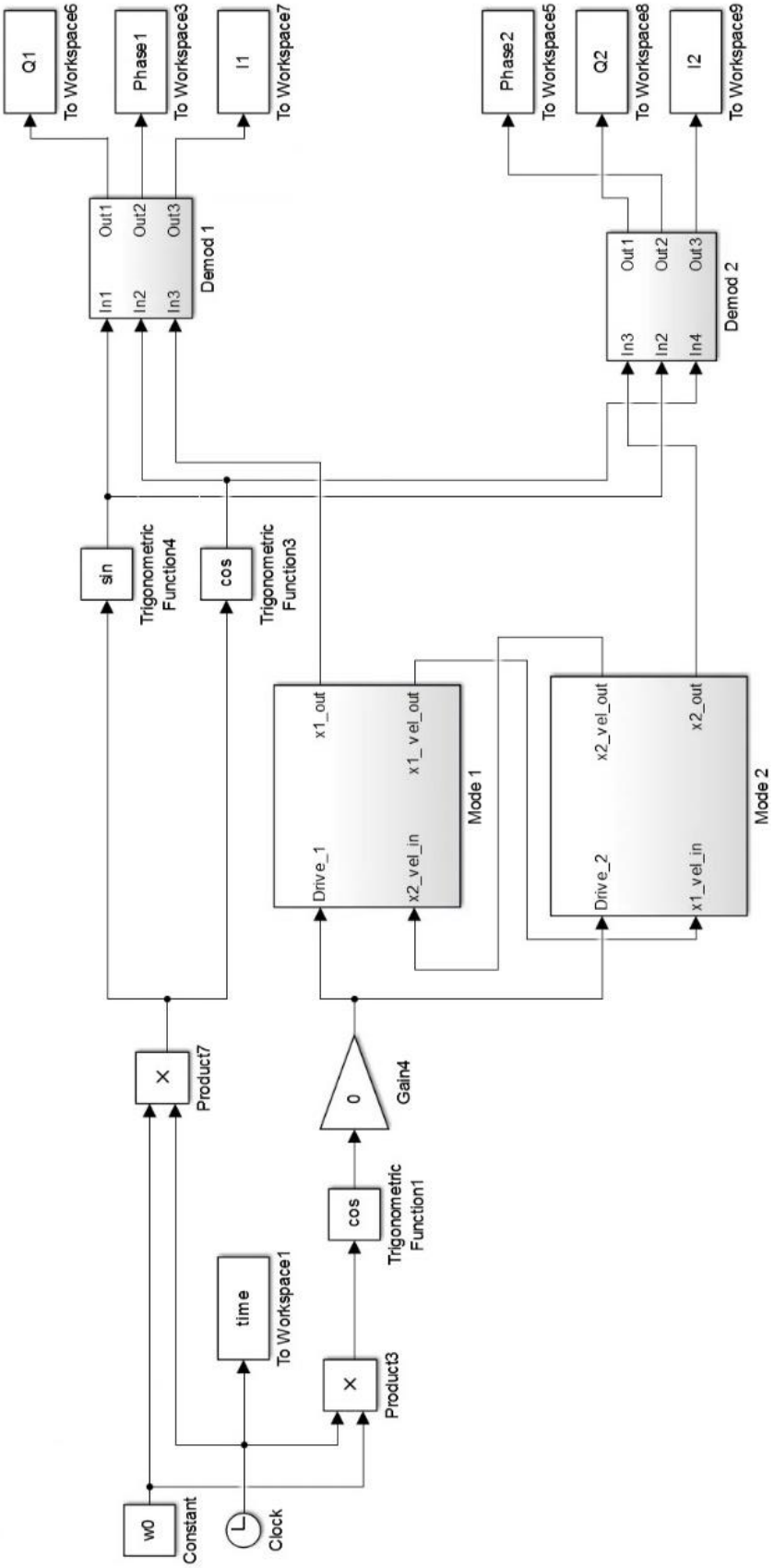

Figure 5.1 - Simulink model of the ring gyroscope

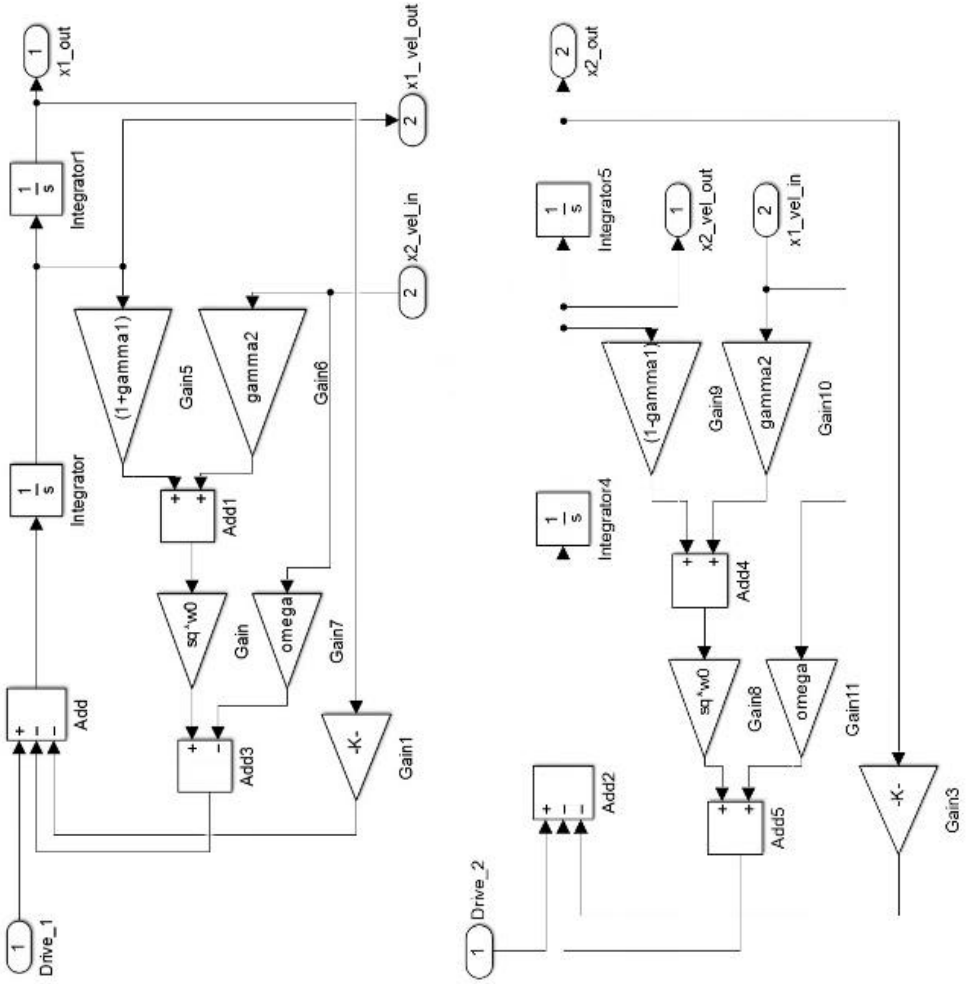

Figure 5.2 - The subsystems in the model of a ring gyroscope – as viewed from landscape, mode 1 subsystem is top and mode 2 subsystem is bottom

Figure 5.3 shows the effect of rate on the free vibration trajectory in modal space over a time period of 0.5s, where the vibration trajectory is described by the displacement of the ring relative to the two orthogonal modes x_1 and x_2 – as such, figure 5.3 can be considered to be the trace of a point on the ring during free vibration. With no rate applied the vibration trajectory takes the form of a straight line. However, on the application of rate this starts to rotate, where it should be noted here that due to the unforced nature of the vibration the magnitude of vibration can also be seen to be reducing as the vibration pattern rotates. It is this rotation that is proportional to the gyroscope input angle and is measured by the control scheme described previously.

This rotation arises from the transfer of energy between the two modes of vibration on the application of rate. This ‘beating’ energy transfer is shown in figure 5.4, which demonstrates the magnitude of vibration for two different applied rates. The increased frequency of energy

transfer at higher rates can be noted from these, and they therefore provide an excellent visualisation of the vibration behaviour described in section 1.3.

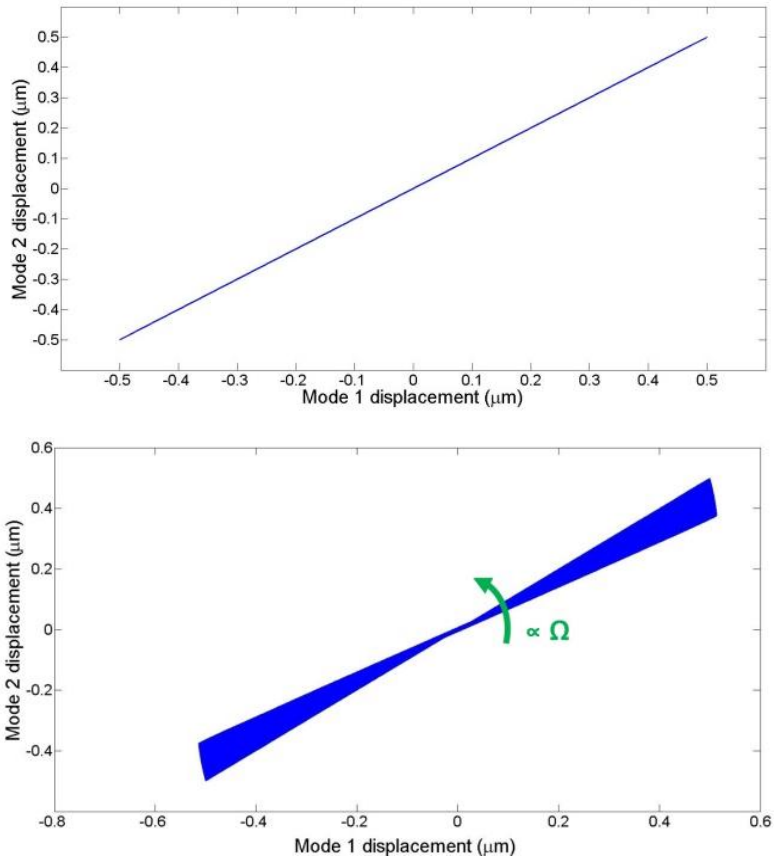

Figure 5.3 - The modal vibration pattern where no rate is applied (top) and a rate of 100rad.s^{-1} is applied (bottom)

With imperfections included in the modelling, changes in the vibration envelope become apparent. This is most clearly manifested in figure 5.5, which is a plot of the angle of the envelope of the modal vibration pattern (i.e. φ) with and without imperfections included at zero rate. With no imperfections included in the model, the vibration trajectory remains at a constant angle. However, as imperfections are introduced there is both drift and an oscillatory noise element, which appear in any measurement of rate. It is these sources of error that the control scheme must eliminate.

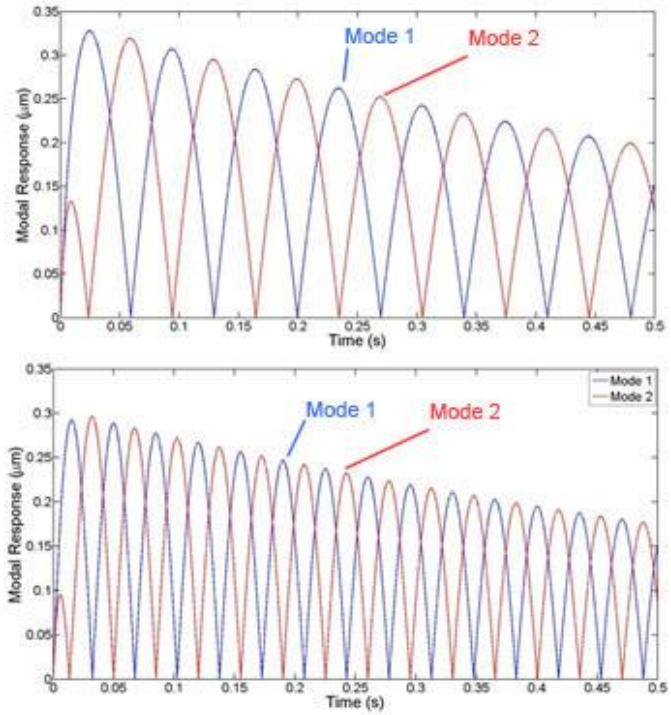

Figure 5.4 - Modal response with a rate of 50rad.s^{-1} (top) and 100rad.s^{-1} (bottom) applied

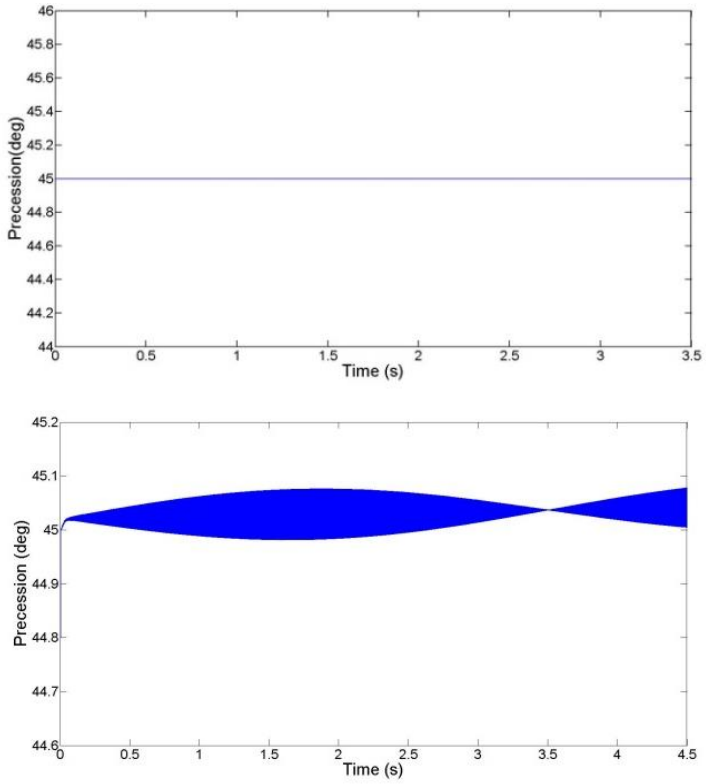

Figure 5.5 - Measured precession at zero rate without imperfections (top) and with all imperfections (bottom)

5.2. Control scheme proof of concept

Although it would be possible to make a relatively simple adaptation to the model described in section 5.1 to obtain a description of the gyroscope motion in terms of the orbital elliptic parameters, such a system would incorporate the fast-time components of vibration, which are of little interest when considering the control scheme proposed. Consequently, equations 3.58 to 3.61 have been modelled directly to demonstrate the feasibility behind the control scheme proposed while using a computationally efficient model.

In order to produce a computationally more efficient model, the equations of motion were scaled by defining each of the variables measured as a product of a scaling parameter and corresponding scaled variable, as shown below, where subscript *c* represents the scaling parameter for a given variable:

$$E_1 = E_{1c}\varepsilon_1 \qquad E_2 = E_{2c}\varepsilon_2 \qquad \varphi = \varphi_c\Psi \qquad \Phi_o = \Phi_c\Gamma_o$$

$$\overline{t} = t_c\tau \qquad \Phi_{Dn} = \Phi_c\Gamma_{Dn}$$

By substituting these into the equations of motion described previously and rearranging, equations 5.1 to 5.4 are derived. These provide a description of the gyroscope motion that can be modelled efficiently, thus considerably reducing the time required to run each simulation of gyroscope behaviour. The values assigned to the scaling parameters are provided by table 5.2.

Parameter	Value
t_c	10^{-5}
E_{1c}	10^{-12}
E_{2c}	10^{-15}
φ_c	10^{-2}
Φ_c	10^{-5}

Table 5.2 - Parameters used to scale the equations of motion

$$\dot{\varepsilon}_1 = -\omega_0 v_0(1 + \gamma_1 \cos(2\varphi_c\Psi) + \gamma_2 \sin(2\varphi_c\Psi))\varepsilon_1 t_c + \frac{\sqrt{\varepsilon_1}t_c}{\sqrt{E_{1c}}}F_1 \quad 5.1$$

$$\dot{\varepsilon}_2 = -\omega_0\xi \sin(2\varphi_c\Psi)\frac{E_{1c}t_c}{E_{2c}}\varepsilon_1 - 2\omega_0 v_0\varepsilon_2 t_c - \frac{\sqrt{E_{1c}\varepsilon_1}}{E_{2c}}F_2 \quad 5.2$$

$$\dot{\Psi} = \omega_0 v_0(\gamma_1 \sin(2\varphi_c\Psi) - \gamma_2 \cos(2\varphi_c\Psi))\frac{t_c}{\varphi_c} - \left(\frac{1}{2}\omega_0\xi \cos(2\varphi_c\Psi)\right)\frac{E_{2c}t_c}{E_{1c}\varphi_c} - \hat{\phi}\frac{t_c}{\varphi_c} - \frac{t_c}{\varphi_c\sqrt{E_{1c}\varepsilon_1}}F_3 \quad 5.3$$

$$\dot{\Gamma}_o = \frac{1}{2}\omega_0\xi \cos(2\varphi_c\Psi)\frac{t_c}{\phi_c} - \{\omega_0 v_0(\gamma_1 \sin(2\varphi_c\Psi) - \gamma_2 \cos(2\varphi_c\Psi))\}\frac{\varepsilon_2 E_{2c}t_c}{\varepsilon_1 E_{1c}\phi_c} + \frac{t_c}{\phi_c\sqrt{E_{1c}\varepsilon_1}}F_4 \quad 5.4$$

In order to prove the concept of the control system the model was simplified somewhat, with the drive forces assumed to be at resonance and not modulated by either the angle or any of the phases, as they are in the full equations of motion. Further, forcing on the orbital phase and precession angle was set to zero, as is the ideal condition. Therefore, the model contains stiffness imperfections – the targets of the control system – and damping imperfections as the only sources of error.

The parameters described by table 5.1 have again used in the model, but by scaling these with ε as described in chapter 3, the parameters in table 5.3 are obtained.

Parameter	Value
v_0	5
ξ (Hz)	1
$\check{\beta}$ (N)	1.4

Table 5.3 - Rescaled parameters

Figure 5.6 shows the Simulink model produced, with figure 5.7 showing the various subsystems – representing E_1, E_2, φ and Φ_0 (the major and minor axes of the ellipse, and the vibration precession pattern and orbital phase, respectively). From these figures, it can be

noted that PID controls have been used to simulate the application of forcing that can sustain E_1 (and therefore the gyroscope vibration) and null E_2 (the effect of modal mistuning) as required, whereas the inputs to F_3 and F_4 are constants of value zero. This fulfils the control scheme requirements on a basic level to allow proof of concept without the need for incorporating sources of error such as parasitic forcing between electrode pairs that, while they may occur on implementation of the control scheme, are not relevant to assessing the effectiveness of the control scheme described in reducing the effect of modal mistuning.

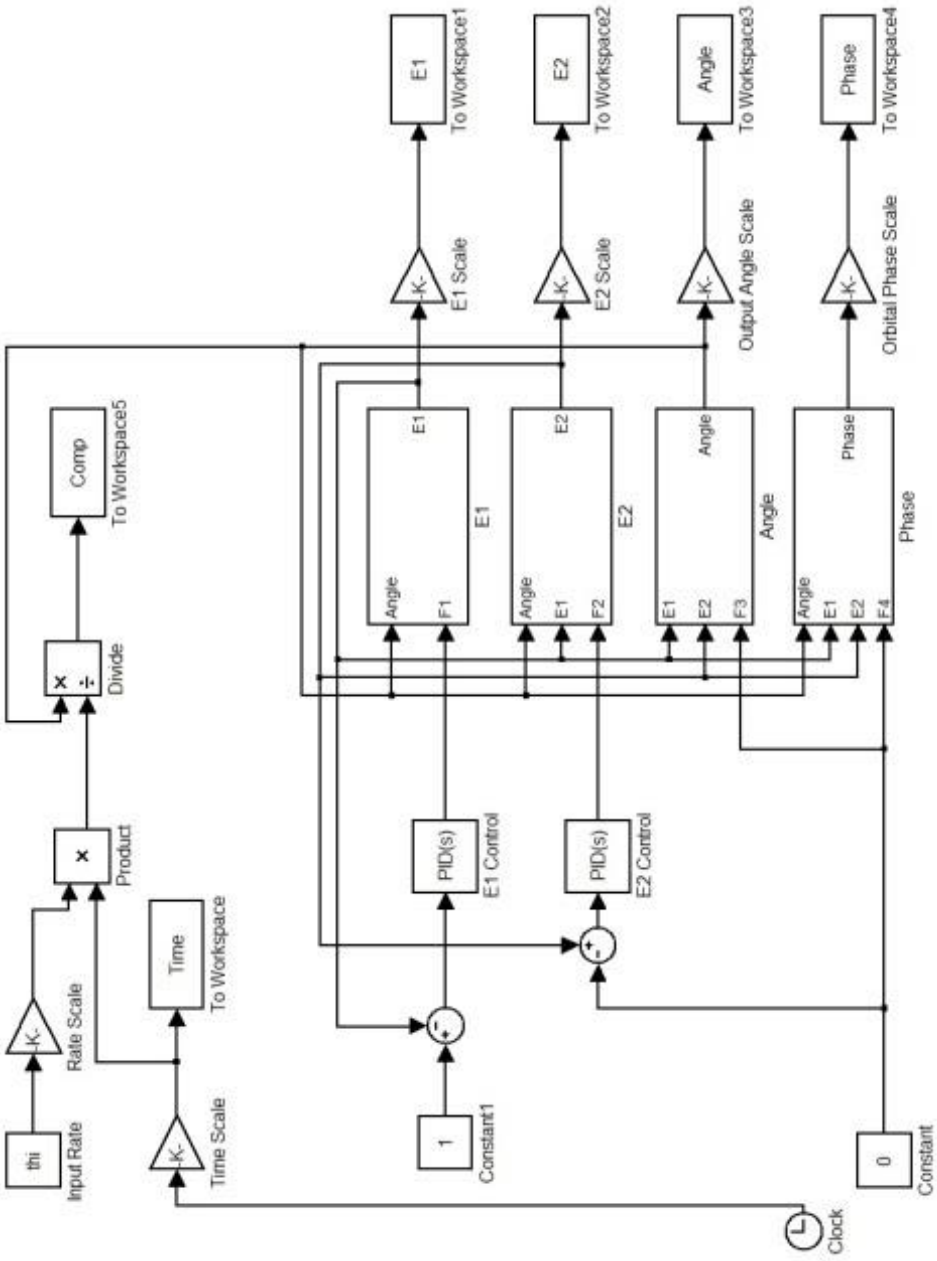

Figure 5.6. Simulink model of the control scheme

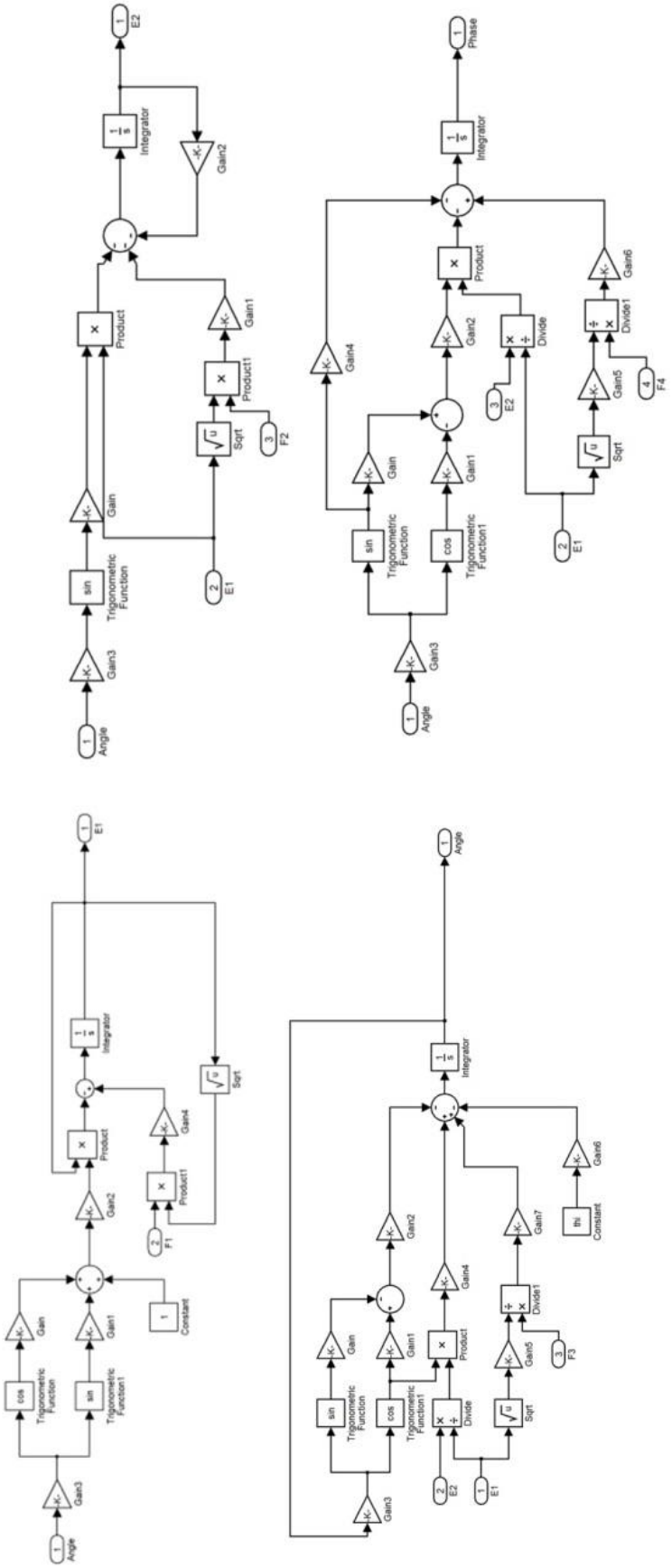

Figure 5.7. Subsystems in the simple Simulink model (clockwise from top left as viewed in landscape, E_1, E_2, φ and Φ_o)

With a rate of 10rad.s^{-1} applied, it can be noted from figure 5.8 that, while E_1 is sustained, E_2 can be driven to be close to zero. Although this is not a surprising effect considering the simplified nature of the model, the effect of this reduction in magnitude of E_2 on the accuracy of measured rate is evident from figure 5.9, where the ratio of measured rate to input rate is driven to be much closer to minus one, (where it has been established from equation 3.60 that minus one would be the ideal value). This improvement translates to a 100-fold improvement in measurement accuracy over a rate integrating gyroscope where E_2 is not controlled.

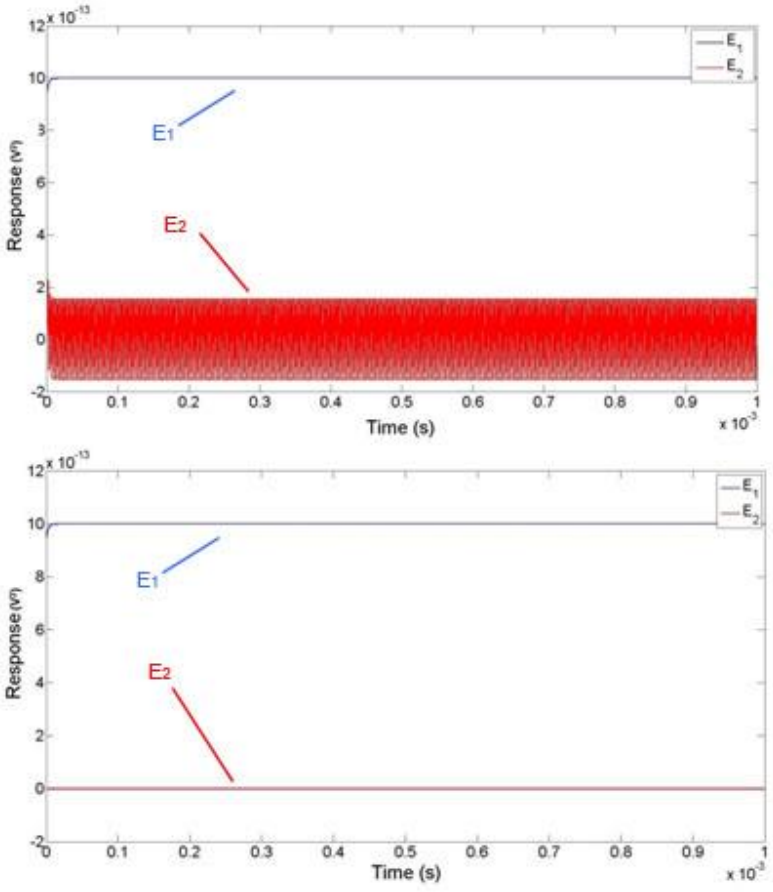

Figure 5.8 - E_1 and E_2 magnitude before E_2 control activation (top) and after control activation (bottom)

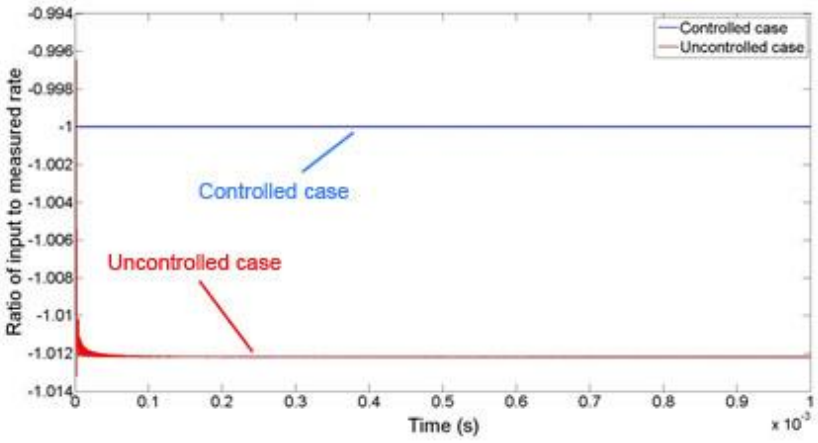

Figure 5.9 - Improvement in measurement accuracy on activation of the control for E_2

Figure 5.10 shows that the potential improvement occurs for a range of rates and levels of modal mistuning. It is clear from these that increasing rate has no effect on the mean ratio of input to output angle for both the case where E_2 is controlled and where it isn't, although activating the E_2 control loop drives the ratio closer to its ideal value. However, it is clear that, with no control loop, the ratio of input to output angle increases as modal mistuning increases. Nevertheless, the control loop is successful at consistently reducing this ratio back to its ideal value and as such can be deemed to be effective at all levels of modal mistuning that are likely to be encountered once the gyroscope has been successfully tuned.

Despite the promising results, the control scheme described by the model is very much idealised, and during operation there are likely to be further sources of inaccuracy, including drive mistuning and electronics delays. Such errors will result in the control scheme being less effective than predicted by this modelling. However, many of these inaccuracies are later shown by experimental results to be small, or to have an effect that is easily nullified.

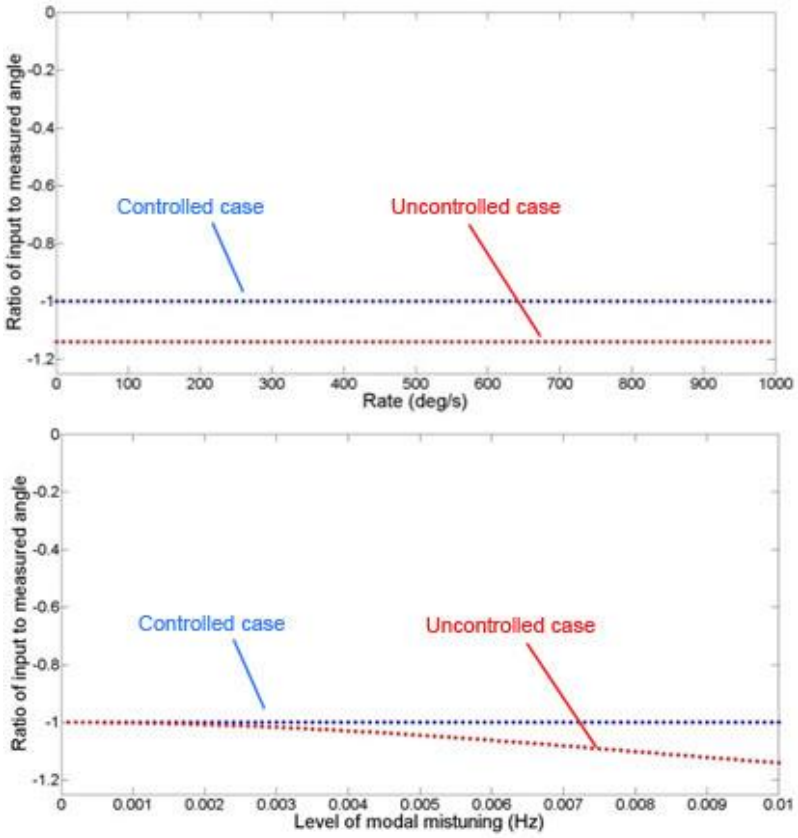

Figure 5.10 - Average ratio of input to measured angle for increasing levels of rate (top) and modal mistuning (bottom), input rate = 100rad.s^{-1}, where in both cases the uncontrolled case is red and controlled case is blue

Chapter 6. Initial gyroscope characterisation

6.1. Experimental set-up

The gyroscope is mounted upon a custom printed circuit board, which is in turn mounted on an Analog Devices ADSP-21469 processor for the purposes of signal analysis. For the testing of performance under rate, the gyroscope and associated circuitry are mounted upon a CUPE oscillating rate table, as shown in figure 6.1.

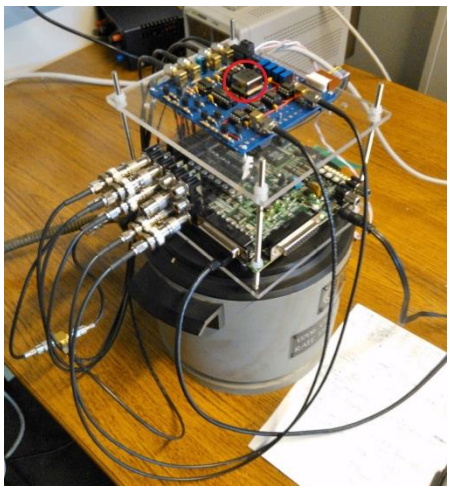

Figure 6.1 - The gyroscope (circled in red) mounted on a PCB, DSP board and CUPE rate table

For the purposes of data collection, gyroscope data is output via serial connection to a data file on a separate laptop by means of a custom-designed Matlab program.

The CUPE rate table can operate at rates of up to $300°s^{-1}$, although being an oscillating rate table the maximum rate is dependent upon frequency of oscillation. It is operated using a square wave signal, which produces the displacement input seen in figure 6.2. It should be noted that the input signal oscillates about zero degrees precession, whereas due to the drive conditions of the gyroscope the output will oscillate about 45°. However, the change in angle of the output, for an ideal gyroscope, should match that of the input.

For the purposes of any tests that involve the application of rate, the positive slopes are to be considered continuous inputs of positive rate, and the negative slopes continuous inputs of negative rate. The rate applied is further restricted by limitations on the data acquisition program loaded onto the control laptop, which allows a sampling rate of just 10Hz, (although the DSP board is of a sufficient standard for data processing). To obtain meaningful results (i.e. greater than 10 samples per period of applied rate in both the positive and negative

directions) the input signal frequency should not exceed 0.5Hz, thus allowing 1s of continuous rate to be applied in either direction per cycle. Considering the displacement limits of the rate table, this leads to a theoretical maximum rate of 300°s^{-1} being applicable. Despite this, the maximum rate that can be applied to the rate table is limited to approximately 80°s^{-1}. This limit arises because the momentum of the rate table at higher rates generates flexure in the gyroscope fixture at the points where the rate table direction of rotation changes between oscillations. This flexure in turn results in undesired movement of the gyroscope, which is likely to influence any measurements taken close to these points of direction change.

The information regarding direction change of the rate table is not necessarily distinguishable as the precise location of the direction change will be at some unspecified point between the two data points either side of the change in gradient. As such, during the analysis of data from the linearity and scale factor tests described in section 7.2 the most extreme data points of each sample of gradient have been disregarded.

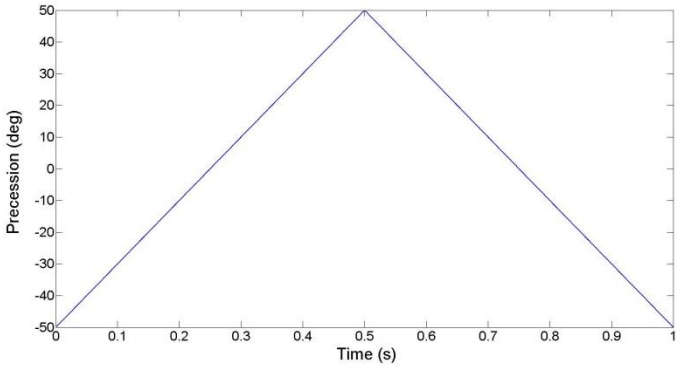

Figure 6.2 – A full cycle of a 1Hz 200deg.s^{-1} step input signal

All tests conducted on the gyroscope have been taken from the IEEE Standard 1431 [26]. These tests have been chosen as they are broadly in line with what is reported in the literature, and as such produce results that are comparable to existing research. In line with these standards, the output data to be measured is the recorded change in angle over one sample of time, with there being sufficient samples taken to ensure repeatability of the experiment.

With the experiment being somewhat limited by the performance of the rate table apparatus, for all experiments involving tests of increasing rate the range of angular rates tested was between 5°s^{-1} and 80°s^{-1} with an oscillation period of 2s. Although these rates are low for the usual applications of a rate integrating gyroscope, they are relevant as it is at low rates that errors caused by structural perturbations have the most noticeable effect of measured rate. It

was established in section 4.1 that a rate of 1rad.s^{-1} (approximately 57°s^{-1}) forms a rate threshold for performance of the gyroscope – as such, the range of 5°s^{-1} to 80°s^{-1} comfortably encloses this threshold and allows a demonstration of performance in the range of operating rates where such a control scheme is likely to be most necessary.

6.2. Bandwidth and frequency measurement

The Q-factor of a mode of vibration is a measure of damping, and can be defined as the ratio of maximum energy in the system to that dissipated during one radian of system oscillation [41]. It defines how underdamped a system is.

For a perfect freely-vibrating system, the modal response is maximised at the resonant frequency, with the response decaying symmetrically as the frequency reduces or increases. For a one degree of freedom system (i.e. a single mode of vibration), the Q-factor can be simply defined by equation 6.1, where B is the bandwidth and ω the resonant frequency of that mode of vibration. This also leads to the expression presented in equation 6.2 where τ is the decay constant of the system and is an indicator of the decay time of a resonating one degree of freedom system's vibration with no force applied. It will be shown shortly that this expression also applies to a gyroscope operating under resonance with two closely-matched modes of vibration.

$$Q = \frac{\omega}{B} = \frac{1}{2\zeta} \tag{6.1}$$

$$\tau = \frac{2Q}{\omega} \tag{6.2}$$

It is well-established that for MEMS gyroscopes to attain maximum sensitivity, both modes of vibration must have equal Q-factors [42]. Furthermore, uneven Q-factors introduce coupling between the modes of vibration that could adversely affect the measurement of rate. By taking the individual frequency sweeps of each mode it becomes possible to measure the bandwidth and resonant frequency of each one, using these to compare the Q-factors as well as to establish the modal frequency split, the average resonant frequency and the orbital phase at resonance.

The frequencies have been swept up from a frequency known to be lower than the resonant frequency, with the drive frequency being maintained for 1s before the frequency increase

(the rationale for this choice of drive time is related to the decay constant of the modes and is discussed later in this section).

The two modes were swept simultaneously as both modes will be activated simultaneously during operation. This differs from exciting each mode individually as it measures Q-factor along the sense axes – the axes of interest in the gyroscope. By measuring the Q-factor for each individual mode, measurements would not account for the contribution of the other mode to that mode's total damping, and this cross-damping may be a crucial contributor to the Q-factor for that mode.

Within the measurement for each mode's damping as taken using this method, information concerning these damping perturbations is encapsulated. Although these prove useful in the mathematical model, it is not possible to separate them out experimentally and the Q-factor can therefore only provide a measurement of how damped the system is, as opposed to providing an insight into the magnitude of these damping perturbations.

Plots of the modal responses from the frequency sweep are provided in figure 6.3. Each response is similar to what would be expected from a one degree of freedom resonator. However, other effects appear to be manifesting themselves in the plot shape, with the modal response rising more rapidly prior to the natural frequency being reached and falling away at a slower rate following this. A possible explanation for this could be electrostatic softening arising as a result of voltage bias or similar effects within the gyroscope structure. Although further investigation may be able to confirm whether this is a valid postulation, the behaviour and, as will be shown shortly, the measurements recorded are broadly similar to those expected indicating that the conclusions drawn from the frequency sweeps are valid irrespective of the causes of the irregular behaviour.

The frequency split when both modes are excited simultaneously is approximately 9mHz, which is of the magnitude required for the control scheme and is derived by finding the difference between the frequencies at the maximum response amplitudes for the frequency sweep for each mode. The average resonant frequency occurs at approximately 14258Hz, although it will be demonstrated later that this value can be variable. This level of tuning and resonant frequency closely matches that described by [11, 24].

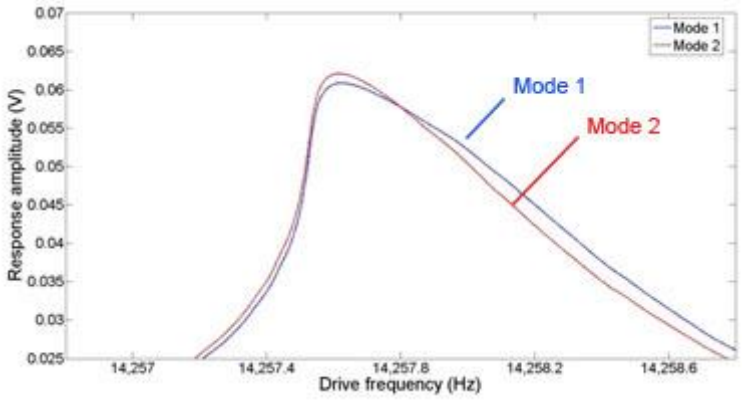

Figure 6.3 - Modal response plots following a frequency sweep of both modes of vibration

The results of the analysis of the plots in figure 6.3 are provided in table 6.1, where ω_n is the resonant frequency of mode *n*, *B* is the bandwidth of the modal response, *Q* is the modal Q-factor, τ is the decay constant and Φ_0 is the orbital phase.

Parameter	**Mode 1**	**Mode 2**
Max response	0.0609	0.0621
ω_n	14257.825	14257.816
B	0.7588	0.6650
Q	18790	21439
τ	0.4195	0.4786
Φ_0 at resonance	83.2954	84.7779

Table 6.1 - The parameters derived from the bandwidth measurements

The Q-factors were calculated using equation 6.1, with the frequency for each mode being measured as previously described and the bandwidth being calculated as the difference between the upper and lower frequencies indicated by the frequency sweep curve at half-power (that is, the maximum response divided by $\sqrt{2}$). Although it may reasonably be suggested that the irregular shape of the curves would influence the calculation, the Q-factors calculated were very close to the gyroscope's intended Q-factor of 2×10^4.

The uneven damping between modes is clear from these, where the Q-factors differ by 2649, with mode 2 having a slightly higher amplitude and smaller bandwidth. While this difference in Q-factor is unlikely to be of an order of magnitude that would produce an error more significant than that caused by the modal mistuning, its reduction may become a priority for later control schemes.

As alluded to previously, it becomes possible to use the information in table 6.1 to validate the frequency scans generated in the previous section. Gregory et al [42] state that, in order for a frequency scan to be reliable, the drive time at any given frequency must exceed the time constant τ to ensure that the decay of the associated peak does not affect the peak for the following frequency. Having a drive time of 1s per frequency sample, the frequency scan meets this condition.

The relationship between orbital phase and frequency is demonstrated by figure 6.4 with the average resonant frequency appearing to occur at $\Phi_o \approx 84^o$ where the drive phase for mode *n*, $\Phi_{Dn,}$ is $\Phi_{Dn} = 0°$ and $\Phi_o \approx -7^o$ where $\Phi_{Dn} = 90°$. It can be shown that the orbital phase at resonance rotates according to the drive phase chosen, with resonance occurring at $\Phi_o \approx -\Phi_{Dn} + 84°$. It can be noted here that the irregular difference of 84^o is likely to be the result of electronics delays during implementation of the control scheme and other similar effects. The orbital phase at resonance is nevertheless consistent and can therefore be used in the creation of a phase locked loop.

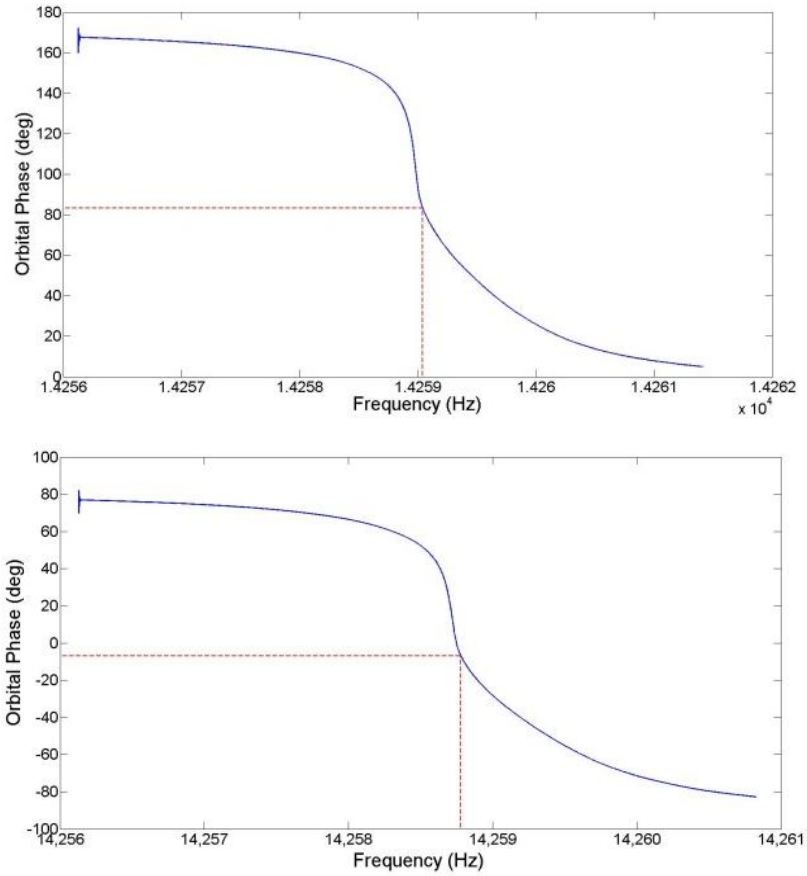

Figure 6.4 - Orbital phase following a frequency scan with a drive phase of 90deg (top) and 0deg (bottom), with the position of resonance marked on as a red dotted line

A further point to note is that the average resonant frequency fluctuates slightly with time, a phenomenon demonstrated by figure 6.5. This variation is likely to be due to a number of factors, such as environmental changes. However, the orbital phase at resonance does not change, with the result that the PLL can be used with constant effectiveness regardless of the precise resonant frequency.

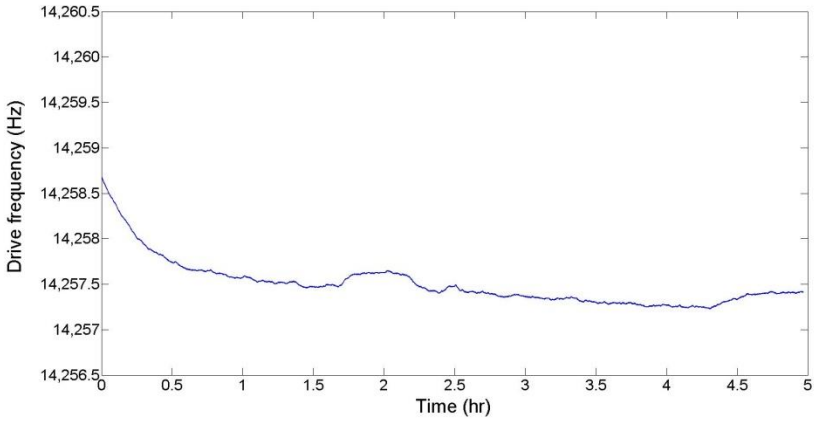

Figure 6.5 - The change in frequency over time for a stationary gyroscope

6.3. Phase locked loop performance

It has been established that the orbital phase can be used to measure the proximity of the drive frequency to the average resonant frequency of the two modes of vibration. In order to take advantage of this, the simple phase locked loop has been derived. With the appropriate gains selected, it is evident from figure 6.6 that, for a stationary gyroscope, the drive frequency can be locked to within a few mHz of the average resonant frequency in a time of approximately 0.2s. Although the locking time is relatively long, the drive frequency is locked to within 18mHz of the average resonant frequency. This is a very close match and of the same order of magnitude as similar errors in the system, such as the modal mistuning, which has been shown previously to be 9mHz.

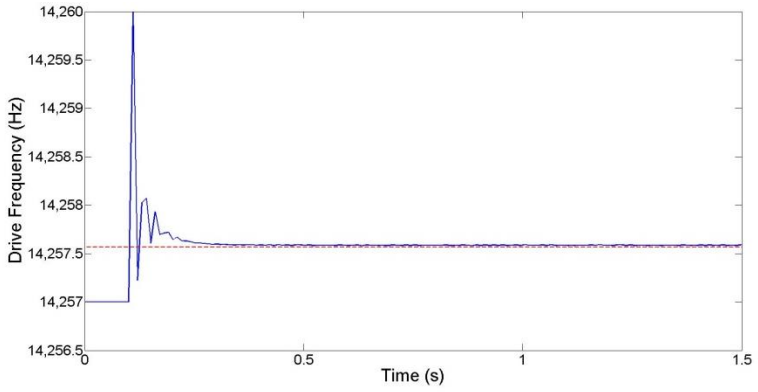

Figure 6.6 - Drive frequency response on activation of the PLL, where the red dotted line represents the average resonant frequency of the two modes of vibration

6.4. Gain control

6.4.1. Control application

Owing to delays caused by the electronics within the DSP board, the phase of the drive signal is offset from that of the reference wave. As such, any forcing applied is not applied in the required direction. However, this is a constant error and can easily be rectified by means of a simple compensation. This compensation consists of, prior to the transmission of the drive wave to the gyroscope, a phase offset that is the negative of the drive offset being applied to the drive signal.

The box plots in figure 6.7 show that the mean drive phase remains very small as rate increases, validating the effectiveness of the phase locked loop in sustaining the drive phase at

zero. It should be reiterated here that the rate applied has been adjusted for the Bryan factor – that is, the ratio of input precession to the precession of the vibration pattern.

Although there is a marginal increase in the distribution of data, indicating that the drive phase begins to fluctuate slightly, this nevertheless remains very small and is therefore unlikely to have a significant effect on the performance of the gyroscope. With the outliers reaching a maximum of approximately 0.08° it becomes possible to conclude that nulling the drive phase error by the application of a constant drive offset is an effective way of eliminating constant drive phase errors.

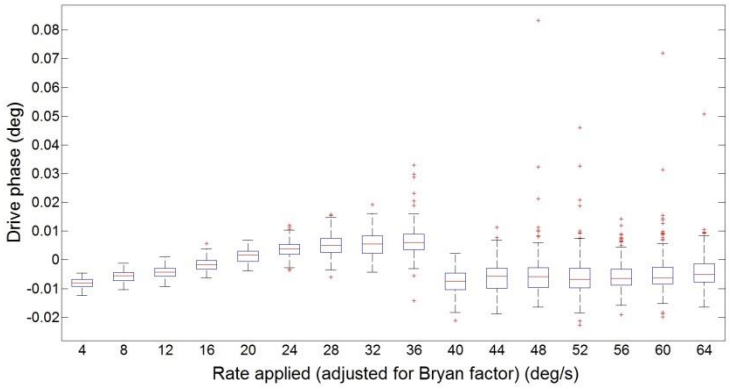

Figure 6.7 - Box plots of drive phase magnitude under increasing rate

As has been described previously, the term E_1 provides a measure of the major axis of an ellipse that is aligned with the trajectory of the ring vibration, while E_2 is a measure of the minor axis of the same ellipse and is proportional to the mistuning between the ring's modes of vibration if E_1 is constant. As such, in order to null the effect of modal mistuning, the control scheme must sustain E_1 at a constant value while nulling E_2. For these tests, the magnitude of E_1 chosen such that the vibration amplitude will be large but within the limits defined by the structure of the gyroscope

The success of the control scheme in achieving these requirements can be noted from figure 6.8, which shows that E_1 is sustained at a value of $2.5\text{x}10^{-3}\text{V}^2$ with minimal variation, while the ratio E_2/E_1 is reduced to a mean value of $0.6\text{x}10^{-3}$ within 3s, which roughly translates to a 120-fold reduction in the size of the ratio. The PID control locks to these values within 3s

Although the set-point for E_2 is zero, this is not attained, because the magnitude of forcing required to null E_2 completely during rotation is too precise for the control loop to handle, and the value of E_2 subsequently oscillates about zero. Nevertheless the reduction in magnitude of

the ratio E_2/E_1 is considerable with the oscillations having small fluctuations about zero – this is likely to represent a large, although not perfect, reduction in the effect of modal mistuning.

The standard deviation of each set of measurements has been chosen quantify the level of fluctuation about the mean for each invariant, and hence assess the stability of the control loop. E_1 is controlled to a standard deviation of 7.13×10^{-8} V^2, which translates to a deviation of just 0.0029% of its required value. When considered alongside the measurements of amplitude, this demonstrates that the control scheme is effective in sustaining a constant value of E_1, both in terms of amplitude and stability. However, the level of amplitude reduction of E_2/E_1 is not as great as that demonstrated in the modelling in section 5.2, with it having a standard deviation of 4.71×10^{-4}, where its mean value is 0.6×10^{-4}. This behaviour can be noted in figure 6.9. While this appears to suggest that the sustained value of E_2 is relatively volatile about its mean, the large reduction in amplitude of the ratio E_2/E_1 ensures that this ratio is at all times considerably smaller than its uncontrolled value, and hence the control scheme is reducing the amplitude of E_2/E_1 at all times.

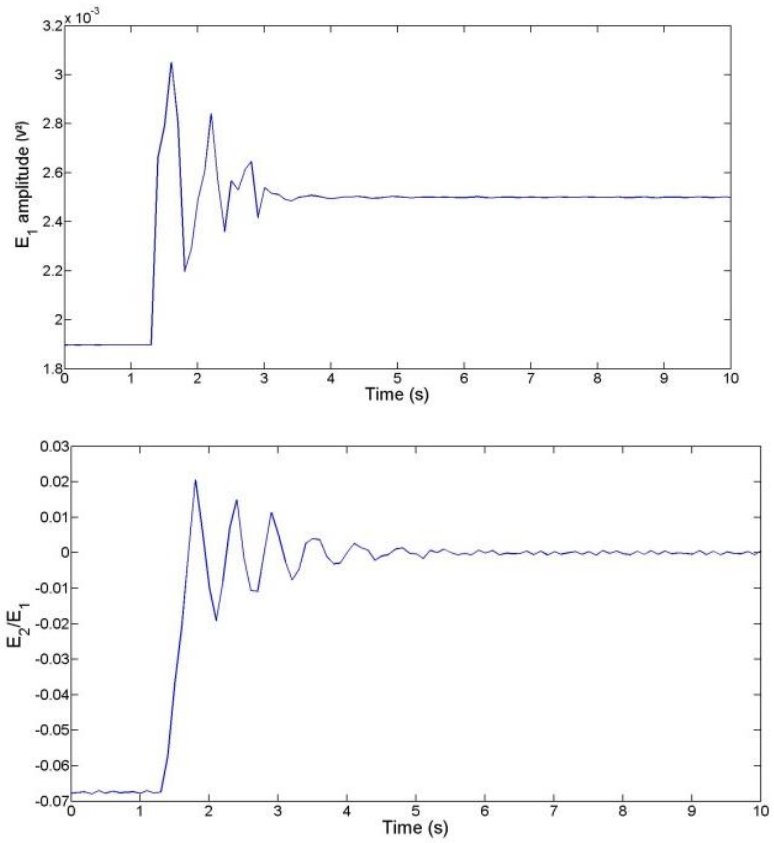

Figure 6.8 - The amplitude of E_1 (top) and the ratio E_2/E_1 (bottom) for a stationary gyroscope as the control is activated

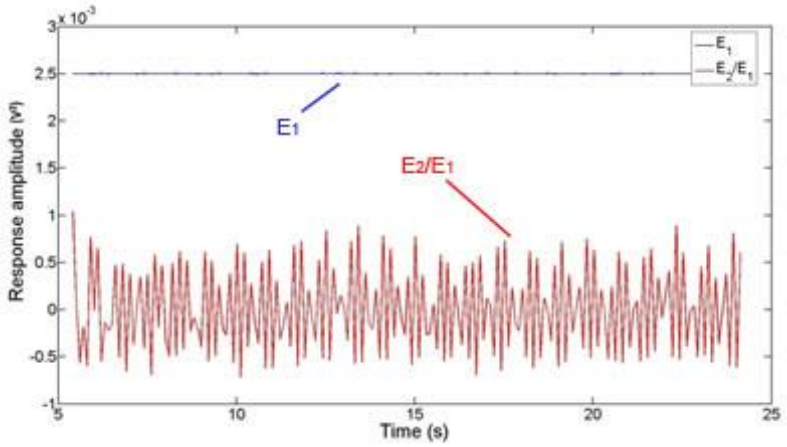

Figure 6.9 - A plot of E_1 and E_2/E_1 for the time period following the settling of the control loops showing the large variation in the amplitude of E_2/E_1

This large variation of E_2 about the mean is likely to be in part due to the inability of the PID control to drive the value of E_2 to precisely zero, compounded by electronics delays, drive mistuning and imprecision in the design of the drive electrodes. Perhaps most significantly, the unwanted influence of forcing from other controls could also reduce the impact of the direct forcing upon the value of E_2.

Nevertheless, the maximum amplitude of these fluctuations is approximately 1×10^{-3}, which corresponds to a minimum reduction of ratio size by a factor of 70 at all times, with the mean reduction being closer to a factor of 120, as discussed previously. The reduction in the size of E_2/E_1 is considerable and, where a control is designed such that the forces exerted do not interfere with the measurement of angle, will reduce the effect of modal mistuning on the accuracy of the gyroscope by a corresponding amount, which will yield a significant increase in gyroscope accuracy. However, this test considers only a stationary gyroscope. With the application of rate, the forcing changes and this results in some deviation from the set-point. This effect is studied further in the next section.

6.4.2. Performance under rate

It has already been established that when rotation is applied to the gyroscope, the forcing acting upon the parameters of the ellipse change. Consequently, the PID loops controlling E_1 and E_2 must react to this change. Figure 6.10 is a series of box plots showing the behaviour of these parameters under increasing rate. Each boxplot was derived from the measurement of a series of data recorded at the indicated rates, measured over a minimum of 10 cycles of rate

table oscillation to ensure a suitably large set of data was recorded. The ideal PID control should maintain each of these at a constant value, with very little distribution of data.

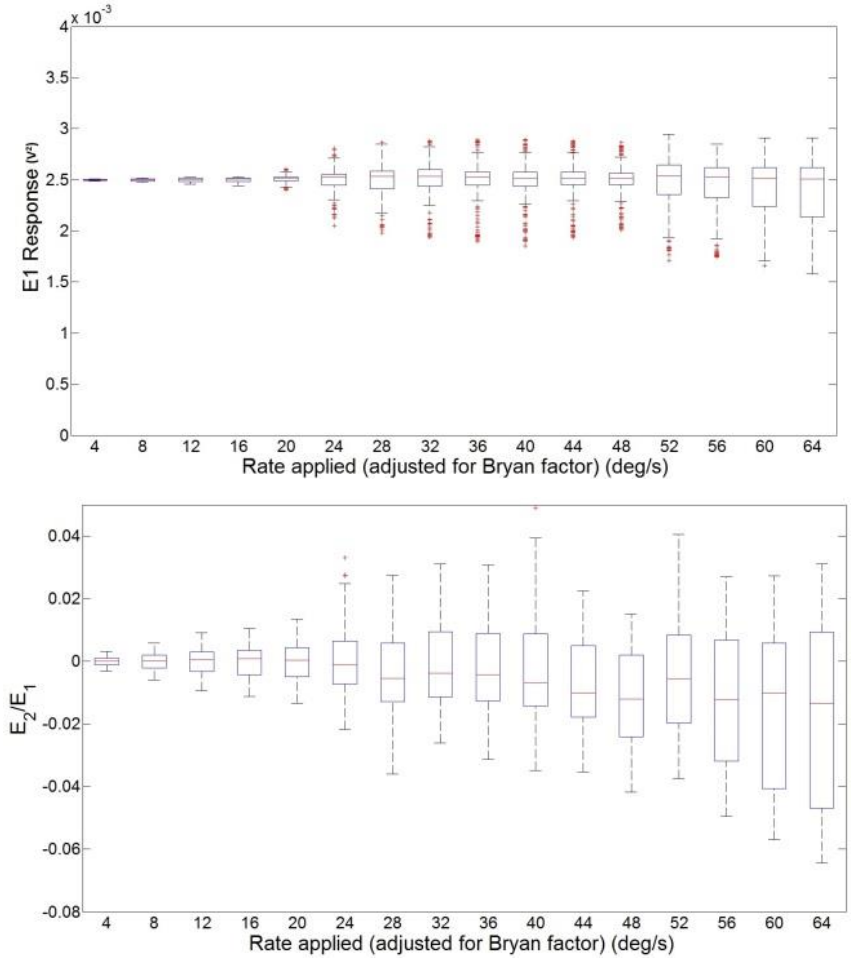

Figure 6.10 - Boxplots of samples of E_1 (top) and E_2/E_1 (bottom) as applied rate increases

While the control is able to sustain the mean value of E_1 under increasing rate, the distribution of data increases. This relationship is almost proportional to rate, as can be noted from the plot of standard deviation in figure 6.11. Despite this increase in the distribution of data, the maximum standard deviation for E_1 for the rates tested is 3.9×10^{-12}. This is approximately 10% of the set point of E_1. Although this is a relatively large number, figure 6.10 indicates that the median does not fluctuate considerably, which in turn indicates that the control is succeeding in maintaining E_1 at a set value.

It is probable that any deviation from the mean is purely a result of applied rate. It has already been established that applied force is dependent on the ellipse angle φ, and it is this dependence that causes the increasing distribution of data at higher rates – the gyroscope

covers a larger angle as rate is increased, thereby changing the forcing required to sustain E_1 at an appropriate value.

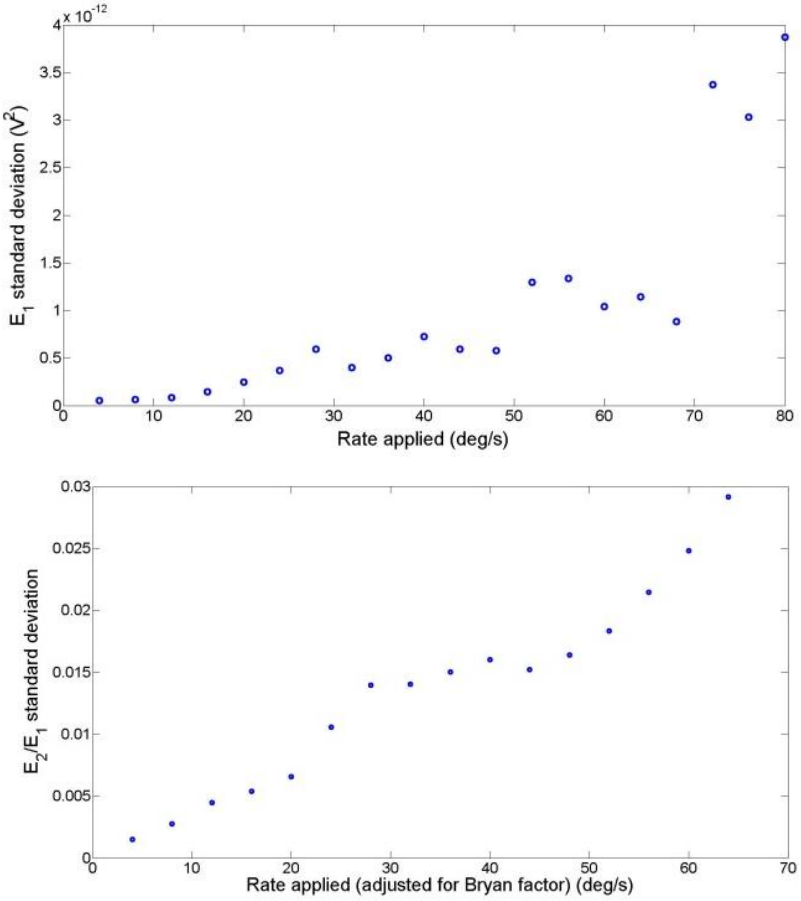

Figure 6.11 - Plots of the standard deviation of E_1 (top) and E_2 (bottom) with increasing rate

It is clear from figure 6.10 that the control is less effective for the ratio E_2/ E_1, with figure 6.11 showing that the standard deviation in this case increases with rate considerably faster than in the case of the control for E_1. Nevertheless, it was established in the previous section that a large deviation is expected for this ratio even for the stationary gyroscope. Figure 6.12 is a series of boxplots of E_2/ E_1 and the associated standard deviation when E_2 is uncontrolled. In this case, a condition is applied to the second electrode whereby there is no forcing on the ellipse angle.

In the controlled case the mean value of the ratio E_2/ E_1 is reduced significantly, although the standard deviation remains of a similar order of magnitude. An overall reduction in the mean value of E_2/ E_1 is useful in that it generally reduces the effect of modal mistuning on the measured angle. However, the large deviation of data may somewhat reduce this effect.

While it may be possible to reduce the deviation in the value of E_2/E_1, the application of forcing to this parameter has a detrimental effect on precession measurement, as detailed in the following section.

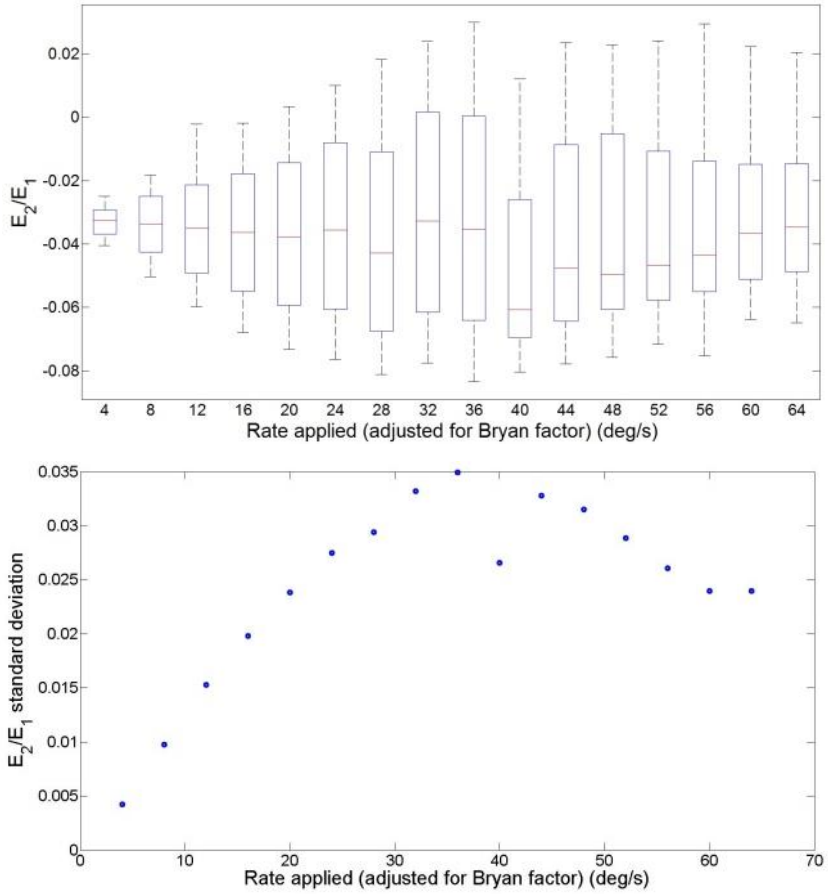

Figure 6.12 - Boxplots of E_2/E_1 (top) and the associated standard deviation (bottom) as rate is increased

6.4.3. Effect on precession measurement

From equation 3.60 it is apparent that the forcing acting on the precession of the ellipse, φ, is itself dependent upon φ. Therefore, any change in angle will result in a change of forcing, affecting the measurement of precession. The result is that the forcing acting upon the ellipse angle, even if the gains do not change, is not simply a bias that can easily be accounted for.

The effect of forcing can be shown to manifest itself in the measurement of ellipse precession by figure 6.13. This figure consists of computer-generated plots of the input displacement pattern placed over plots of the measured precession. While the input oscillates about the zero point, the output oscillates about the 'zero' for the gyroscope, which in this case is a precession angle of 45°. Therefore, the bias for each plot has been adjusted to best match that of the output as this is of little concern with the control scheme, providing that it is constant.

While velocity is applied in the form of a square wave, forming the ‘sawtooth’ displacement output shown, the output precession deviates significantly from this pattern when E_2 is minimised. There is no discernible angle information and it is clear that the forcing used to null E_2 has a considerable effect on the precession, as discussed in previous sections. The effect of forcing on precession measurement is compared to other control-based error sources in section 7.1, but it is clear that it will be a huge source of error if this an E_2 control is implemented on the existing gyroscope architecture. However, by applying the force nulling scheme described in section 4.4 instead, it becomes clear from figure 6.13 that the effect of forcing on the precession angle can be nulled to a great extent by choosing the appropriate drive electrode gains.

This outcome is useful as it demonstrates that it is possible to reduce the effect of forcing acting on a given ellipse parameter. With the appropriate gyroscope design, which is discussed further in chapter 8, it becomes possible to use the drive electrodes to null unwanted forces. However, the electrode layout of the gyroscope used in this project precludes this from being implemented alongside the control scheme described.

A further advantage to this behaviour is that the success of the force nulling scheme goes some way to validating the forcing conditions described in section 3.2.

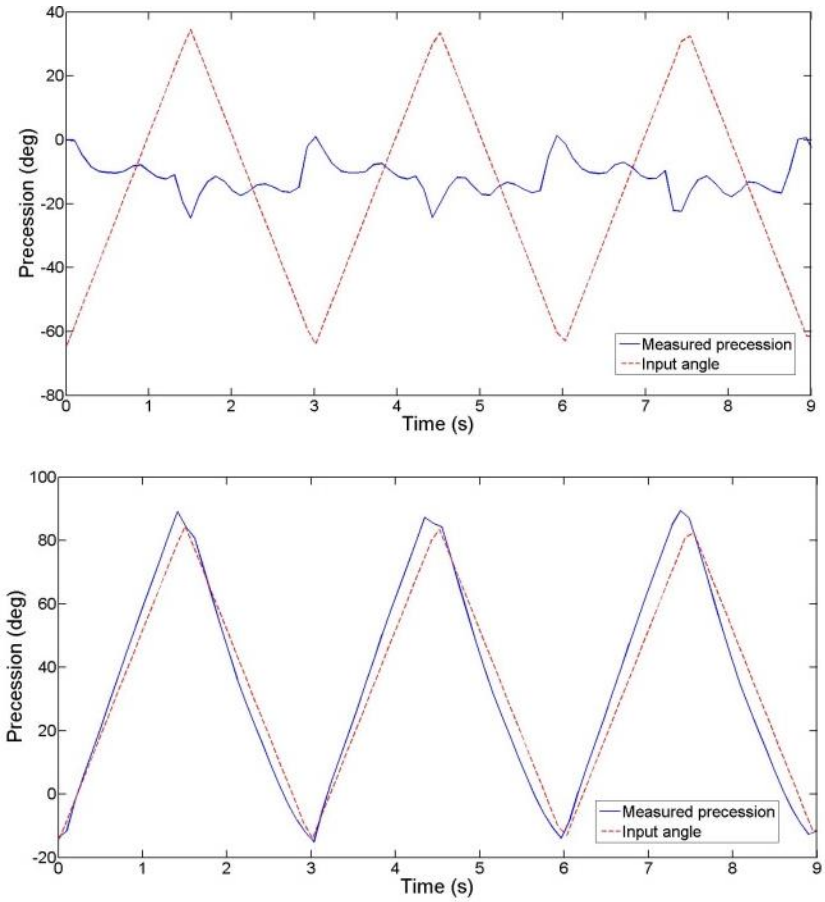

Figure 6.13 - The measured precession (blue line) and input angle (red dashed line) where E_2 is controlled (top) and where F_3 is controlled (bottom)

6.4.4. Effect on modal and orbital phase (and phase locked loop)

According to equation 3.60 any forcing used to excite the gyroscope also acts upon the orbital phase unless an appropriate forcing condition is applied. Further, the orbital phase is modulated by φ, this effect being particularly compounded by the requirement for a large E_1 in comparison to E_2. This forcing effect results in the orbital phase at resonance for a rotating gyroscope being forced to a different value than that for a stationary gyroscope.

The effects of forcing and ellipse angle as the gyroscope is rotated are clearly manifested in the orbital phase shown in figure 6.14, which displays samples of orbital phase and frequency when a rate is applied that alternates between ±50deg.s^{-1} at a frequency of 0.5Hz. It is clear from these that even at such low rates, there is a regular deviation from the mean drive frequency of approximately 100mHz, which is clearly considerable considering that it has been established that the modal mistuning is approximately 9mHz. This large variation is supported by this frequency sample having a standard deviation of 73.2mHz which, when it is taken into account that there may be some deviation of the mean from the ring's resonant

frequency (a phenomenon that it is not possible to accurately measure due to the variation in resonant frequency described previously), may result in adverse effects on the phase locked loop.

With the orbital phase displaying a regular variation of ±0.5° it is clear that the orbital phase is very sensitive to frequency change and the nulling of any forcing acting upon the orbital phase is necessary to reduce the variation in frequency as rate is applied.

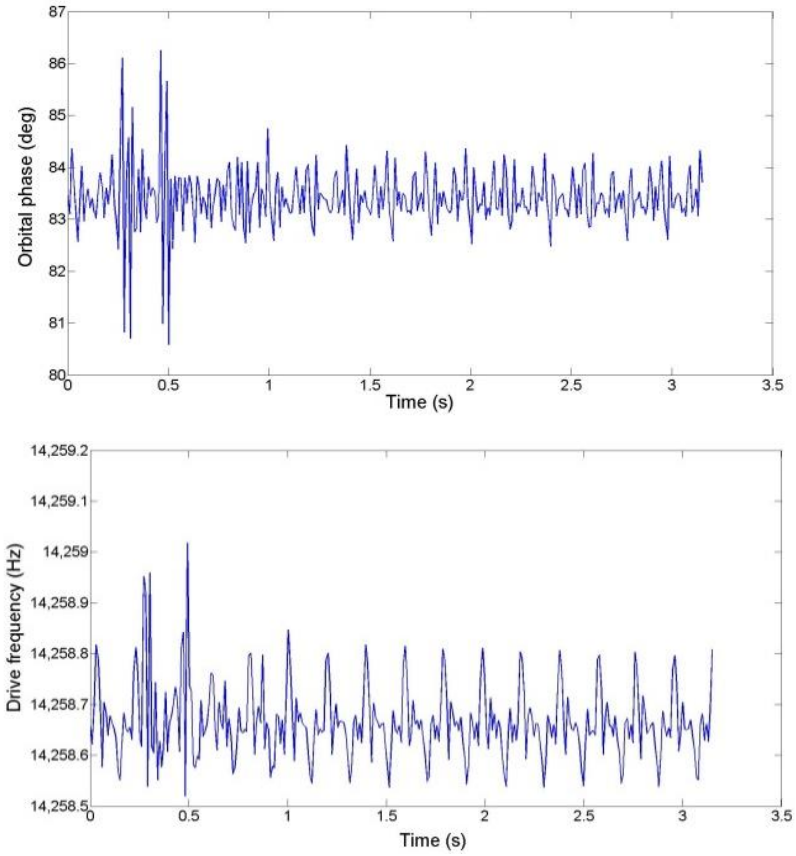

Figure 6.14 - The orbital phase (top) and drive frequency (bottom) as the PLL is used to control frequency while an alternating rate of ±50deg.s^{-1} is applied to the gyroscope and the ratio E_2/E_1 is controlled

This behaviour is observed across a range of rates, where figure 6.15 shows the standard deviation of the frequency samples where applied rate is increasing. It clearly shows that increasing rate leads to the increasing distribution of drive frequency from the mean, due to the effect that forcing has on orbital phase. It should be noted here that the mean has not been considered in demonstrating the effect of rate on orbital phase past that given in section 6.3. This is due to changes in the resonant frequency that occur during testing and that have been described in section 6.2.

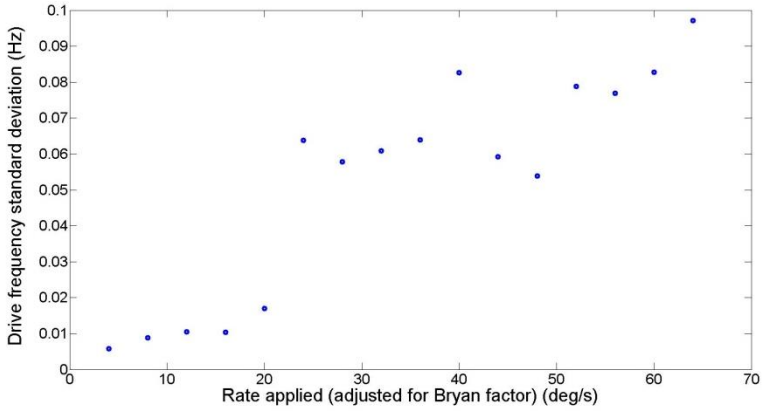

Figure 6.15 – Standard deviation of drive frequency as applied rate is increased where the ratio E_2/E_1 is controlled

When the ratio E_2/E_1 is controlled there is significant effect on the drive frequency due to the forcing affecting the orbital phase at resonance. However, it can be noted from figure 6.16 that where the forcing is applied such that F_3, the forcing acting upon the ellipse precession, is zero (i.e. no forcing on φ) the standard deviation of the drive frequency is much smaller at higher rates, indicating that the applied rate has less of an effect on the orbital phase at resonance with this condition applied.

In addition, the gradient of the pattern appears to reduce at higher rates. This provides a preliminary indication that increasing the rate further would cease to have any effect. However, this postulation requires further investigation with a rate table that is capable of higher rates.

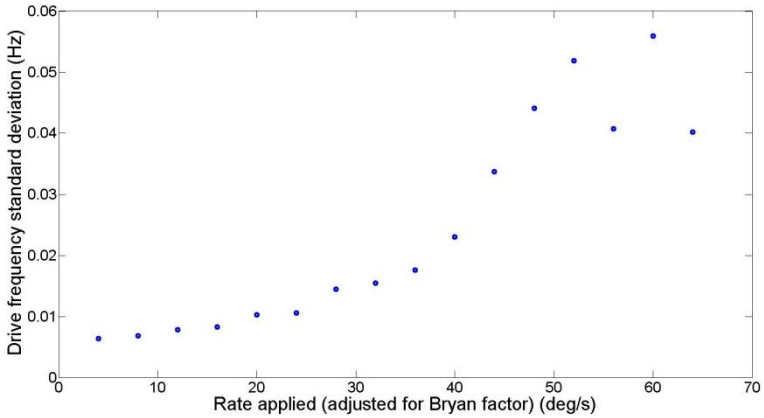

Figure 6.16 - Standard deviation of drive frequency as applied rate is increased where F_3 is controlled

This demonstrates that the use of the orbital phase in the creation of a PLL would require the nulling of forcing acting on it. While this appears to add a layer of complexity to the control scheme, the orbital phase is the most viable measurement for generating a PLL as there is no

forcing information concerning the force acting upon the first mode phase, which would be the only viable alternative available from the control scheme. Furthermore, the first mode phase would excite the ring at the resonant frequency of the first mode of vibration, rather than the average, which would have a detrimental effect on gyroscope accuracy where modal mistuning is present, as it would generate modes of vibration of differing amplitudes.

Chapter 7. Gyroscope characterisation

7.1. Choice of condition for characterisation

The gyroscope used in this project has been fully characterised, as will be demonstrated in this section. However, it is clear from previous sections that it is not possible to fully implement the control scheme described due to limitations regarding the architecture of the gyroscope. Consequently, it is necessary to select the operating conditions that would provide the most accurate interpretation of its performance as a rate integrating gyroscope.

This translates to a choice of three conditions – minimise the value of E_2 in order to reduce the effect of mistuning on angular rate, eliminate the forcing on the ellipse angle or eliminate the forcing on the orbital phase.

As the objective of a rate integrating gyroscope is to measure angular displacement, the accuracy of this measurement will be used to determine the condition under which the gyroscope behaves with the most accuracy.

It is clear from figure 6.13 that the control loop for E_2 has a large effect on the output precession. Further, it has been established in section 6.4.4 that the application of forcing such that the forcing on the precession, F_3, is zero-vastly reduces the effect of forcing on the orbital phase as well as the measured precession. Therefore, it is apparent that the gyroscope measures with the greatest accuracy if the force on the precession angle is minimised as a priority.

As such, for the gyroscope characterisation with existing architecture the control scheme will maintain E_1 at a constant value, while nulling the force on the measured precession.

7.2. Angle measurement performance

7.2.1. Scale factor

The gyroscope scale factor is the ratio between the change in input angle and the change in angle as indicated by a line fitted to the output data by the least squares method. It is also possible to use this data to measure both the asymmetry of the gyroscope – the difference between the scale factor when a positive and when a negative rate is applied – and the linearity of the gyroscope.

The scale factor is defined as the gradient of a line fitted by the least squares method to a plot of the input against output data [26]. Thus, for a MEMS gyroscope it is the gradient of a line fitted by the least squares method to a plot of the input versus output rate.

However, to gain an insight into the behaviour of how the scale factor changes as rate is increased, it becomes useful to first take the scale factor from within a set of measurements at a constant applied rate. By taking the scale factor as the gradient of a line fitted to a plot of input angle against measured angle, where the angle is measured for *k* samples and $\hat{\varphi}_i$ is the input angle at sample *i* and $\overline{\varphi}_i$ the output according to a line fitted to the output data, the scale factor can be defined as:

$$SF = \frac{1}{k}\sum_{i=1}^{k}\frac{\left(\overline{\varphi}_{i+1} - \overline{\varphi}_i\right)}{\left(\hat{\varphi}_{i+1} - \hat{\varphi}_i\right)} \tag{7.1}$$

Figure 7.1 shows the change in scale factor with rate. Although the calculation of scale factor for each rate is not in line with the standards in [26] it serves as a useful indicator of how scale factor changes with increasing rate and emphasises some otherwise less detectable trends.

At lower rates, below approximately 20°s^{-1}, the scale factor is considerably away from the ideal of one, and exhibits a considerable increase as rate increases. Following this the scale factor becomes relatively constant for both positive and negative rates, although it does not reach its ideal value of 1. This is likely to be because the control scheme is unable to eliminate all errors in the system – damping imperfections are not addressed by this control scheme and the forcing serves to minimise, but not completely eliminate, the effect of modal mistuning. As such, it is likely that these will manifest in some assessments of performance, including the measurement of gyroscope scale factor. For full gyroscope operation, a consistent and constant scale factor away from one is acceptable as this would require a simple adjustment factor to be implemented into the control scheme.

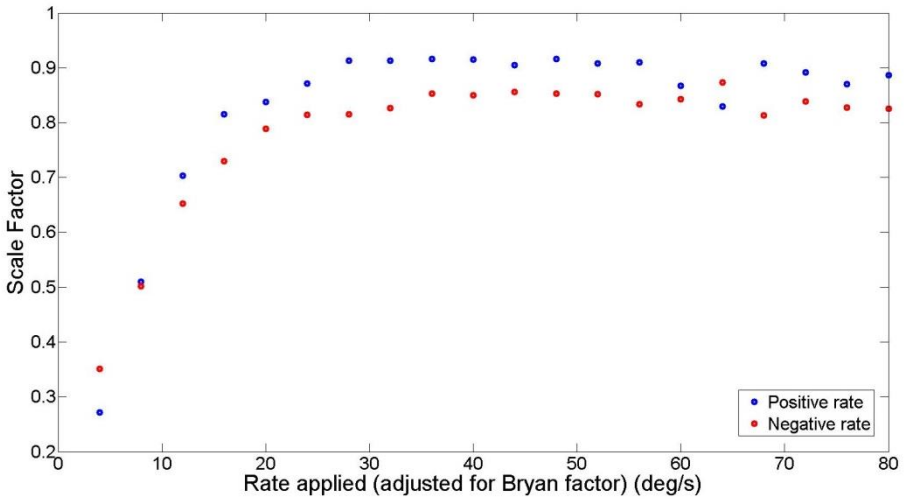

Figure 7.1 - The scale factor measured as rate increases for positive rate (blue markers) and negative rate (red markers)

The low rate behaviour is a manifestation of the dominant behaviour that angular rate exhibits over other imperfections as it increases – it can be noted from equation 3.60 that the rate must exceed any forcing acting on the ellipse, as well as the effects of damping and stiffness perturbations.

With damping being small on account of the high Q-factor, it can be noted from the box plots in figure 7.2 that, at these low rates, the ratio E_2/E_1 – that is, the ratio of minor to major ellipse axis - has a varying mean and standard deviation as rate is increased. As the modal mistuning is a constant value, a change in E_2 can be attributed to the effect of forcing on E_2. Subsequently, it must be concluded that a combination of modal mistuning and forcing on E_2 influence the measurement of angle at low rate, with the remnants of forcing on angle also likely to be having an effect despite the force nulling routine. This may be resolvable by switching between rate mode at low rates and rate integrating mode at higher rates, where the higher bandwidth would prove advantageous.

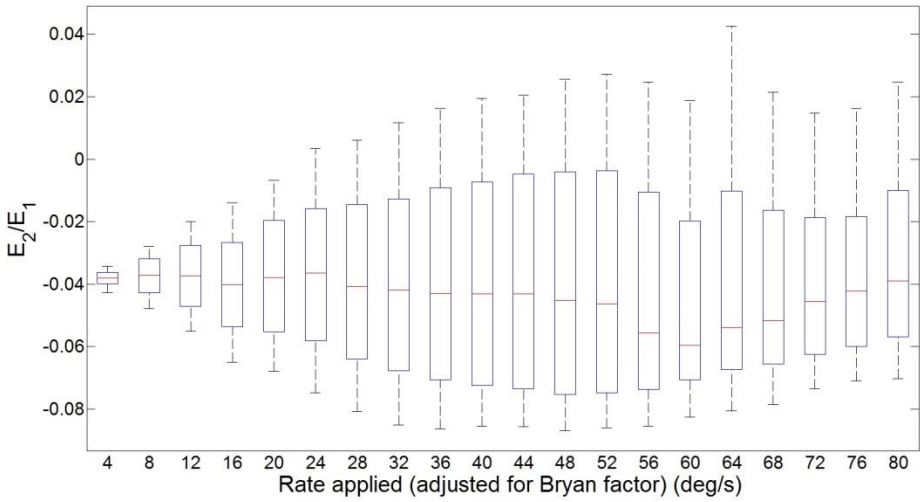

***Figure 7.2 - Box plots of the ratio E_2/E_1* for increasing rate**

It is evident that, in order to use the method discussed in [26], the scale factor for this gyroscope architecture should be measured at rates above 20°s^{-1} only. The output for these tests is the average change in angle measured for each time sample, while the input is the input change in angle per time sample. Where Δt is the length of time sample (in this case 0.1s) and recall the term $\frac{2n}{(n^2+1)}\Omega$ is the input rate multiplied by Bryan factor, the input change in angle used for scale factor calculations is expressed as in equation 7.2.

$$\Delta\varphi_{ideal} = \Delta t\left\{\frac{2n}{(n^2+1)}\Omega\right\} \qquad 7.2$$

The measured output, $\Delta\varphi$, is the average change in angle between each sample for the given experimental run time.

Figure 7.3 provides plots of the input against output angle for both positive and negative rates. Each point on these figures corresponds to the average change in input angle per time period for the sample data for each of the rates tested and can be used to examine the linearity of the gyroscope behaviour. From visual inspection, both appear to follow a broadly linear pattern, although this will be examined more closely when the linearity error is analysed in section 7.2.2.

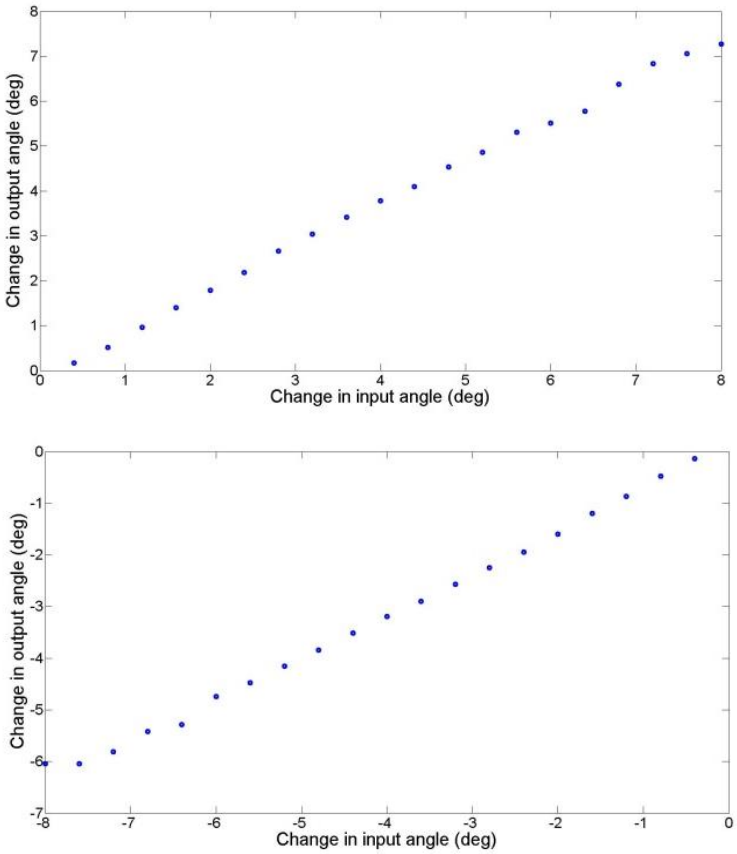

Figure 7.3 - Plots of average input against output angle for a single time period with the application of positive rate (top) and negative rate (bottom)

By fitting lines to these charts using the least squares method, it can be shown that for positive rates the gyroscope has a scale factor of approximately 0.95, whereas for negative rates the scale factor is shown to be approximately 0.81. Although these differ slightly from those indicated by figure 7.1, this can be attributed to the differing calculation method (i.e. the use of all rates to calculate scale factor, as opposed to its calculation for each individual rate). This is a large difference and is explored further during the investigation of asymmetry in section 7.2.3 and its subsequent analysis in section 7.4.

7.2.2. Linearity error

An important measure of gyroscope performance is linearity error (also referred to as scale factor accuracy), and is a measurement of how accurately the measurement of precession reflects a linear rate input. The linearity error is obtained by finding the deviation of the output at each applied rate from the fitted line calculated in section 7.2.1 [26].

Where the data sample consists of *k* rates the linearity of the gyroscope, *L*, can be expressed, as a percentage, by:

$$L = \left(\frac{1}{k}\sum_{i=1}^{k}\frac{\varphi_i - (SF)\hat{\varphi}_i}{(SF)\hat{\varphi}_i}\right)100 \qquad 7.3$$

A lower linearity error is beneficial for gyroscope performance as it represents a response that fits to that dictated by the scale factor.

The gyroscope examined here has a linearity error of 6.93% and 6.04% for positive and negative rates, respectively. Although this appears to be relatively high, these measurements incorporate the low rate behaviour discussed is section 7.2.1. This can be better visualised by figure 7.4 which shows the deviation from the line of best fit for the measurement of each applied rate. The large deviation of the low rate behaviour is clearly evident, with the deviation dropping to a minimum of 0.5% and 0.2% at 28°s^{-1} for positive and negative rates respectively.

It is clear from figure 7.4 that the massive deviation from linearity at low rates is somewhat skewing results. By neglecting those measurements below the 20°s^{-1} limit identified previously, the linearity error of the gyroscope falls to 1.53% and 1.20% for positive and negative rates, respectively. This leads to an average linearity error of 1.37%.

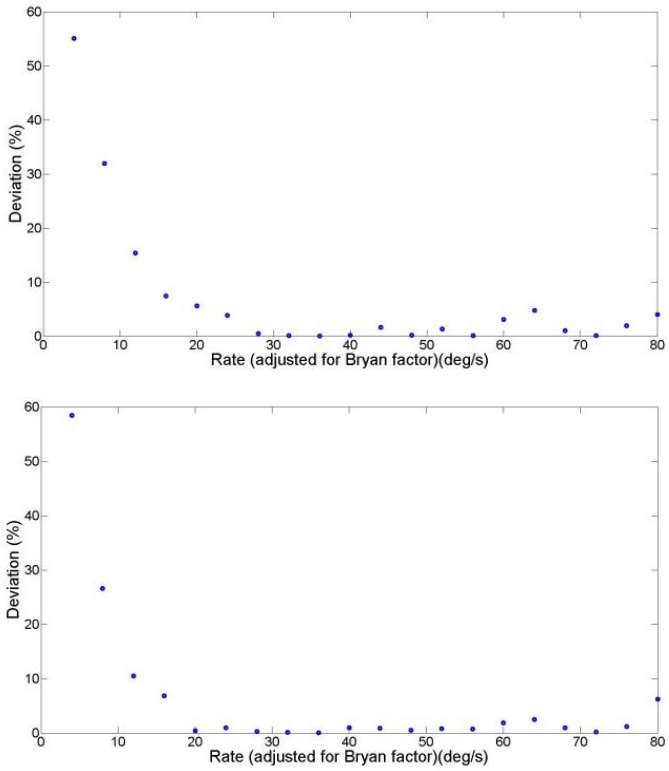

Figure 7.4 - The deviation of the measured angle from the line of best fit for positive (top) and negative (bottom) rate

7.2.3. Asymmetry

The asymmetry of a gyroscope is a measure of how closely the performance of the gyroscope with positive rate applied matches that with negative rate applied. Where SF_P is the scale factor in the positive direction and SF_N the scale factor in the negative direction, the asymmetry, A, for a given rate is defined as [26]:

$$A = \frac{2(SF_P - SF_N)}{(SF_P + SF_N)} \qquad 7.4$$

An asymmetry of zero is perfect, as this indicates no difference between the application of positive and negative rate. It has already been established in section 7.2.1 that this gyroscope exhibits asymmetry, and this can be quantified to be an asymmetry of 0.16, or 16%.

Although this value is very large, it does reduce somewhat when the lower rate results discussed previously are discounted. Having a mean value of 6% for higher rates, this is clearly an improvement on the asymmetry for the whole range of testing. However, it is nevertheless a large number, with values in the region of 100ppm (0.01%) being preferable for high-performance gyroscopes [27].

Asymmetry is commonly caused by slightly mismatched control electrodes [28], although the causes behind it being particularly high for this gyroscope are unclear. It is possible that the structure of the gyroscope exhibits abnormally high imperfections or the implementation of the control scheme has resulted in some mismatch, although there has been little evidence of this during previous experimental work.

7.2.4. Drift measurement

Drift measurements provide information regarding the long-term performance of the gyroscope. The bias drift is measured as the average rate of measured rotation when the gyroscope is stationary and earth rate has been removed, and is obtained by taking an average of the change in precession as a gyroscope is left stationary for a finite period of time.

Where D is the bias drift, it is calculable using:

$$D = \frac{1}{k}\sum_{i=1}^{k} \dot{\varphi}_i - \phi_{earth} \qquad 7.5$$

This is where k is the number of samples, φ_i the angle of precession and ϕ_{earth} is the angular rate of rotation of earth, which is approximately 15°hr^{-1} where the gyroscope was tested.

Figure 7.5 is a sample of output precession measurement data while the gyroscope is held stationary, prior to the removal of earth rate. Although it appears that only a small amount of bias drift is exhibited, when the contribution of earth rate is taken into account, the absolute value of measured drift is approximately 15°hr^{-1}.

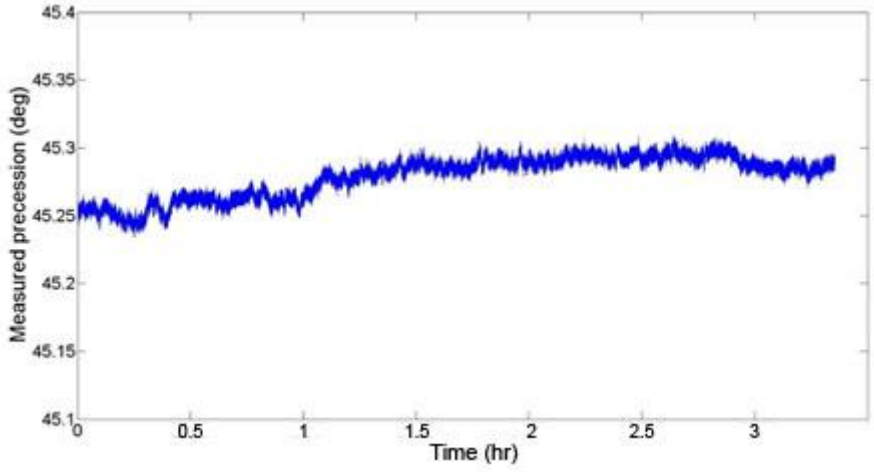

Figure 7.5 - A sample of output precession for a stationary gyroscope prior to the removal of earth rate

Random drift must also be accounted for, and this is done through the use of an Allan variance test, whereby the gyroscope is activated but stationary for a long period of time. The rate data is then divided into several time segments of equal length, and the average variance for these segments taken. This is better expressed by equation 7.6, where *AV* is the Allan variance, *n* is the number of the data segments measured and T is the averaging time.

$$\left(AV(\mathrm{T})\right)^2 = \frac{1}{2(n-1)}\sum_i (\dot{\varphi}(\mathrm{T})_{i+1} - \dot{\varphi}(\mathrm{T})_i)^2 \qquad 7.6$$

This process is repeated for segments of increasing length, allowing the variance to be plotted against sample time on a log scale. This plot gives the angle random walk (a measure of gyroscope noise) as the Allan variance for a sample time of 1s, while the bias instability (the minimum rate at which bias may change over time) is the minimum point on the plot.

Allan deviation is used to measure the performance of a gyroscope over long time scales. The requirements of a gyroscope with respect to Allan deviation vary according to the application. For example, for space navigation operations, where it is viable to average measurement data over a long period, a low bias instability would be desirable. However, for shorter averaging times, such as in video game controllers, a lower angle random walk may be desirable to ensure noise is minimal.

The Allan variance plot for this gyroscope is provided in figure 7.6. This plot shows that the angle random walk has a value of $0.3°hr^{-0.5}$, while the bias stability has a value of $6.55x10^{-4}°s^{-1}$, or $2.36°hr^{-1}$.

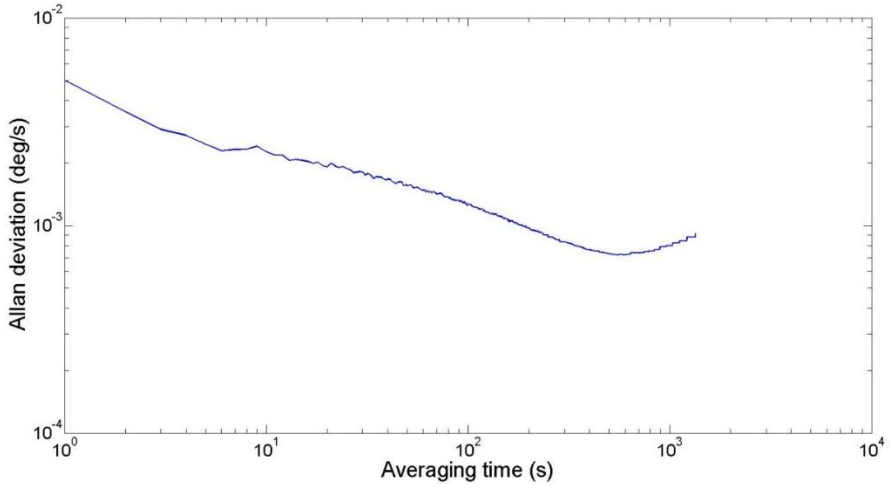

Figure 7.6 - Allan variance plot for the gyroscope

7.3. Bandwidth measurement

The bandwidth test measures the maximum frequency of oscillation the gyroscope can measure – it is a measure of how many measurements the gyroscope can take per second. It is ordinarily conducted by applying a sinusoidal rate to the gyroscope at a set amplitude and measuring the noise of the signal.

However, as discussed in section 6.1 the data transfer rate of the experimental apparatus will severely limit this. Only able to measure 10 data points per second, it is possible to measure the bandwidth up to 10Hz, which, as is demonstrated in section 7.4, is insufficient for a rate integrating gyroscope.

Enhanced bandwidth is one of the major advantages to using a MEMS gyroscope in rate integrating mode and, as such, it is crucial that any characterisation with a view to full implementation of the gyroscope must incorporate bandwidth measurements to validate the use of rate integrating mode. However, this would require extensive redesign of the hardware used in this project and as such is out of its scope.

7.4. Comparison to existing gyroscope specifications

As discussed in section 2.4.1, there are specifications available that divide gyroscopes into three distinct types – ‘rate’, ‘tactical’ and ‘inertial’. These specifications are presented again in table 7.1 and table 2.2.

To demonstrate the effectiveness of the rate integrating gyroscope described in this paper, the specifications in table 7.1 have been compared to the measurements described in section 7.2. It should be noted here that due to the limitations of the rate table described in section 6.1 it has not been possible to measure the full range of the gyroscope or the bandwidth.

	Rate	Tactical	Inertial
Angle random walk (°/√hr)	> 0.5	0.5 - 0.05	< 0.001
Bias drift (°/hr)	11 - 1000	0.1 - 10	< 0.01
Linearity (%)	0.1 - 1	0.01 – 0.1	< 0.001

Table 7.1 - The specifications for the three grades of gyroscope

Parameter	Average
Bias instability (°/hr)	7.5

Table 7.2 - Additional specifications for a rate integrating gyroscope

The measured specifications for the gyroscope used in this thesis are listed in table 7.3.

Parameter	Measurement
Bias instability (°/hr)	2.36
Angle random walk (°/√hr)	0.3
Bias drift (°/hr)	12
Linearity (%)	1.37

Table 7.3 - The measured gyroscope specifications

The measured drift is of a magnitude that puts the gyroscope within the performance parameters normally attributed to higher-end rate gyroscopes, as is shown in table 7.1. A contributing factor to this drift is likely to be the damping asymmetry, which manifests itself as the uneven Q-factors found in section 6.2. As the effect of mistuning is reduced, it will become necessary to account for this in future control schemes as it becomes a significant effect. A control scheme to minimise the effect of damping imperfections can be implemented using methods such as velocity feedback tuning [34].

However, the angle random walk, which is a measure of the random drift exhibited by the gyroscope, is relatively low and places the gyroscope in the realm of tactical grade devices.

This drift performance is further exemplified by the relatively low bias instability, which implies that the variation of bias is lower than that reported in some of the literature. It should, however, be noted that the bias instability measured in the literature varies considerably and, while the gyroscope provides much enhanced performance over many designs, it can be shown to have a considerably lower performance than others. Nevertheless, these results indicate that the random drift has a smaller impact on the gyroscope performance than the bias drift, implying that it may be possible, in future schemes, to reduce the effect of such drift by applying a known tuning voltage.

However, a particularly negative aspect of the gyroscope performance is the linearity. At 1.37%, it falls outside of the required specification for rate gyroscopes, indicating particularly poor performance. This non-linearity is likely to be the result of forces acting upon the precession angle as, although a condition is imposed to set such forcing to zero, there is a minimum forcing that can be applied from the secondary electrode to sustain the second mode of vibration. Should the required forcing drop below this, it is clear that forcing will begin to influence the precession angle.

A solution to this problem is proposed in section 8.1. By implementing further control electrodes it becomes possible to allow further degrees of freedom in the gyroscope control, thus ensuring that the control electrodes are always able to be used such that the applied forcing cannot influence the measurement of precession.

7.5. Test limitations

While the tests conducted have followed the IEEE standards closely, there are nevertheless some shortcomings in the experiment that may be rectifiable following further study on the subject.

The most notable of these were the limitations imposed on the applicable rate. With the data transfer link between the DSP board and data processing laptop severely limiting the frequency of signal input, this should form the primary area of improvement should an oscillating rate table continue to be used for tests. By increasing the frequency of data transfer it becomes possible to apply higher rates due to the potential for increased frequency of oscillation. This will allow the gyroscope to be tested over a much greater range of rates than described previously.

However, another option to resolve this issue would be to use a continuous rate table. By applying rate continuously, as opposed to in an oscillatory manner, a longer sample time is acceptable provided that the applied rate is linear, as there is no direction change resulting from rate table oscillations. This, however, will obviously not resolve the issues with bandwidth testing discussed in section 7.3.

There were also environmental factors that were not addressed during this project. The most notable of this is temperature. It is known that changes in ambient temperature affect the performance of MEMS gyroscopes and it would therefore be informative to include temperature performance tests in any further characterisation.

Chapter 8. Gyroscope re-design

8.1. Additional electrodes

It was demonstrated in section 3.2 that by applying a force along the minor axis of the ellipse in order to adjust the value of the invariant E_2, the effect of mistuning on the measured angle of gyroscope precession can be reduced. However, it has been established in section 6.4.3 that, with the current gyroscope design, the application of this control scheme will cause considerable errors in the measurement of precession angle. Although it is possible to reach a compromise whereby the gyroscope is well-tuned and E_2 is not controlled, with the forcing from the second drive electrode instead being used to null the forcing on the gyroscope precession, it would be preferable to reduce the effect of modal mistuning by controlling E_2. In order to achieve all necessary conditions, however, more drive electrodes are required.

The gyroscope architecture described by figure 8.1 consists of four pairs of drive electrodes four pairs of pick-offs, with the drive electrodes being those placed at equal intervals between 0° and 67.5° (labelled 1 to 4 in the diagram). Such a design permits the excitation of two orthogonal modes of vibration, while generating a quadrature-nulling force that does not influence the precession measurement. The sixteen tuning electrodes have also been retained inside the ring to allow the use of electrostatic correction for providing close initial mode matching.

In this case, the homogenous equations of motion would not differ from those produced by defining equations 3.58 to 3.61 in section 3.2 as unforced. However, the inhomogenous equations of motion would exhibit altered forcing terms, which would take the form of those provided by equations 8.1 to 8.4, where A_n are control gains applied to the drive electrodes n = 1 to 4. These are derived using the same method as that described in section 3.1.2, but by inserting additional electrodes at appropriate angles to the modes and then rearranging in the same manner as for the conventional gyroscope architecture.

$$F_1 = \frac{\hat{\beta}}{\omega_0}\{A_1 \sin\sigma_1 \cos\varphi + A_3 \sin\sigma_3 \sin\varphi + A_2 \sin\sigma_2 (\sin\varphi + \cos\varphi) + A_4 \sin\sigma_4 (\sin\varphi - \cos\varphi)\} \quad 8.1$$

$$F_2 = \frac{\hat{\beta}}{\omega_0}\{A_1 \cos\sigma_1 \sin\varphi - A_3 \cos\sigma_3 \cos\varphi - A_2 \cos\sigma_2 (\cos\varphi - \sin\varphi) - A_4 \cos\sigma_4 (\cos\varphi + \sin\varphi)\} \quad 8.2$$

$$F_3 = \frac{\hat{\beta}}{\omega_0}\{A_1 \sin\sigma_1 \sin\varphi - A_3 \sin\sigma_3 \cos\varphi - A_2 \sin\sigma_2 (\cos\varphi - \sin\varphi) - A_4 \sin\sigma_4 (\cos\varphi + \sin\varphi)\} \quad 8.3$$

$$F_4 = \frac{\hat{\beta}}{\omega_0}\{A_1 \cos\sigma_1 \cos\varphi + A_3 \cos\sigma_3 \sin\varphi + A_2 \cos\sigma_2 (\sin\varphi + \cos\varphi) + A_4 \cos\sigma_4 (\sin\varphi - \cos\varphi)\} \quad 8.4$$

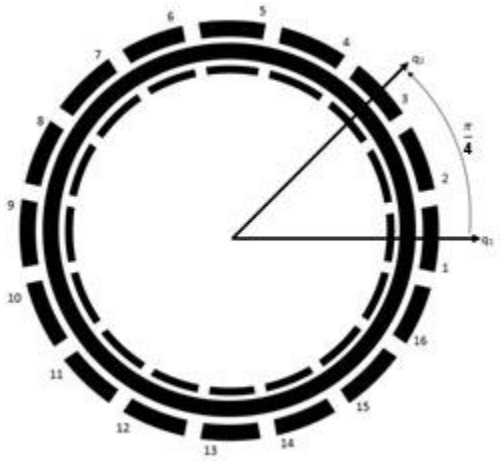

Figure 8.1 - Alternative ring gyro design with four pairs of capacitive drive electrodes (1&9, 2&10, 3&11 and 4&12) and four pairs of sense electrodes (5&13, 6&14, 7&15 and 8&16)

Considering equations 8.1to 8.4, if the gains from electrodes 1 and 3 (and their corresponding drive electrode), A_1 and A_3, are used to excite the two modes of vibration and null quadrature, the gains from the remaining drive electrode pairs, A_2 and A_4, should be used to remove forcing effects from the measurement of angle and orbital phase. By rearranging equations 8.3 and 8.4 to provide $F_3 = 0$ and $F_4 = 0$ (nulling the forcing effects on the precession and orbital phase measurements), it becomes possible to derive the pairs of conditions in equations 8.5 and 8.6 or in equations 8.7 and 8.8. By implementing these, the forcing on the precession and orbital phase can be nulled.

The advantage to this design is that the combination of forcing conditions described previously can be chosen according to which will provide the most effective forcing given the gyroscope's state at the time. For example, as the gyroscope rotates the contribution of the gains A_1 and A_3 to the magnitude of E_1 and E_2 will change as the contributions of these gains to their respective parameters are modulated by the angle φ. By devising a forcing scheme that alternates between the use of electrodes 1 and 3 in controlling the vibration magnitude according to which will permit the greatest range of applied gain, it becomes possible to derive a control scheme that can operate across the widest possible range of conditions and produce the largest response.

It would prove similarly advantageous to switch between electrodes 2 and 4 in controlling the forcing on the ellipse angle or orbital phase, according to which condition would null the contribution of forcing most effectively.

$$A_2 = \frac{A_1 \sin\sigma_1 \sin\varphi - A_3 \sin\sigma_3 \cos\varphi - A_4 \sin\sigma_4 (\cos\varphi + \sin\varphi)}{\sin\sigma_2 (\cos\varphi - \sin\varphi)} \quad 8.5$$

$$A_4 = \frac{A_1 \cos\sigma_1 \cos\varphi + A_3 \cos\sigma_3 \sin\varphi + A_2 \cos\sigma_2 (\sin\varphi + \cos\varphi)}{\cos\sigma_4 (\cos\varphi - \sin\varphi)} \quad 8.6$$

$$A_4 = \frac{A_1 \sin\sigma_1 \sin\varphi - A_3 \sin\sigma_3 \cos\varphi - A_2 \sin\sigma_2 (\cos\varphi - \sin\varphi)}{\sin\sigma_4 (\cos\varphi + \sin\varphi)} \quad 8.7$$

$$A_2 = \frac{-\{A_1 \cos\sigma_1 \cos\varphi + A_3 \cos\sigma_3 \sin\varphi + A_4 \cos\sigma_4 (\sin\varphi - \cos\varphi)\}}{\cos\sigma_2 (\sin\varphi + \cos\varphi)} \quad 8.8$$

8.2. Initial experimental results

8.2.1. Tuning

With the gyroscope design described in section 8.1 having been fabricated, tests have been conducted in order to provide an initial overview of the gyroscope performance.

A further advantage of the design is the sixteen tuning electrodes, half of which are directly aligned with the relevant driven modes of vibration. This design allows the tuning electrodes to alter individual elements of the stiffness matrix, simplifying the tuning process.

Using a process equivalent to that described in section 4.3.1, the tuning electrodes placed between the primary and secondary modes can be used to eliminate the cross-coupling in the

matrix, while those aligned with the driven modes can be used to tune the direct terms. This design therefore allows a greater degree of flexibility in the tuning regime, and this behaviour is demonstrated in figure 8.2. This is a plot of the shift in resonant frequency of each mode from its untuned value as the electrode configurations in table 8.1 are used at their maximum voltage, where direct and cross refer to the electrodes that alter the direct and cross terms in the stiffness matrix – in figure 8.1 the direct tuning electrodes are those directly opposite their corresponding modal sense and drive electrodes (the drive electrodes being electrodes 1, 3, 9 and 11, with their sense electrodes at 90°), while the cross term tuning electrodes are placed between these. It is clear that the direct tuning electrodes affect their corresponding modes considerably more than the other, while the cross terms have effects on both modes.

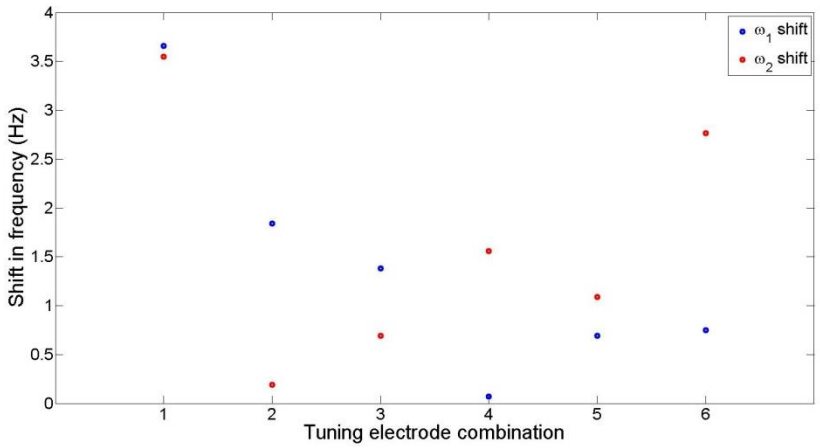

Figure 8.2 - The shift in resonant frequency for each mode as the combination of tuning electrodes used to tune is changed, where the combinations are detailed in table 8.1

Further, it can be noted from figure 8.3 that the minimal modal mistuning of 7.25Hz is achieved where tuning voltages are applied to the second mode and its adjacent cross tuning electrode only. This is a shift of 2.02Hz from the pretuned frequency split of 9.27Hz.

The frequency split remains very large, particularly considering the control scheme derived requires the modes to be tuned to the order of mHz. Figure 8.4 shows that the measured frequency shift of 2.02Hz is of the order expected for the gyroscope architecture provided, and in fact the gyroscope must be provided with enhanced modal tuning before it can be electrostatically tuned. An alternative to this is to use a higher range of tuning voltage, with the same figure demonstrating the enhanced tuning range provided by a higher voltage.

Number	Tuning set
1	All sets
2	Direct primary
3	Cross #1
4	Direct secondary
5	Cross #2
6	Direct secondary and Cross #2

Table 8.1 - The tuning electrode combinations used to produce figure 8.2

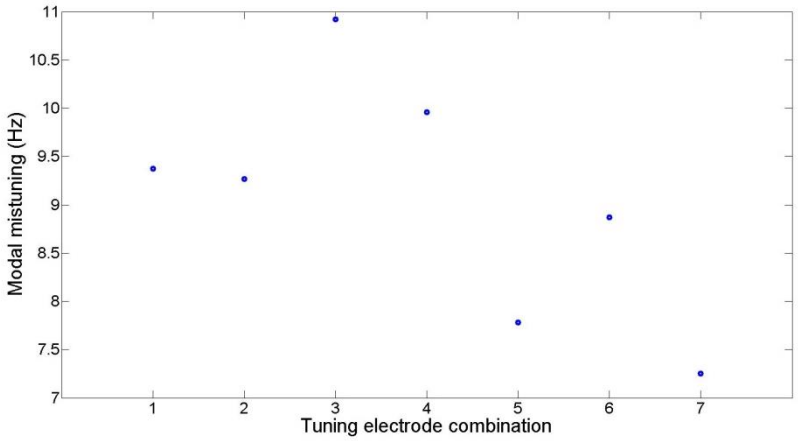

Figure 8.3 - The modal mistuning associated with varying combinations of tuning electrodes

Number	Tuning set
1	All sets
2	No tuning applied
3	Direct primary
4	Cross #1
5	Direct secondary
6	Cross #2
7	Direct secondary and Cross #2

Table 8.2 - The tuning electrode sets used to produce figure 8.3

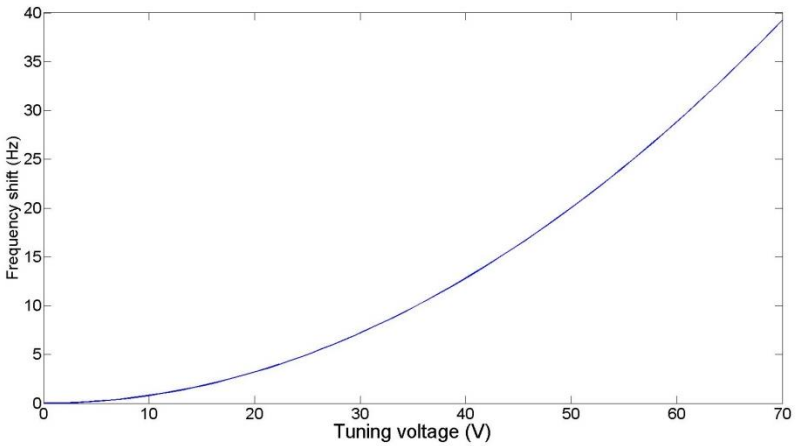

Figure 8.4 - The calculated frequency shift achieved by changing tuning voltage

Figure 8.5 shows that while the modal mistuning is reduced following the application of tuning, the resonant frequency of the second mode of vibration increases following tuning. This is an irregular effect, as it indicates that the tuning electrodes are having a hardening effect. This indicates that structural irregularities are present during the tuning of the gyroscope.

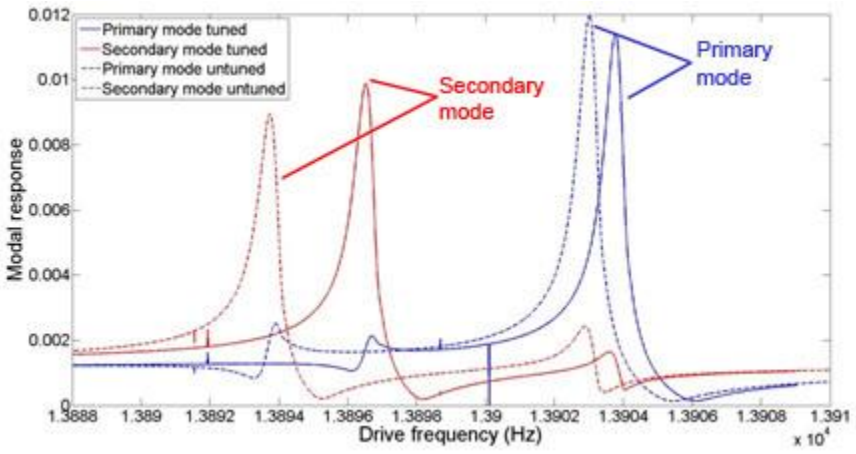

Figure 8.5 - Modal response plots of the tuned gyroscope

8.2.2. Phase locked loop

The plot of orbital phase in figure 8.6 was taken following a frequency sweep, and demonstrates that the orbital phase indicates resonance at approximately equal values for each mode, as denoted by the coloured dots on the trace, labelled A, B and C, which are the second, average and first mode responses, respectively. However, with there being a large frequency split it is clear that the average resonant frequency, ω_0, is located between the two areas of resonant behaviour indicated, where the value of orbital phase at this is indistinguishable from those values further away from average modal resonance. This indicates that, in order for orbital phase to be used to produce a phase locked loop, the modal mistuning must be much smaller than is possible with this new design.

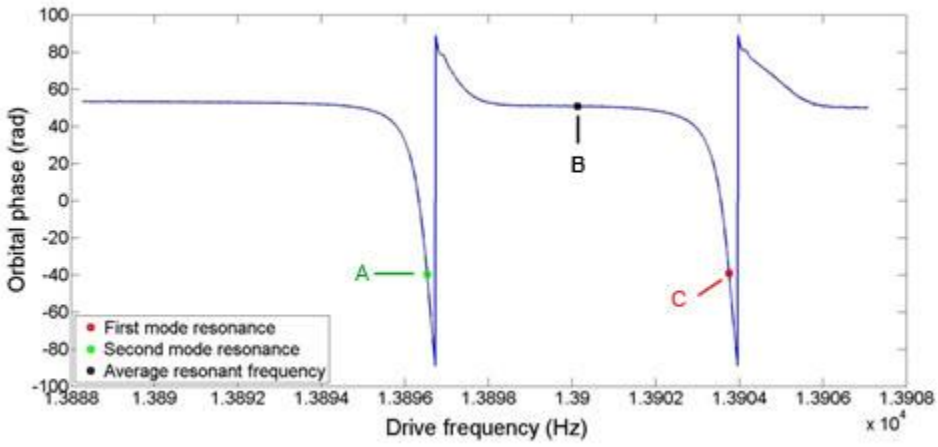

Figure 8.6 - Orbital phase change during a frequency sweep

An alternative to the use of orbital phase is the use of first mode phase, with the value adjusted to shift the drive frequency closer to the average resonant frequency of the two

modes, ω_0. However, the frequency sweeps in figure 8.7 show similar behaviour, whereby the location of the average resonant frequency of the two modes is at an indeterminate location.

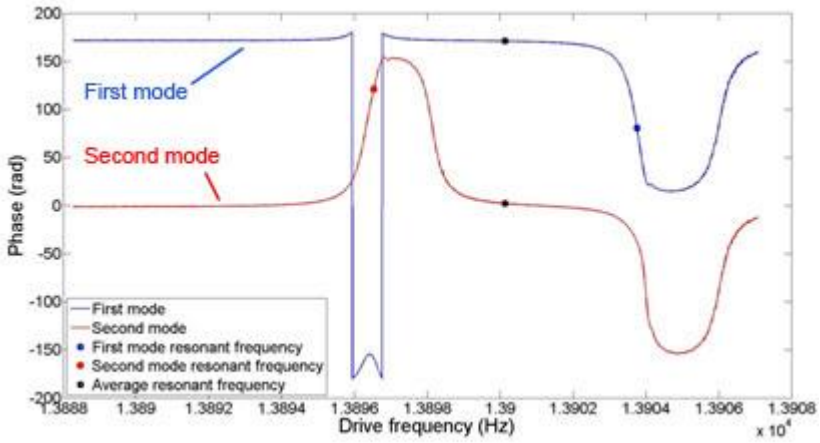

Figure 8.7 - Modal phase plot for both modes of vibration during a frequency sweep

With neither orbital phase or first mode phase being suitable for locking to the average resonant frequency of the two modes of vibration, it is clear that a much smaller degree of modal mistuning must be attained before the control scheme can be implemented as planned.

With the very large modal mistuning, large errors are likely to occur in the system as a result of both the aforementioned modal mistuning and drive mistuning. This is further compounded by the inability to locate the average resonant frequency of the two modes, with the resulting drive frequency likely to be a sizable distance from the optimum. As such, it is unlikely that any experimental results will provide a reliable insight into the performance of the device, or provide a comparison to that of the device described previously.

Chapter 9. Conclusions

9.1. Control scheme effectiveness

A control scheme has been devised for a rate integrating MEMS ring gyroscope that can be shown through simulations to be effective in reducing the effect of modal mistuning upon the accuracy of angle measurement. These simulations show that the potential increase in accuracy is massive, with a 100-fold increase in measurement accuracy being attainable. However, this increase relies on the perfect application of forcing.

It has been shown that the gyroscope geometry used in the project possesses insufficient drive electrodes to apply the control scheme described, as it is not possible to null the effect of control forces upon the measured precession. Furthermore, it is clear that many of the inaccuracies concerning the control scheme, particularly drive mistuning, are very difficult to eliminate, this effect being compounded by the application of rate. Errors also arise as the result of drive electronics, manifesting as a phase shift of the drive signal. However, it has been shown that these can be nulled by carefully choosing the initial drive parameters.

Despite the lack of a fully closed-loop control scheme, the effectiveness of each component has been demonstrated. The phase locked loop and vibration envelope controls have been shown to be effective across a range of rates, although the outputs do suffer some increase in standard deviation as rate increases due to the relationship between ellipse angle and force applied.

Further, a scheme to null any forcing on the measured precession using capacitive forcing from other electrodes has been shown to be effective. Furthermore, characterisation of the gyroscope using this scheme has shown it to have performance similar to that of a rate gyroscope, although the random drift performance appears to be equivalent to that of a tactical-grade gyroscope.

Table 9.1 provides a comparison of the measured performance of the rate integrating gyroscope devised in this thesis to the performance or a standard rate-integrating gyroscope, as discussed in section 7.4.

Parameter	Gyroscope developed in thesis	Standard rate integrating gyroscope
Bias instability (°/hr)	2.36	7.5
Angle random walk (°/$\sqrt{\text{hr}}$)	0.3	0.5-0.05
Bias drift (°/hr)	12	0.1-10
Linearity (%)	1.37	0.01-0.1

Table 9.1 – A comparison of the measured performance of the gyroscope to the performance of a standard commercially-available rate integrating gyroscope

Although the immediate indication of these results is that the gyroscope does not meet the standard of a rate-integrating gyroscope, as originally intended, they do demonstrate that the scheme described can be used to measure angle with some accuracy. More importantly, they indicate the changes required to ensure that the gyroscope can measure with the accuracy expected from a modern rate-integrating gyroscope.

Furthermore, the adaptability of the rate gyroscope design in figure 1.1 has been demonstrated, with the mode of operation being changed exclusively through the careful adjustment of the control program and re-purposing of the drive and pick-off electrodes. However, it has also been clearly demonstrated that for a fully-effective rate-integrating gyroscope a greater number of degrees of freedom are required in the control architecture than are available with that used for the bulk of this project.

9.2. Gyroscope re-design

It is clear from section 8.2 that the behaviour of the optimum gyroscope is similar to that of the current gyroscope, particularly with regards to tuning. Most notably, the tuning electrode arrangement allows the direct and cross terms of the stiffness matrix to be modified independently.

Despite the success in the design of the tuning electrode arrangements, it is clear that the construction of the gyroscope is not to a sufficient standard for the implementation of a rate-integrating control scheme. Solutions to this would be to either physically tune the gyroscope through methods such as laser ablation, or to use a larger power supply to provide enhanced

tuning voltages. Neither of these solutions are possible given the timeframe for the project, however, and therefore simply provide directions for any future research.

Furthermore, it would be useful to examine whether this design has any advantages over the use of a parametric drive.

9.3. Further work

With the work in this thesis laying the foundations for the creation of a control scheme featuring all of the control loops previously discussed, the logical progression is to implement these on the proposed gyroscope architectures. It would also be useful to investigate the application of the automatic tuning loop discussed in section 4.3.2.

By implementing a control scheme that features all control loops discussed and comparing the accuracy of the gyroscope architectures used to the results detailed in chapter 7, it should be possible to demonstrate an increase in accuracy over the current gyroscope architecture being used in rate integrating mode. As part of this, it would be prudent to compare the accuracy improvements obtained using parametric drive to those using capacitive.

However, further study of the existing gyroscope architecture may also be necessary. In particular, it is important to observe higher rate behaviour than that detailed in this thesis in order to better reflect the likely operating parameters. The effect of environmental conditions must also be considered.

9.3.1. Parametric Drive

An alternative to the use of additional drive electrodes described in section 8.1 is to use parametric drive. Such a drive excites the gyroscope with a drive frequency twice that of the ring's resonant frequency, applied in a way such as to not influence the measurement of precession. Parametric excitation has the advantage that is excites the gyroscope into resonance without affecting the modes of vibration. Conventional capacitive control forces can then be used to reduce the effect of imperfections as described previously.

An example of a gyroscope design that permits parametric excitation is the use of an annular electrode to provide excitation, as shown in figure 9.1. However, there are a number of electrode layouts that may permit such a scheme, and the appropriate type is an avenue for future research in the area.

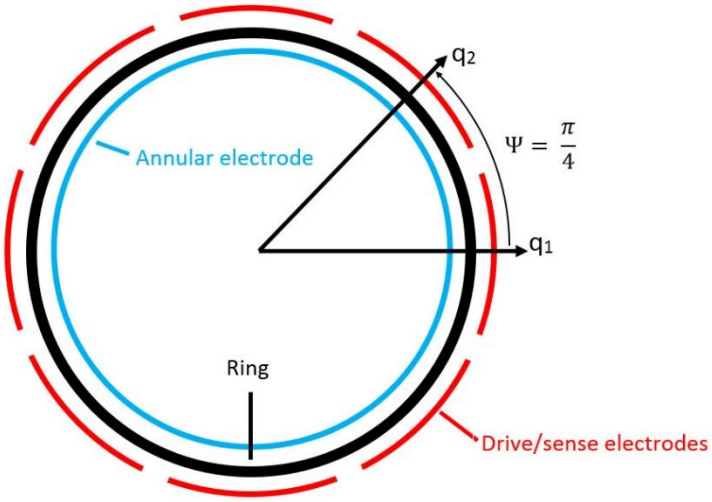

Figure 9.1 - An example of a gyroscope architecture for the provision of parametric drive, where this is provided through the blue annular ring

Parametric drive applies forcing through the stiffness matrix, thus does not affect the gyroscope precession. This alters the equations of motion, providing parametric terms in the stiffness matrix. The careful choice of such components allows an excitation to be applied that does not influence the angle of precession of the gyroscope's vibratory pattern.

This design has the advantage that is simpler and does not require forcing components for the control system that are much more complicated than those described previously in this thesis. However, the addition of parametric terms can have the potential to complicate the gyroscope dynamics if not chosen appropriately.

Chapter 10. Appendices

10.1. Published work

The following is a list of publications that are fully or in part derived from the research detailed in this thesis:

- Bowles, S.R. et al, *Control Scheme to Reduce the Effect of Stiffness Imperfections in a Rate Integrating MEMS Gyroscope*, IEEE Sensors, 2015. **15**(1): p. 552-560.
- Bowles, S.R. et al, *Control scheme for a rate integrating MEMS gyroscope*, Inertial Sensors and Systems (ISISS), 2014 International Symposium on, 2014, Laguna Beach: p. 1-4
- Hu, Z.X. et al, *A systematic approach for precision electrostatic mode tuning of a MEMS gyroscope*, J. Micromech. Microeng., 2014. **24**(12)

10.2. Programs

The program used to control the gyroscope is provided. Only the primary C and assembly routines are provided, as many of the routines used to process signals are generic programs that provide little interest to the reader.

10.2.1. Initial gyroscope design – C routine

```
// NAME:     main.c (sample-based Talkthrough)
// PURPOSE:  Function main() for AD1939/ADSP-21469 Talkthrough
framework


#include "ADDS_21469_EzKit.h"
#include "stdio.h"
#include "signal.h"
#include <math.h>
#include "processor_include.h"
#include <def21469.h>

#include <string.h>

float * DelayLine;

int Index  = 0;
int Sine_Index = 0;
int SPORT1_isr_count = 0;
int SPORT0_isr_count = 0;

int timer_count=0, timer_c1=0, timer_c2 =0;
```

```
float fre = 1216675*16;    //1216931, frequency PLL start at this
float reso_f, f_resolution = 0.011718;
float f_mult = 16;
float f_lowlimit = 1216650, f_uplimit = 1217000;

float FlagScan =1;

void useUART(void);
void SPORT1_isr_counter(void);
void SPORT0_isr_counter(void);
void timer_isr (int sig);

void FillBuffer(int Num);

extern ftoa(float f);
extern char outbuf_sign, outbuf_int[6], outbuf_frac[6];

char source[164];

//PID parameters and related variables
float er, er_1 =0, er_2 =0;
float er2, er2_1 = 0, er2_2 = 0;
float per, per_1=0, per_2=0;

float de_fm_gain = 5; //desired first mode gain

extern float    buffer_a[75];         /*store sampled drive siganl*/
extern     float      buffer_q[75];         /*quadrature drive signal
from Hilbert transform*/
extern float    buffer_r[75];         /*store sampled response
signal*/
extern float    buffer_m2[75];        /*second mode signal*/
extern float    buffer_ar[75];
extern float    buffer_qr[75];

extern float    digi_2f_a, digi_2f_q;
extern float    current_digi_a, current_digi_q;
extern float    aligned_digi_a, aligned_digi_q;       //aligned with
the actual drive signal

extern float    current_a, current_q, current_r, current_m2;
extern float    current_oa, current_qa;
extern float    current_ar, current_qr, current_am, current_qm,
current_rm;          //low pass filtered cross products
extern float    current_shifted_rm;
extern int           Extend1_M_reg, Extend2_M_reg, Extend3_M_reg,
Extend4_M_reg;
extern float    Gain_1f, Gain_1s, Gain_2f;
extern int      Extend1D_I_reg, Extend2D_I_reg;
extern float    square_drive, square_response_f, square_response_s;
extern float    de_response_f;
extern int           Start_control, Param_control, fb_enable;
extern int           Start_comm;

extern float    amp_orthogonal;
extern float    amp_drive;
```

```
extern float    amp_response_f, amp_response_f_pr;
extern float    amp_response_s;
extern float    amp_response_s_inphase, amp_response_s_quadrature;
extern float    amp_cross_df;
extern float    cos_phase, cos_angle, cos_rm;
extern float    Phase_resultant_drive;
extern float    delta;
extern float    Gain_DirectTerm, Gain_CrossTerm, Gain_feedback;
extern char     Flag_AMtuning, Flag_AGC, Flag_PLL;

float de_phase = 90;
float cos_phase_pr =0, cos_rm_pr =0, amp_response_s_inphase_pr,
amp_response_s_quadrature_pr;
float cos_phase_pr2 =0, cos_rm_pr2 =0;

float beta =0.62167;                    //coefficient of allpass phase
shift, changes with signal freq and desired phase shift
float man_phase = 0, des_phase ; //90; //desired phase shift value,
for the known resonant frequency
float beta_90 = 0.62167;                //coefficient for a 90 degrees
shifter
float beta_2f;

float Angle_drive, Angle_fr, Angle_sr;
float Angle_DfRf=0, Angle_DfRs=0, Angle_RfRs =0; //angle Rf relative
to Rs
float Primary_angle_err, Primary_angle_errp =0, Primary_angle_errp2
=0;
float Secondary_angle_err, Secondary_angle_errp =0,
Secondary_angle_errp2 =0;


float Gain_Sec_2f = 0.1;
float Gain_Force_Rebalance = 0;
float fb_control_i =0, fb_control_q =0;

float f_norm;
float f1_max = 0.6;         //600mv max applied gain
float f1_min = 0.008;       //8mv min applied gain
float fm_gain, tp;          //first mode response gain

float Scale = 1.4285;
float I_2f, Q_2f;

//variables for electrostatic tuning
char  flag_tuningdata =1;

float ESB_P = 128, ESB_S = 128;                    //start from half
float ESB_P_Ratio =0.5, ESB_S_Ratio =0.50;  //0.5 ~ 1.5

float DC_bias = 255, dif_PCW, dif_PACW, dif_SCW, dif_SACW;
float A_1, B_1, A_2, B_2;
char SCW0, PACW1, PCW2, SACW3;                     //electrostatic
tuning voltages

//invariables and eliptic parameters
```

```
float Ee, Qq, Rr, Ss, Lr, Li;
float Prec_angle, Orbit_phase, Major_amp, Minor_amp, Diff;
float n = 0;
float Orbit_phase_mod;
float Ti = 0;
float F1, F3;
float limit = 2.5;
float A_1_in, A_2_in, B_1_in, B_2_in;
float p = 0;

void main()
{

      initPLL();
      initDDR2DRAM();

    // Initialize DAI because the SPORT and SPI signals
    // which need to be routed
    InitDAI();

    // This function will configure the AD1939 codec on the 21469
EZ-KIT
    Init1939viaSPI();

    useUART();

    // Turn on SPORT0 TX and SPORT1 RX for Multichannel Operation
      enable_SPORT01_MCM_mode();
      enable_SPORT01_DMA_channels();

      SinTableInit();
      BufferInit();

      // Unmask SPORT1 RX ISR Interrupt
      interrupts(SIG_SP1, process_AD1939_samples);
      //SIG_SP1

      // SIG_TMZ0 enables high priority timer interrupt, SIG_TMZ for
low priority
      interrupt(SIG_TMZ, timer_isr);

    timer_set(1000000, 1000000);      // set tperiod and tcount of
the timer(in cycles)
    timer_on();

      // Set up small delay buffer
      DelayLine = (float *) 0x000C4000;

      // read electrostatic tuning voltages from EEPROM,
      DPeeprom_read();

      // calcualte voltage difference between DC bias and tuning
voltages
      dif_PCW  = 255 - PCW2;
      dif_PACW = 255 - PACW1;
      dif_SCW  = 255 - SCW0;
```

```
      dif_SACW = 255 - SACW3;

      // calcualte initial A1 A2..., B1 B2 can be negative
      A_1 = dif_PCW*dif_PCW + dif_PACW*dif_PACW;
      B_1 = dif_PCW*dif_PCW - dif_PACW*dif_PACW;
      A_2 = dif_SCW*dif_SCW + dif_SACW*dif_SACW;
      B_2 = dif_SCW*dif_SCW - dif_SACW*dif_SACW;

      A_1_in = A_1;
      A_2_in = A_2;
      B_1_in = B_1;
      B_2_in = B_2;

      // TuningVoltageUpdate();
      Update_wiper_RAM_EEPROM();

      for (;;)
        {

      //send measurements via UART0 DMA every 100ms
      if(timer_count > 100*0.45 && Start_comm ==1)
                {

                timer_count =0;

                if(flag_tuningdata ==1)
                      {
                      flag_tuningdata =0;         //send once when
one of them is changed

                      ftoa(0);
                      FillBuffer(0);

                      ftoa(Gain_DirectTerm);
                      FillBuffer(1);

                      ftoa(Gain_CrossTerm);
                      FillBuffer(2);

                      ftoa(B_1);
                      FillBuffer(3);

                      ftoa(B_2);
                FillBuffer(4);

                      ftoa(A_1);
                      FillBuffer(5);

                      ftoa(A_2);
                      FillBuffer(6);

                      source[162] = 0x0a;
                      source[163] = 0x0d;

                      *pUART0TXCTL =0;
                *pIIUART0TX = (unsigned int) &source[0];
```

```
*pIMUART0TX = 1;
*pCUART0TX = 164;          //86, sizeof(source);
*pUART0TXCTL = UARTEN | UARTDEN;
     }

else
     {

     ftoa(reso_f);               //drive frequency
     FillBuffer(0);

     ftoa(Ee*1000);
     //ftoa(A_1);
     FillBuffer(1);

     ftoa(Qq*1000);
     //ftoa(B_1);
     FillBuffer(2);

     ftoa(Gain_1f);
     //ftoa(n);
     FillBuffer(3);

     if(fb_enable != 0)
          ftoa(fb_control_i);
     else
          ftoa(amp_response_s_inphase*Scale);

     ftoa(Gain_1s);
     FillBuffer(4);

     ftoa(Angle_drive);
     FillBuffer(5);

     ftoa(Orbit_phase_mod);
     FillBuffer(6);

     ftoa(current_ar);
     FillBuffer(7);

     ftoa(current_qr);
     FillBuffer(8);

     ftoa(current_am);
     FillBuffer(9);

     ftoa(current_qm);
     FillBuffer(10);

     if(Flag_AMtuning == 1) n++;

     source[162] = 0x0a;
     source[163] = 0x0d;

     *pUART0TXCTL =0;
*pIIUART0TX = (unsigned int) &source[0];
```

```
                *pIMUART0TX = 1;
                *pCUART0TX = 164;          //86, sizeof(source);
                *pUART0TXCTL = UARTEN | UARTDEN;
                      }

                }

       }
}

void FillBuffer(int num)
{
      int i, k;

      k=14*num;
      source[k] = outbuf_sign;
      for (i=1; i<7; i++) source[k+i]=outbuf_int[6-i];
      for (i=7; i<13; i++) source[k+i]=outbuf_frac[12-i];
      source[k+13] = 0x20;
}

//this interrupt takes about 50 cycles overhead to call in and //50
cycles to call out,
//therefore, Tperiod can not be too low,
void timer_isr (int sig)
{
 int i, value;
 float AM_radian, pi = 3.14159;

 float fblimit_l = -0.06, fblimit_h = 0.06;
 float ctemp =0;

 //PID control variables for the primary electrode
 float Kp = 1;
 float Ki = 0.1;
 float Kd = 0.1;

//PID control variables for the secondary electrode
 float Kp2 = 6;
 float Ki2 = 0.01;
 float Kd2 = 0.01;

 timer_count++;
 timer_c1++;

 timer_c2++;
 AM_radian = 2*pi*timer_c2/5000.0; //varies from 0 ~ 2pi
 if(timer_c2 >= 5000) timer_c2 =0;

 //----------measure all necessary elements before closing control
loops-------------
 //amp_orthogonal is always unit, better calcualte square of inphase
and quadrature
 //in CODEC interrupt, in case use diffrent values due to higher
priority.
```

```
amp_orthogonal = sqrtf(current_digi_a * current_digi_a +
current_digi_q * current_digi_q);
amp_drive = 2*sqrtf(square_drive)/amp_orthogonal;
amp_response_f = 2*sqrtf(square_response_f)/amp_orthogonal;
amp_response_s = 2*sqrtf(square_response_s)/amp_orthogonal;

 // phase angles relative to internal reference
     Angle_drive = atan2f(current_qa, current_oa)*57.2958;
     Angle_fr = atan2f(current_qr, current_ar)*57.2958;
     Angle_sr = atan2f(current_qm, current_am)*57.2958;

 //  Phases relative to real primary drive, avoid electronics //and
processing phase shifts
Angle_DfRf = Angle_fr - Angle_drive;  //First mode phase wrt drive

     if(Angle_DfRf > 180)
          Angle_DfRf = Angle_DfRf - 360;
     if(Angle_DfRf < -180)
          Angle_DfRf = Angle_DfRf + 360;

Angle_DfRs = Angle_sr - Angle_drive; //Second mode phase wrt drive

     if(Angle_DfRs > 180)
          Angle_DfRs = Angle_DfRs - 360;
     if(Angle_DfRs < -180)
          Angle_DfRs = Angle_DfRs + 360;

Angle_RfRs = Angle_fr - Angle_sr; //Difference between primary and
secondary phase
     if(Angle_RfRs > 180)
          Angle_RfRs = Angle_RfRs - 360;
     if(Angle_RfRs < -180)
          Angle_RfRs = Angle_RfRs + 360;

//Calculation of invariants
Ee = current_ar * current_ar + current_qr * current_qr + current_am
* current_am + current_qm * current_qm;
Qq = 2*(current_ar * current_qm - current_am * current_qr);
Rr = current_ar * current_ar + current_qr * current_qr - current_am
* current_am - current_qm * current_qm;
Ss = 2 * (current_ar * current_am +  current_qr * current_qm );
Lr = current_ar * current_ar - current_qr * current_qr + current_am
* current_am - current_qm * current_qm;
Li = 2*(current_ar * current_qr + current_am * current_qm);

Prec_angle = 0.5* atan2f(Ss, Rr) * 57.2958;
Orbit_phase = 0.5 * atan2f(Li, Lr) * 57.2958;
Orbit_phase_mod = Orbit_phase;
     if(Orbit_phase_mod < 0) Orbit_phase_mod = Orbit_phase_mod +
180;

 // calculate drive frequency from index register Extend1_M_reg:
reso_f = Extend1_M_reg * f_resolution/f_mult;

Extend1_M_reg = (int)fre;
```

```
     if(Extend1_M_reg > f_uplimit*f_mult) Extend1_M_reg =
f_uplimit*f_mult;
     if(Extend1_M_reg < f_lowlimit*f_mult) Extend1_M_reg =
f_lowlimit*f_mult;
     Extend2_M_reg = Extend1_M_reg;
     Extend3_M_reg = Extend1_M_reg << 1; //2f signal, for parametric
application
     Extend4_M_reg = Extend1_M_reg << 1;

//  Calculate phase error for Phase lock loop. Due to JFET //buffer
inside the device, 90 ahead of drive, the real //vibration phase is
90 behind.

Primary_angle_err = (83.7 - Orbit_phase_mod);

//Primary mode PLL
     if(Flag_PLL == 1 && timer_c1 >= 2)
       {
          timer_c1 = 0;
fre += -50.0*(Primary_angle_err - Primary_angle_errp) -
10*Primary_angle_err - 0.2*(Primary_angle_err -2*Primary_angle_errp
+ Primary_angle_errp2);

          //make sure there is drive if not in AGC mode
          if(Flag_AGC != 1 && Flag_AMtuning !=1)
          {
               Gain_1f = 0.25;
               Gain_1s = 0.25;
          }
       }

     //Error in size of E1 and E2
     er = limit - 1000*Ee;
     er2 = 0 - 1000*Qq;

  // AGC for primary mode and secondary mode or angle forcing
//control
     if(Flag_AGC == 1)
     {

          Gain_1f += Kp*(er-er_1) + Ki*er + Kd*(er- 2*er_1 + er_2);

          if(Gain_1f > f1_max) Gain_1f = f1_max;
          if(Gain_1f < f1_min) Gain_1f = f1_min;

          //E2 control
          //Gain_1s += Kp2*(er2-er2_1) + Ki2*er2 + Kd2*(er2-
2*er2_1 + er2_2);

          //Angle forcing control
          Gain_1s = Gain_1f*(tan(Prec_angle/57.2958));

          if(Gain_1s > f1_max) Gain_1s = f1_max;
          if(Gain_1s < f1_min) Gain_1s = f1_min;
          }
```

```
  // Frequency sweep routine
     if(Flag_AGC != 1 && Flag_AMtuning == 1 && Flag_PLL != 1)
     {

           Gain_1f = 0.25;
           Gain_1s = 0.25;

           Extend1_M_reg = f_lowlimit*f_mult + (n*f_mult*(f_uplimit
- f_lowlimit))/5000;

           if(Extend1_M_reg > f_uplimit*f_mult)
           {
                n = 0;
           }

     }

  // always update phase and amplitude errors after PLL and AGC
  //control calcualtions
     er_2 = er_1;
     er_1 = er;

     er2_2 = er2_1;
     er2_1 = er2;

     cos_phase_pr2 = cos_phase_pr;
     cos_phase_pr = cos_phase;
     cos_rm_pr2 = cos_rm_pr;
     cos_rm_pr = cos_rm;

     Primary_angle_errp2 = Primary_angle_errp;
     Primary_angle_errp = Primary_angle_err;
     Secondary_angle_errp2 = Secondary_angle_errp;
     Secondary_angle_errp = Secondary_angle_err;

     amp_response_s_inphase_pr = amp_response_s_inphase;
     amp_response_s_quadrature_pr = amp_response_s_quadrature;

     amp_response_f_pr = amp_response_f;
}
```

10.2.2. Initial gyroscope design – assembly routine

```
/*****************************************************************
*********************************
/
/
/                            AD1939 - SPORT1 RX INTERRUPT SERVICE
ROUTINE                              /
/
/
/    Receives input data from the AD1939 ADCs via SPORT1 and
transmits processed audio data         /
```

```
/    back out to the four AD1939 Stereo DACs/Line Outputs through
SPORT0.                              /
/
/
************************************************************************
**********************************
/
/
/   This Serial Port 1 Receive Interrupt Service Routine performs
arithmetic computations on           /
/   the SPORT1 receive DMA buffer (rx1a_buf) and places results to
SPORT0 transmit                      /
/   DMA buffer (tx0a_buf)
/
/
/
/  rx1a_buf[8] - DSP SPORT receive buffer - AD1939
/
/  Slot # Description                                DSP Data Memory
Address                              /
/  ------ ---------------------------------------  ------------------
--------------------------------  /
/  0      Internal ADC 0 Left Channel               DM(_rx1a_buf + 0)
= DM(_rx1a_buf + Internal_ADC_L1) /
/  1      Internal ADC 0 Right Channel              DM(_rx1a_buf + 1)
= DM(_rx1a_buf + Internal_ADC_R1) /
/  2      Internal ADC 1 Left Channel               DM(_rx1a_buf + 2)
= DM(_rx1a_buf + Internal_ADC_L2) /
/  3      Internal ADC 1 Right Channel              DM(_rx1a_buf + 3)
= DM(_rx1a_buf + Internal_ADC_R2) /
/  4      External Auxilliary ADC 1 Left Chan.      DM(_rx1a_buf + 4)
= DM(_rx1a_buf + AUX_DAC_L1)      /
/  5      External Auxilliary ADC 1 Right Chan.     DM(_rx1a_buf + 5)
= DM(_rx1a_buf + AUX_DAC_R1)      /
/  6      External Auxilliary ADC 2 Left Chan.      DM(_rx1a_buf + 6)
= DM(_rx1a_buf + AUX_DAC_L2)      /
/  7      External Auxilliary ADC 2 Right Chan.     DM(_rx1a_buf + 7)
= DM(_rx1a_buf + AUX_DAC_R2)      /
/
/
/  tx0a_buf[8] - DSP SPORT transmit buffer - AD1939
/
/  Slot # Description                                DSP Data Memory
Address                              /
/  ------ ---------------------------------------  ------------------
--------------------------------  /
/  0      Internal DAC 1 Left Channel               DM(_tx0a_buf + 0)
= DM(_tx0a_buf + Internal_DAC_L1) /
/  1      Internal DAC 1 Right Channel              DM(_tx0a_buf + 1)
= DM(_tx0a_buf + Internal_DAC_R1) /
/  2      Internal DAC 2 Left Channel               DM(_tx0a_buf + 2)
= DM(_tx0a_buf + Internal_DAC_L2) /
/  3      Internal DAC 2 Right Channel              DM(_tx0a_buf + 3)
= DM(_tx0a_buf + Internal_DAC_R2) /
/  4      Internal DAC 3 Left Channel               DM(_tx0a_buf + 4)
= DM(_tx0a_buf + Internal_DAC_L3) /
```

```
/  5      Internal DAC 3 Right Channel            DM(_tx0a_buf + 5)
= DM(_tx0a_buf + Internal_DAC_R3) /
/  6      Internal DAC 4 Left Channel             DM(_tx0a_buf + 6)
= DM(_tx0a_buf + Internal_DAC_L4) /
/  7      Internal DAC 4 Right Channel            DM(_tx0a_buf + 7)
= DM(_tx0a_buf + Internal_DAC_R4) /
/
/
************************************************************************
*********************************/

#include "adds_21469_ezkit.h"
#include <asm_sprt.h>
#include <def21469.h>
/*  The following macro def should be uncommented to test the DACs
only with some generated pure tones... */
/*  Running at 96 KHz vs 48 KHz, you should hear a 1-octave
difference in the tones */
/*  Tones are generated a 4K sine wave lookup table (integer divisor
of 48K/96K/192K */

#define GENERATE_DAC_PURE_TONES_TEST

.section /dm seg_dmda;

/* AD1939 stereo-channel data holders - used for DSP processing of
audio data received from codec */
// input channels
.var             _Left_Channel_In1;          /* Input values from the
AD1939 internal stereo ADCs */
.var             _Right_Channel_In1;
.var             _Left_Channel_In2;
.var             _Right_Channel_In2;

//output channels
.var             _Left_Channel_Out1;         /* Output values for the
4 AD1939 internal stereo DACs */
.var             _Left_Channel_Out2;
.var             _Left_Channel_Out3;
.var             _Left_Channel_Out4;
.var             _Right_Channel_Out1;
.var             _Right_Channel_Out2;
.var             _Right_Channel_Out3;
.var             _Right_Channel_Out4;

.var             _Left_Channel;              /* Can use these
variables as intermediate results to next filtering stage */
.var            _Right_Channel;

.var             AD1939_audio_frame_timer;

.var             sine4000[4000] = "sinetbl.dat";
.var             TEMP_M5, TEMP_M1, TEMP_M2, TEMP_L5, TEMP_I6;
.var             Sine1_B_reg, Sine1_I_reg, Sine1_M_reg, Sine1_L_reg;
.var             Sine2_B_reg, Sine2_I_reg, Sine2_M_reg, Sine2_L_reg;
.var             Sine3_B_reg, Sine3_I_reg, Sine3_M_reg, Sine3_L_reg;
```

```
.var            Sine4_B_reg, Sine4_I_reg, Sine4_M_reg, Sine4_L_reg;

//need to create three sine waves, for the drive, quadrature of the
drive,
//and 2f drive for parametric amp!
.var            Extend1_B_reg, Extend1_I_reg, Extend1_L_reg;
.var            Extend2_B_reg, Extend2_I_reg, Extend2_L_reg;
.var            Extend3_B_reg, Extend3_I_reg, Extend3_L_reg;
.var            Extend4_B_reg, Extend4_I_reg, Extend4_L_reg;
.extern              _Extend1_M_reg, _Extend2_M_reg,
_Extend3_M_reg, _Extend4_M_reg;
.extern              _Extend1D_I_reg, _Extend2D_I_reg;
.extern              _Gain_1f, _Gain_1s, _Gain_2f, _Gain_Sec_2f,
_Gain_Force_Rebalance;

//regard the six buffers (_buffer_a, buffer_q ...) as circular
buffers,
//define six variables as pointers associated with the
current(header) position, when read in
//data (store), pointers always increase.
.var            digiaBuffer_B_Reg, digiaBuffer_I_Reg,
digiaBuffer_M_Reg, digiaBuffer_L_Reg;
.var            digiqBuffer_B_Reg, digiqBuffer_I_Reg,
digiqBuffer_M_Reg, digiqBuffer_L_Reg;
.var            oaBuffer_B_Reg, oaBuffer_I_Reg, oaBuffer_M_Reg,
oaBuffer_L_Reg;
.var            qaBuffer_B_Reg, qaBuffer_I_Reg, qaBuffer_M_Reg,
qaBuffer_L_Reg;

.var            aBuffer_B_Reg, aBuffer_I_Reg, aBuffer_M_Reg,
aBuffer_L_Reg;
.var            qBuffer_B_Reg, qBuffer_I_Reg, qBuffer_M_Reg,
qBuffer_L_Reg;
.var            rBuffer_B_Reg, rBuffer_I_Reg, rBuffer_M_Reg,
rBuffer_L_Reg;
.var            rBuffer_shifted_rm_B_Reg, rBuffer_shifted_rm_I_Reg,
rBuffer_shifted_rm_L_Reg, rBuffer_shifted_rm_M_Reg;

.var            m2Buffer_B_Reg, m2Buffer_I_Reg, m2Buffer_M_Reg,
m2Buffer_L_Reg;
.var            arBuffer_B_Reg, arBuffer_I_Reg, arBuffer_M_Reg,
arBuffer_L_Reg;
.var            qrBuffer_B_Reg, qrBuffer_I_Reg, qrBuffer_M_Reg,
qrBuffer_L_Reg;
.var            amBuffer_B_Reg, amBuffer_I_Reg, amBuffer_M_Reg,
amBuffer_L_Reg;
.var            qmBuffer_B_Reg, qmBuffer_I_Reg, qmBuffer_M_Reg,
qmBuffer_L_Reg;
.var            rmBuffer_B_Reg, rmBuffer_I_Reg, rmBuffer_M_Reg,
rmBuffer_L_Reg;
.var            zero =0;

.var            Original_2f, previous_Original_2f,
shifted_Original_2f, previous_shifted_Orginal_2f;
.var            shifted_2f, previous_shifted_2f;
.var            Parametric_drive;
```

```
//these variables store the current values, already in float format.
.extern    _I_2f, _Q_2f;
.extern          _digi_2f_a, _digi_2f_q;
.extern          _current_digi_a, _current_digi_q;
.extern    _aligned_digi_a, _aligned_digi_q;
.extern               _current_a, _current_q, _current_r,
_current_m2;
.extern    _current_oa, _current_qa;
.extern          _current_ar, _current_qr, _current_am, _current_qm,
_current_rm; //low pass filtered cross products
.extern          _previous_a, _previous_r;
     /*previous first mode value, for phase shift filter use */
.extern               _shifted_a, _previous_shifted_a;
.extern               _shifted_r, _previous_shifted_r;
.extern               _current_shifted_rm;
.extern               _second_2f_control,
_second_forcebalance_control;
.extern               _current_E1, _current_E2, _current_E3,
_current_E4, _current_E5R, _current_E5I;

.global               _Left_Channel_In1;
.global               _Right_Channel_In1;
.global               _Left_Channel_In2;
.global               _Right_Channel_In2;

.global               _Left_Channel_Out1;
.global               _Right_Channel_Out1;
.global               _Left_Channel_Out2;
.global               _Right_Channel_Out2;
.global               _Left_Channel_Out3;
.global               _Right_Channel_Out3;
.global               _Left_Channel_Out4;
.global               _Right_Channel_Out4;

.extern               _rx1a_buf;
.extern               _tx0a_buf;
.extern               _tx0b_buf;

//defined by Huzx, to store sampled drive, response and trnsformed
data
.extern    _digi_a;
.extern    _digi_q;
.extern          _buffer_oa;
.extern          _buffer_qa;

.extern          _buffer_a;
.extern          _buffer_q;
.extern          _buffer_r;
.extern               _buffer_m2;
.extern               _buffer_ar;
.extern               _buffer_qr;
.extern               _buffer_am;
.extern               _buffer_qm;
.extern               _buffer_rm;
```

```
.extern          _buffer_shifted_rm;   /*store phase shifted first
mode response signal*/

.extern          _beta;          //parameter of allpass phase shift,
.extern               _beta_90;
.extern               _beta_2f;

.extern    _square_drive, _square_response_f, _square_response_s;
.extern          _amp_orthogonal;
.extern               _amp_drive;
.extern               _amp_response_f;
.extern               _amp_response_s;
.extern          _amp_response_s_inphase, _amp_response_s_quadrature;
.extern          _cos_phase;

.extern               _fb_control_i, _fb_control_q;
.extern               _Gain_feedback;
.extern               _Gain_DirectTerm, _Gain_CrossTerm;
.extern               _reconstr_f, _reconstr_s;
     //reconstructed primary/secondary responses
.extern          _reconstr_vel_f, _reconstr_vel_s;
     //reconstructed velocity
.extern          _feedback_f, _feedback_s;
.extern               _delta;

//the FIR low pass filter coefficients are stored in the program
memory
.section /pm seg_pmda;
.var             lowpass[75] = "Gyrolowpass.dat";
.var             bandpass[75] = "Gyrobandpass.dat";

.section/pm seg_pmco;
//.section/pm seg_swco;

_Receive_ADC_Samples:
.global _Receive_ADC_Samples;

     dm(TEMP_M5) = M5;
     dm(TEMP_M1) = I5;
     dm(TEMP_M2) = M6;
     dm(TEMP_I6) = I6;     //I6 must be protected!!!
     dm(TEMP_L5) = L5;

//************************************************************
// store sampled drive signal into circular buffer (_buffer_a),
// use bandpass filter.
//************************************************************
     r1 = -31;
     r0 = dm(_rx1a_buf + Internal_ADC_L1); f0 = float r0 by r1;
     B5 = DM(aBuffer_B_Reg);
     I5 = DM(aBuffer_I_Reg);
     L5 = DM(aBuffer_L_Reg);
     M5 = DM(aBuffer_M_Reg);
     dm(I5, m5) = r0;
     DM(aBuffer_B_Reg) = B5;
     DM(aBuffer_I_Reg) = I5;
```

```
      DM(aBuffer_L_Reg) = L5;
      DM(aBuffer_M_Reg) = M5;


      I8 = bandpass;                    //coefficents stored in
program memory, addressed by DAG2
      m8 = 1;                                 //make sure the same size
of coeffient array with the data array

      f12 = 0;
      f2 = dm(I5, M5), f4 = pm(I8, M8);     //I5 still points to the
oldest data, fine as the filter is symmetrical
      lcntr = @bandpass-1, do ta until lce;
ta:   f8 = f2*f4, f12 =f8+f12, f2 =dm(I5, M5), f4 = pm(I8,M8);
      f8 = f2*f4;
      f12 = f8+f12;
      dm(_current_a) = f12;      // bandpass filtered drive signal


      dm(_current_a) = f0;  //disable bandpass------------

// ------------------to measure drive signal---------------------
      r0 = dm(_current_digi_a);
      r1 = dm(_current_a);
      f0 = f0*f1;                //this is the new cross product in
r0!

      B5 = DM(oaBuffer_B_Reg);
      I5 = DM(oaBuffer_I_Reg);   //I register always point to the
oldest data
      L5 = DM(oaBuffer_L_Reg);
      M5 = DM(oaBuffer_M_Reg);
      dm(I5, m5) = r0;           //first push the new product in
buffer!!!
      DM(oaBuffer_B_Reg) = B5;
      DM(oaBuffer_I_Reg) = I5;
      DM(oaBuffer_L_Reg) = L5;
      DM(oaBuffer_M_Reg) = M5 ;

      I8 = lowpass;                     //coefficents stored in
program memory, addressed by DAG2
      m8 = 1;                                 //make sure the same size
of coeffient array with the data array

      f12 = 0;
      f2 = dm(I5, M5), f4 = pm(I8, M8);
      lcntr = @lowpass-1, do toa until lce;
toa:  f8 = f2*f4, f12 =f8+f12, f2 =dm(I5, M5), f4 = pm(I8,M8);
      f8 = f2*f4;
      f12 = f8+f12;
      dm(_current_oa) = f12;           //filtered cross product of
response and quadrature

      //calcualte qa
      r0 = dm(_current_digi_q);
      r1 = dm(_current_a);
```

```
      f0 = f0*f1;                //this is the new cross product in
r0!

      B5 = DM(qaBuffer_B_Reg);
      I5 = DM(qaBuffer_I_Reg);   //I register always point to the
oldest data
      L5 = DM(qaBuffer_L_Reg);
      M5 = DM(qaBuffer_M_Reg);
      dm(I5, m5) = r0;           //first push the new product in
buffer!!!
      DM(qaBuffer_B_Reg) = B5;
      DM(qaBuffer_I_Reg) = I5;
      DM(qaBuffer_L_Reg) = L5;
      DM(qaBuffer_M_Reg) = M5 ;

      I8 = lowpass;                     //coefficents stored in
program memory, addressed by DAG2
      m8 = 1;                                 //make sure the same size
of coeffient array with the data array

      f12 = 0;
      f2 = dm(I5, M5), f4 = pm(I8, M8);
      lcntr = @lowpass-1, do tqa until lce;
tqa:  f8 = f2*f4, f12 =f8+f12, f2 =dm(I5, M5), f4 = pm(I8,M8);
      f8 = f2*f4;
      f12 = f8+f12;
      dm(_current_qa) = f12;           //filtered cross product of
response and quadrature

      //calculate I^2 + Q^2
      f12 = f12 *f12;
      f2 = dm(_current_oa);
      f2 = f2*f2;
      f2 = f2+f12;
      dm(_square_drive) = f2;

//*********************************************************
//store first mode response, apply bandpass filter
//*********************************************************
      r1 = -31;
      r0 = dm(_rx1a_buf + Internal_ADC_L2); f0 = float r0 by r1;
      B5 = DM(rBuffer_B_Reg);
      I5 = DM(rBuffer_I_Reg);
      L5 = DM(rBuffer_L_Reg);
      M5 = DM(rBuffer_M_Reg);
      dm(I5, m5) = r0;
      DM(rBuffer_B_Reg) = B5;
      DM(rBuffer_I_Reg) = I5;
      DM(rBuffer_L_Reg) = L5;
      DM(rBuffer_M_Reg) = M5;


      I8 = bandpass;                    //coefficents stored in
program memory, addressed by DAG2
      m8 = 1;                                 //make sure the same size
of coeffient array with the data array
```

```
      f12 = 0;
      f2 = dm(I5, M5), f4 = pm(I8, M8);     //I5 still points to the
oldest data, it is fine as the filter is symmetrical
      lcntr = @bandpass-1, do tr until lce;
tr:   f8 = f2*f4, f12 =f8+f12, f2 =dm(I5, M5), f4 = pm(I8,M8);
      f8 = f2*f4;
      f12 = f8+f12;
      dm(_current_r) = f12;      //bandpass filtered response


      dm(_current_r) = f0;  //disable bandpass---------

//*****************************************************************
*****************
//----------phase shift first mode response;2010-----------
// instead of using shifted first mode response for the phase
sensitive detection
// it should be better by using digital unit vector, that will lead
to low noise, 2011
//still use the same name "_shifted_r", it is unit amplitude
//no need, in-phase and quadrature will be calcualted from I and Q
by rotation
//*****************************************************************
*****************
/*
      f0 = dm(_current_r);
      f2 = dm(_previous_r);      //retrieve previous value
      f1 = dm(_beta);                  //_beta is modified in main.c
      f4 = f1*f0;
      f0 = f4 - f2;

      f4 = dm(_previous_shifted_r);
      f2 = f1*f4;
      f1 =f0 + f2;
      dm(_shifted_r) = f1;

      f0 = dm(_current_r);       //update previous values
      dm(_previous_r) = f0;
      f4 = dm(_shifted_r);
      dm(_previous_shifted_r) = f4;
      */

//-------------------------------------------------------

//*****************************************************************
******
//---phase shift original 2f signal, aim to amplify coriolis
response;---
//*****************************************************************
******
/*
      f0 = dm(Original_2f);
      f2 = dm(previous_Original_2f);
      f1 = dm(_beta_2f);
      f4 = f1*f0;
```

```
      f0 = f4 - f2;

      f4 = dm(previous_shifted_Orginal_2f);
      f2 = f1*f4;
      f1 =f0 + f2;
      dm(shifted_Original_2f) = f1;

      f0 = dm(Original_2f);
      dm(previous_Original_2f) = f0;
//    f4 = dm(shifted_Original_2f);
//    dm(previous_shifted_Orginal_2f) = f4;


      f0 = dm(shifted_Original_2f);              //phase shift the
shifted 2f signal: shifted_original_2f again
      f2 = dm(previous_shifted_Orginal_2f);
      f1 = dm(_beta_2f);
      f4 = f1*f0;
      f0 = f4 - f2;

      f4 = dm(previous_shifted_2f);
      f2 = f1*f4;
      f1 =f0 + f2;
      dm(shifted_2f) = f1;

      f0 = dm(shifted_Original_2f);
      dm(previous_shifted_Orginal_2f) = f0;
      f4 = dm(shifted_2f);
      dm(previous_shifted_2f) = f4;
      */

//*****************************************************************
//store second mode response from channel R2, apply bandpass filter
//*****************************************************************

      r1 = -31;
      r0 = dm(_rx1a_buf + Internal_ADC_R2); f0 = float r0 by r1;
      B5 = DM(m2Buffer_B_Reg);
      I5 = DM(m2Buffer_I_Reg);
      L5 = DM(m2Buffer_L_Reg);
      M5 = DM(m2Buffer_M_Reg);
      dm(I5, m5) = r0;
      DM(m2Buffer_B_Reg) = B5;
      DM(m2Buffer_I_Reg) = I5;
      DM(m2Buffer_L_Reg) = L5;
      DM(m2Buffer_M_Reg) = M5;


      I8 = bandpass;                    //coefficents stored in
program memory, addressed by DAG2
      m8 = 1;                                 //make sure the same size
of coeffient array with the data array

      f12 = 0;
      f2 = dm(I5, M5), f4 = pm(I8, M8);     //I5 still points to the
oldest data, it is fine as the filter is symmetrical
```

```
      lcntr = @bandpass-1, do tm2 until lce;
tm2:  f8 = f2*f4, f12 =f8+f12, f2 =dm(I5, M5), f4 = pm(I8,M8);
      f8 = f2*f4;
      f12 = f8+f12;
      dm(_current_m2) = f12;           //bandpass filtered second
mode response


      dm(_current_m2) = f0; //disable bandpass----------------

// ***********************************************
// orthorgonal demodulation of first mode response.
// ***********************************************
      r0 = dm(_current_digi_a);
      r1 = dm(_current_r);
      f0 = f0*f1;                //this is the new cross product in
r0!

//---low pass filter it and store it into the circular buffer
(_buffer_ar)
      B5 = DM(arBuffer_B_Reg);
      I5 = DM(arBuffer_I_Reg);   //I register always point to the
oldest data
      L5 = DM(arBuffer_L_Reg);
      M5 = DM(arBuffer_M_Reg);
      dm(I5, m5) = r0;           //first push the new product in
buffer!!!
      DM(arBuffer_B_Reg) = B5;
      DM(arBuffer_I_Reg) = I5;
      DM(arBuffer_L_Reg) = L5;
      DM(arBuffer_M_Reg) = M5 ;

      I8 = lowpass;                    //coefficents stored in
program memory, addressed by DAG2
      m8 = 1;                                //make sure the same size
of coeffient array with the data array

      f12 = 0;
      f2 = dm(I5, M5), f4 = pm(I8, M8);     //I5 still points to the
oldest data, it is fine as the filter is symmetrical
      lcntr = @lowpass-1, do tar until lce;
tar:  f8 = f2*f4, f12 =f8+f12, f2 =dm(I5, M5), f4 = pm(I8,M8);
      f8 = f2*f4;
      f12 = f8+f12;
      dm(_current_ar) = f12;           //filtered cross product value
of response and drive

// calcualte multiplications of quadrature with response, vector
product.
      r0 = dm(_current_digi_q);
      r1 = dm(_current_r);
      f0 = f0*f1;                //this is the new cross product in
r0!

//---low pass filter it and store it into the circular buffer
(_buffer_qr)
```

```
      B5 = DM(qrBuffer_B_Reg);
      I5 = DM(qrBuffer_I_Reg);    //I register always point to the
oldest data
      L5 = DM(qrBuffer_L_Reg);
      M5 = DM(qrBuffer_M_Reg);
      dm(I5, m5) = r0;            //first push the new product in
buffer!!!
      DM(qrBuffer_B_Reg) = B5;
      DM(qrBuffer_I_Reg) = I5;
      DM(qrBuffer_L_Reg) = L5;
      DM(qrBuffer_M_Reg) = M5 ;

      I8 = lowpass;                      //coefficents stored in
program memory, addressed by DAG2
      m8 = 1;                                 //make sure the same size
of coeffient array with the data array

      f12 = 0;
      f2 = dm(I5, M5), f4 = pm(I8, M8);
      lcntr = @lowpass-1, do tqr until lce;
tqr:  f8 = f2*f4, f12 =f8+f12, f2 =dm(I5, M5), f4 = pm(I8,M8);
      f8 = f2*f4;
      f12 = f8+f12;
      dm(_current_qr) = f12;           //filtered cross product of
response and quadrature


      //calculate I^2 + Q^2
      f12 = f12 *f12;
      f2 = dm(_current_ar);
      f2 = f2*f2;
      f2 = f2+f12;
      dm(_square_response_f) = f2;
//----------------------------

// ************************************************
// orthorgonal demodulation of second mode response.
// ************************************************
      r0 = dm(_current_digi_a);
      r1 = dm(_current_m2);
      f0 = f0*f1;                 //this is the new cross product in
r0!

//---low pass filter it and store it into the circular buffer
(_buffer_qr)
      B5 = DM(amBuffer_B_Reg);
      I5 = DM(amBuffer_I_Reg);    //I register always point to the
oldest data
      L5 = DM(amBuffer_L_Reg);
      M5 = DM(amBuffer_M_Reg);
      dm(I5, m5) = r0;            //first push the new product in
buffer!!!
      DM(amBuffer_B_Reg) = B5;
      DM(amBuffer_I_Reg) = I5;
      DM(amBuffer_L_Reg) = L5;
      DM(amBuffer_M_Reg) = M5 ;
```

```
      I8 = lowpass;                     //coefficents stored in
program memory, addressed by DAG2
      m8 = 1;                                 //make sure the same size
of coeffient array with the data array

      f12 = 0;
      f2 = dm(I5, M5), f4 = pm(I8, M8);
      lcntr = @lowpass-1, do tam until lce;
tam:  f8 = f2*f4, f12 =f8+f12, f2 =dm(I5, M5), f4 = pm(I8,M8);
      f8 = f2*f4;
      f12 = f8+f12;
      dm(_current_am) = f12;            //filtered cross product of
response and quadrature

// calcualte multiplications of quadrature with response, vector
product.
      r0 = dm(_current_digi_q);
      r1 = dm(_current_m2);
      f0 = f0*f1;                 //this is the new cross product in
r0!

//---low pass filter it and store it into the circular buffer
(_buffer_qr)
      B5 = DM(qmBuffer_B_Reg);
      I5 = DM(qmBuffer_I_Reg);    //I register always point to the
oldest data
      L5 = DM(qmBuffer_L_Reg);
      M5 = DM(qmBuffer_M_Reg);
      dm(I5, m5) = r0;            //first push the new product in
buffer!!!
      DM(qmBuffer_B_Reg) = B5;
      DM(qmBuffer_I_Reg) = I5;
      DM(qmBuffer_L_Reg) = L5;
      DM(qmBuffer_M_Reg) = M5 ;

      I8 = lowpass;                     //coefficents stored in
program memory, addressed by DAG2
      m8 = 1;                                 //make sure the same size
of coeffient array with the data array

      f12 = 0;
      f2 = dm(I5, M5), f4 = pm(I8, M8);
      lcntr = @lowpass-1, do tqm until lce;
tqm:  f8 = f2*f4, f12 =f8+f12, f2 =dm(I5, M5), f4 = pm(I8,M8);
      f8 = f2*f4;
      f12 = f8+f12;
      dm(_current_qm) = f12;            //filtered cross product of
response and quadrature

      //calculate I^2 + Q^2
      f12 = f12 *f12;
      f2 = dm(_current_am);
      f2 = f2*f2;
      f2 = f2+f12;
      dm(_square_response_s) = f2;
```

```
// ******************************************************
// this is the phase sensitive demodualtion-------------
// ******************************************************
// calculate multiplication of second mode response with shifted
first mode //response, vector product, to measure the in phase and
quadrature value of the //second mode first, shift the first mode
response, so that it forms 90 degrees with //the quadrature (when
the gyro is in static)
      r0 = dm(_shifted_r);
      r1 = dm(_current_m2);
      f0 = f0*f1;

//---low pass filter it and store
      B5 = DM(rBuffer_shifted_rm_B_Reg);
      I5 = DM(rBuffer_shifted_rm_I_Reg);    //I register always point
to the oldest data
      L5 = DM(rBuffer_shifted_rm_L_Reg);
      M5 = DM(rBuffer_shifted_rm_M_Reg);
      dm(I5, m5) = r0;           //first push the new product in
buffer!!!
      DM(rBuffer_shifted_rm_B_Reg) = B5;
      DM(rBuffer_shifted_rm_I_Reg) = I5;
      DM(rBuffer_shifted_rm_L_Reg) = L5;
      DM(rBuffer_shifted_rm_M_Reg) = M5;

      I8 = lowpass;                     //coefficents stored in
program memory, addressed by DAG2
      m8 = 1;                                //make sure the same size
of coeffient array with the data array

      f12 = 0;
      f2 = dm(I5, M5), f4 = pm(I8, M8);
      lcntr = @lowpass-1, do shiftrm until lce;
shiftrm:   f8 = f2*f4, f12 =f8+f12, f2 =dm(I5, M5), f4 = pm(I8,M8);
      f8 = f2*f4;
      f12 = f8+f12;
      dm(_current_shifted_rm) = f12;
*/

//
*********************************************************************
*****************
// second mode force rebalance control: use the created unit digital
orthogonal pair,
// and control outputs from measured _amp_response_s_inphase,
_amp_response_s_quadrature,
// to generate a sine wave (possibly need phase compensation) to
balance the second mode
//
*********************************************************************
*****************
      //r0 = dm(_aligned_digi_a);
      //r1 = dm(_aligned_digi_q);
```

```
      r0 = dm(_current_digi_a);
      r1 = dm(_current_digi_q);

      f2 = dm(_fb_control_i);
      f4 = dm(_fb_control_q);

      f2 = f2*f0;
      f4 = f4*f1;
      f12 = f2+f4;

      dm(_second_forcebalance_control) = f12;
//---------------------------------------

//
*****************************************************************
*********************************
// reconstructed primary mode response (displacement), multiplied
with a feedback gain ( between [-5, 5])
// used to modify the resonator dynamics, mainly the resonant
frequency aiming at mode tuning
//
*****************************************************************
********************
      f2 = dm(_current_ar);
      f4 = dm(_current_qr);

      //displacement feedback
      f2 = f2*f0;
      f4 = f4*f1;
      f12 = f2+f4;

      dm(_reconstr_f) = f12;           // save reconstructed primary
displacement

      //velocity feedback         //Jan. 2012 to try velocity
feedback to improve Q factor of primary mode
      //f2 = f2*f1;
      //f4 = f4*f0;
      //f12 = f2-f4;

      f2 = dm(_current_am);
      f4 = dm(_current_qm);

      f2 = f2*f0;
      f4 = f4*f1;
      f12 = f2+f4;

      dm(_reconstr_s) = f12;           // save reconstructed
secondary response

// ---------------------------------------


//
*****************************************************************
****************************
```

```
// create parametric signal from I_2f, Q_2f; that should follow
phase of the resultant primary drive
//
*************************************************************************
****************************
/*
      r0 = dm(_digi_2f_a);
      r1 = dm(_digi_2f_q);

      f2 = dm(_I_2f);
      f4 = dm(_Q_2f);

      f2 = f2*f0;
      f4 = f4*f1;
      f12 = f2+f4;

      f2 = dm(_Gain_Sec_2f);
      f12 = f12 * f2;

      dm(Parametric_drive) = f12;
      */
//----------------------------------------


      M5 = dm(TEMP_M5);
      I5 = dm(TEMP_M1);
      m6 = dm(TEMP_M2);
      I6 = dm(TEMP_I6);
      L5 = dm(TEMP_L5);

      leaf_exit;
_Receive_ADC_Samples.end:


_Transmit_DAC_Samples:
.global _Transmit_DAC_Samples;

      r1 = 31;

//    I5 = DM(m2Buffer_I_Reg);
//    r0 = dm(I5, 0);
//    r0 = dm(_second_forcebalance_control);
//    r0 = dm(_shifted_r);
//    r0 = trunc f0 by r1; dm(_tx0b_buf + Internal_DAC_R4) = r0;

//    I5 = DM(arBuffer_I_Reg);
//    r0 = dm(I5, 0);
//    f0 = dm(_amp_response_s_inphase);
//    r0 = trunc f0 by r1; dm(_tx0b_buf + Internal_DAC_L4) = r0;

// calculate and output full displacement feedback for tuning
      f0 = dm(_reconstr_f);
      f1 = dm(_reconstr_s);

      f2 = dm(_Gain_DirectTerm);
      f4 = dm(_Gain_CrossTerm);
```

```
      f2 = f2*f0;
      f4 = f4*f1;
      f12 = f2+f4;
      dm(_feedback_f) = f12;           //L3, feedabck to primary mode

      f2 = dm(_Gain_DirectTerm);
      f4 = dm(_Gain_CrossTerm);
      f12 = f4*f0;
      dm(_feedback_s) = f12;           //R3, feedback to secondary
mode

      r1 = 31;
      f0 = dm(_feedback_f);
      r0 = trunc f0 by r1; dm(_tx0b_buf + Internal_DAC_L3) = r0;
      //be careful here, L3/R3 use tx0b_buf
      f0 = dm(_feedback_s);
      r0 = trunc f0 by r1; dm(_tx0b_buf + Internal_DAC_R3) = r0;


#ifdef GENERATE_DAC_PURE_TONES_TEST
      Call make_DAC_Pure_Tones;
#endif

      leaf_exit;
_Transmit_DAC_Samples.end:

//initialize the buffer pointers
_BufferInit:
.global _BufferInit;

      DM(TEMP_L5) = L5;     //protect the preserved register

//buffer for digitally created orthogonal pair, hopefuly it will
imporve accuracy
      B5 = _digi_a;
      I5 = _digi_a;
      L5 = @_digi_a;
      M4 = 1;
      DM(digiaBuffer_B_Reg) = B5;
      DM(digiaBuffer_I_Reg) = I5;
      DM(digiaBuffer_L_Reg) = L5;
      DM(digiaBuffer_M_Reg) = M4;

      B5 = _digi_q;
      I5 = _digi_q;
      L5 = @_digi_q;
      DM(digiqBuffer_B_Reg) = B5;
      DM(digiqBuffer_I_Reg) = I5;
      DM(digiqBuffer_L_Reg) = L5;
      DM(digiqBuffer_M_Reg) = M4;

// buffer for drive and its orthogonal counterpart
      B5 = _buffer_a;
      I5 = _buffer_a;
      L5 = @_buffer_a;
```

```
      M4 = 1;
      DM(aBuffer_B_Reg) = B5;
      DM(aBuffer_I_Reg) = I5;
      DM(aBuffer_L_Reg) = L5;
      DM(aBuffer_M_Reg) = M4;

      B5 = _buffer_q;
      I5 = _buffer_q;
      L5 = @_buffer_q;
      DM(qBuffer_B_Reg) = B5;
      DM(qBuffer_I_Reg) = I5;
      DM(qBuffer_L_Reg) = L5;
      DM(qBuffer_M_Reg) = M4;

      B5 = _buffer_r;
      I5 = _buffer_r;
      L5 = @_buffer_r;
      DM(rBuffer_B_Reg) = B5;
      DM(rBuffer_I_Reg) = I5;
      DM(rBuffer_L_Reg) = L5;
      DM(rBuffer_M_Reg) = M4;

//buffer for the phase shifted first mode response signal,
//will use for phase sensitive demodualtion of the second mode in
phase and quadrature signals
      B5 = _buffer_shifted_rm;
      I5 = _buffer_shifted_rm;
      L5 = @_buffer_shifted_rm;
      DM(rBuffer_shifted_rm_B_Reg) = B5;
      DM(rBuffer_shifted_rm_I_Reg) = I5;
      DM(rBuffer_shifted_rm_L_Reg) = L5;
      DM(rBuffer_shifted_rm_M_Reg) = M4;

      B5 = _buffer_m2;
      I5 = _buffer_m2;
      L5 = @_buffer_m2;
      DM(m2Buffer_B_Reg) = B5;
      DM(m2Buffer_I_Reg) = I5;
      DM(m2Buffer_L_Reg) = L5;
      DM(m2Buffer_M_Reg) = M4;

//to meassure drive signal
      B5 = _buffer_oa;
      I5 = _buffer_oa;
      L5 = @_buffer_oa;
      DM(oaBuffer_B_Reg) = B5;
      DM(oaBuffer_I_Reg) = I5;
      DM(oaBuffer_L_Reg) = L5;
      DM(oaBuffer_M_Reg) = M4;

      B5 = _buffer_qa;
      I5 = _buffer_qa;
      L5 = @_buffer_qa;
      DM(qaBuffer_B_Reg) = B5;
      DM(qaBuffer_I_Reg) = I5;
      DM(qaBuffer_L_Reg) = L5;
```

```
      DM(qaBuffer_M_Reg) = M4;

//to measure first mode response
      B5 = _buffer_ar;
      I5 = _buffer_ar;
      L5 = @_buffer_ar;
      DM(arBuffer_B_Reg) = B5;
      DM(arBuffer_I_Reg) = I5;
      DM(arBuffer_L_Reg) = L5;
      DM(arBuffer_M_Reg) = M4;

      B5 = _buffer_qr;
      I5 = _buffer_qr;
      L5 = @_buffer_qr;
      DM(qrBuffer_B_Reg) = B5;
      DM(qrBuffer_I_Reg) = I5;
      DM(qrBuffer_L_Reg) = L5;
      DM(qrBuffer_M_Reg) = M4;

//to measure second mode response
      B5 = _buffer_am;
      I5 = _buffer_am;
      L5 = @_buffer_am;
      DM(amBuffer_B_Reg) = B5;
      DM(amBuffer_I_Reg) = I5;
      DM(amBuffer_L_Reg) = L5;
      DM(amBuffer_M_Reg) = M4;

      B5 = _buffer_qm;
      I5 = _buffer_qm;
      L5 = @_buffer_qm;
      DM(qmBuffer_B_Reg) = B5;
      DM(qmBuffer_I_Reg) = I5;
      DM(qmBuffer_L_Reg) = L5;
      DM(qmBuffer_M_Reg) = M4;

      B5 = _buffer_rm;
      I5 = _buffer_rm;
      L5 = @_buffer_rm;
      DM(rmBuffer_B_Reg) = B5;
      DM(rmBuffer_I_Reg) = I5;
      DM(rmBuffer_L_Reg) = L5;
      DM(rmBuffer_M_Reg) = M4;

      L5 = DM(TEMP_L5);

leaf_exit;
_BufferInit.end:


_SinTableInit:
.global _SinTableInit;

      //  Huzx: can use scratch registers, their values don't need to
be perseved and restored
      // this can save some core time. M4, I4, B4, R0, R1, R2, R4
```

```
      // preserve M1 M2 and L5 registers
      DM(TEMP_M1) = M1;
      DM(TEMP_M2) = M2;
      DM(TEMP_L5) = L5;

      // added by Huzx for extended sine wave generation
      BIT SET Mode1 CBUFEN;

      B5=0;
      I5=0;
      L5 = 4000*4096*16;

      // create the I data for the reference signal, initial
frequency set at 14.26kHz
      M1 = 1216931*16;           //1216931, for the drive freq of
14.260khz! 960000;
      DM(Extend1_B_reg) = B5;
      DM(Extend1_I_reg) = I5;
      DM(Extend1_L_reg) = L5;
      DM(_Extend1_M_reg) = M1;

      //create drive phase data               //Required phase offset
to account for electronics
      I5 = 237822862; //0 = 237822862; //22.5 = 254206862; 45 =
8446862; 67.5 = 24830862;
      DM(_Extend1D_I_reg) = I5; //First mode phase
      I5 = 237822862;
      DM(_Extend2D_I_reg) = I5; //Second mode phase

      //create the Q data for the reference signal
      r0 = L5;
      //r1 = lshift r0 by -2;
      //r1 = 12288000*16;   //three quaters of L5, ahead 270 degrees,
that is 90 degrees behind;
      r1 = 4096000*16; //90 ahead
      DM(Extend2_B_reg) = B5;
      DM(Extend2_I_reg) = r1;
      DM(Extend2_L_reg) = L5;
      DM(_Extend2_M_reg) = M1;

      //2f parametric signal,in phase with reference signal, output
via L3
      r0 = M1;
      r1 = lshift r0 by 1;       //double the frequency by double
the M register

      //create the I data for the 2f signal
      DM(Extend3_B_reg) = B5;
      DM(Extend3_I_reg) = I5;
      DM(Extend3_L_reg) = L5;
      DM(_Extend3_M_reg) = r1;    //2f

      //create the Q data
      DM(Extend4_B_reg) = B5;
      DM(Extend4_L_reg) = L5;
```

```
      DM(_Extend4_M_reg) = r1;    //2f

      r1 = 4096000*16;            //90 ahead for the index register
      DM(Extend4_I_reg) = r1;


      M1 = DM(TEMP_M1);
      M2 = DM(TEMP_M2);
      L5 = DM(TEMP_L5);

      leaf_exit;
_SinTableInit.end:


make_DAC_Pure_Tones:
      // use Compiler Scratch Registers for generating sine tones in
assembly
      DM(TEMP_M5) = M5;
      DM(TEMP_L5) = L5;

      R1 = DM(_Extend1_M_reg);    //make sure they definetely the
same value!!
      DM(_Extend2_M_reg) = R1;
      R1 = lshift R1 by 1;
      DM(_Extend3_M_reg) = R1;

//------------create cos(wt) into _current_digi_a-------------------
---------
      B5 = DM(Extend1_B_reg);
      I5 = DM(Extend1_I_reg);
      L5 = DM(Extend1_L_reg);
      M5 = DM(_Extend1_M_reg);

      modify(I5, M5);
      DM(Extend1_I_reg) = I5;
      R0 = I5;
      R1 = LSHIFT R0 by -16;      //-12
      m4 = R1;
      I4=sine4000;
      r4 = dm(m4, i4);

// linear interpolation: using Y0(R4) and Y1(R2), in integer or
fractional format?
// interpolation coefficient in R1(integer format?)
      R0 = m4;
      R0 = R0 +1;
      R1 = 4000;
      R2 = 0;
      comp (R0, R1);
      if EQ R0 = r2;
      m4 = R0;
      R2 = dm(m4, i4);      //read the next value in the sine wave
table

      R0 = I5;
      R1 = FEXT R0 by 0:16; //extract the 16 LSB bits
```

```
      r1 = lshift r1 by 15; //make interpolation coefficient 32 bit,
with sign bit 0 (0~1)

      R0 = R2 - R4;              //Y1-Y0
      R0 = R0 * r1(ssfr);
      R4 = r4 + r0;              //Y0 + k(Y1-Y0)

// store into buffer before adjust its amplitude, as one of the
orthogonal pair
      r1 = -31;
      f0 = float r4 by r1;
      B5 = DM(digiaBuffer_B_Reg);
      I5 = DM(digiaBuffer_I_Reg);
      L5 = DM(digiaBuffer_L_Reg);
      M5 = DM(digiaBuffer_M_Reg);
      dm(I5, m5) = r0;           //post modify with m5, update I5
      DM(digiaBuffer_B_Reg) = B5;
      DM(digiaBuffer_I_Reg) = I5;
      DM(digiaBuffer_L_Reg) = L5;
      DM(digiaBuffer_M_Reg) = M5;

      dm(_current_digi_a) = r0;

//--------------create sin(wt) into _current_digi_q-----------------
------------
      B5 = DM(Extend2_B_reg);
      I5 = DM(Extend2_I_reg);
      L5 = DM(Extend2_L_reg);
      M5 = DM(_Extend2_M_reg);

      modify(I5, M5);
      DM(Extend2_I_reg) = I5;
      R0 = I5;
      R1 = LSHIFT R0 by -16;
      m4 = R1;
      I4=sine4000;
      r4 = dm(m4, i4);

// linear interpolation: using Y0(R4) and Y1(R2), in integer or
fractional format?
// interpolation coefficient in R1(integer format?)
      R0 = m4;
      R0 = R0 +1;
      R1 = 4000;
      R2 = 0;
      comp (R0, R1);
      if EQ R0 = r2;
      m4 = R0;
      R2 = dm(m4, i4);      //read the next value in the sine wave
table

      R0 = I5;
      R1 = FEXT R0 by 0:16; //extract the 16 LSB bits
      r1 = lshift r1 by 15;

      R0 = R2 - R4;              //Y1-Y0
```

```
      R0 = R0 * r1(ssfr);
      R4 = r4 + r0;              //Y0 + k(Y1-Y0)

// store quadrature into buffer before adjust its amplitude,
      r1 = -31;
      f0 = float r4 by r1;
      B5 = DM(digiqBuffer_B_Reg);
      I5 = DM(digiqBuffer_I_Reg);
      L5 = DM(digiqBuffer_L_Reg);
      M5 = DM(digiqBuffer_M_Reg);
      dm(I5, m5) = r0;
      DM(digiqBuffer_B_Reg) = B5;
      DM(digiqBuffer_I_Reg) = I5;
      DM(digiqBuffer_L_Reg) = L5;
      DM(digiqBuffer_M_Reg) = M5;

      dm(_current_digi_q) = r0;

///////ADDED BY SB 12/09/13////////////////////////////////

//------------create modified cos(wt), drive signal through L1------
---
      B5 = DM(Extend1_B_reg);
      I5 = DM(_Extend1D_I_reg);
      L5 = DM(Extend1_L_reg);
      M5 = DM(_Extend1_M_reg);

      modify(I5, M5);
      DM(_Extend1D_I_reg) = I5;
      R0 = I5;
      R1 = LSHIFT R0 by -16;     //-12
      m4 = R1;
      I4=sine4000;
      r4 = dm(m4, i4);

// linear interpolation: using Y0(R4) and Y1(R2), in integer or
fractional format?
// interpolation coefficient in R1(integer format?)
      R0 = m4;
      R0 = R0 +1;
      R1 = 4000;
      R2 = 0;
      comp (R0, R1);
      if EQ R0 = r2;
      m4 = R0;
      R2 = dm(m4, i4);      //read the next value in the sine wave
table

      R0 = I5;
      R1 = FEXT R0 by 0:16; //extract the 16 LSB bits
      r1 = lshift r1 by 15; //make interpolation coefficient 32 bit,
with sign bit 0 (0~1)

      R0 = R2 - R4;              //Y1-Y0
      R0 = R0 * r1(ssfr);
      R4 = r4 + r0;              //Y0 + k(Y1-Y0)
```

```
      r1 = -31;
      f0 = float r4 by r1;

// adjust amplitude, and output to DAC
      r1 = 31;
      f2 = dm(_Gain_1f);
      r0 = fix f2 by r1;          //convert float-point gain into
fractional
//    r0 = 0.05r;
      r2 = r4*r0(ssfr);           //the inputs are signed fractional
      r4 = r2;
      dm(_tx0a_buf + Internal_DAC_L1) = r4;

//--------------create modified sin(wt) output via R1---------------
--
      B5 = DM(Extend2_B_reg);
      I5 = DM(_Extend2D_I_reg);
      L5 = DM(Extend2_L_reg);
      M5 = DM(_Extend2_M_reg);

      modify(I5, M5);
      DM(_Extend2D_I_reg) = I5;
      R0 = I5;
      R1 = LSHIFT R0 by -16;
      m4 = R1;
      I4=sine4000;
      r4 = dm(m4, i4);

// linear interpolation: using Y0(R4) and Y1(R2), in integer or
fractional format?
// interpolation coefficient in R1(integer format?)
      R0 = m4;
      R0 = R0 +1;
      R1 = 4000;
      R2 = 0;
      comp (R0, R1);
      if EQ R0 = r2;
      m4 = R0;
      R2 = dm(m4, i4);      //read the next value in the sine wave
table

      R0 = I5;
      R1 = FEXT R0 by 0:16; //extract the 16 LSB bits
      r1 = lshift r1 by 15;

      R0 = R2 - R4;               //Y1-Y0
      R0 = R0 * r1(ssfr);
      R4 = r4 + r0;               //Y0 + k(Y1-Y0)

      r1 = -31;
      f0 = float r4 by r1;

//    adjust gain, output to DAC
      r1 = 31;
      f2 = dm(_Gain_1s);
```

```
      r0 = fix f2 by r1;         //convert float-point gain into
fractional
//    r0 = 0.05r;
      r2 = r4*r0(ssfr);
      r4 = r2;
      dm(_tx0a_buf + Internal_DAC_R1) = r4;

////////////////////////////////////////////////////////////////

//-------------produce 2f parametric cos(2wt) into _digi_2f_a,
output into L3----------
      B5 = DM(Extend3_B_reg);
      I5 = DM(Extend3_I_reg);
      L5 = DM(Extend3_L_reg);
      M5 = DM(_Extend3_M_reg);

      modify(I5, M5);
      DM(Extend3_I_reg) = I5;
      R0 = I5;
      R1 = LSHIFT R0 by -16;
      m4 = R1;
      I4=sine4000;
      r4 = dm(m4, i4);

// linear interpolation: using Y0(R4) and Y1(R2), in integer or
fractional format?
// interpolation coefficient in R1(integer format?)
      R0 = m4;
      R0 = R0 +1;
      R1 = 4000;
      R2 = 0;
      comp (R0, R1);
      if EQ R0 = r2;
      m4 = R0;
      R2 = dm(m4, i4);      //read the next value in the sine wave
table

      R0 = I5;
      R1 = FEXT R0 by 0:16; //extract the 16 LSB bits
      r1 = lshift r1 by 15;

      R0 = R2 - R4;              //Y1-Y0
      R0 = R0 * r1(ssfr);
      R4 = r4 + r0;              //Y0 + k(Y1-Y0)

//--------extract 2f wave fractional data in r4 into foating point
format--
      r1 = -31;
      r0 = r4;   f0 = float r0 by r1;
      dm(Original_2f) = f0;
      dm(_digi_2f_a) = f0;

      r1 = 31;
      f2 = dm(_Gain_2f);
      r0 = fix f2 by r1;         //convert float-point gain into
fractional
```

```
      r2 = r4*r0(ssfr);
      r4 = r2;
//    dm(_tx0b_buf + Internal_DAC_L3) = r4;

//---------------produce 2f parametric, sin(2wt) into _digi_2f_q----
-------------
      B5 = DM(Extend4_B_reg);
      I5 = DM(Extend4_I_reg);
      L5 = DM(Extend4_L_reg);
      M5 = DM(_Extend4_M_reg);

      modify(I5, M5);
      DM(Extend4_I_reg) = I5;
      R0 = I5;
      R1 = LSHIFT R0 by -16;
      m4 = R1;
      I4=sine4000;
      r4 = dm(m4, i4);

// linear interpolation: using Y0(R4) and Y1(R2), in integer or
fractional format?
// interpolation coefficient in R1(integer format?)
      R0 = m4;
      R0 = R0 +1;
      R1 = 4000;
      R2 = 0;
      comp (R0, R1);
      if EQ R0 = r2;
      m4 = R0;
      R2 = dm(m4, i4);      //read the next value in the sine wave
table

      R0 = I5;
      R1 = FEXT R0 by 0:16; //extract the 16 LSB bits
      r1 = lshift r1 by 15;

      R0 = R2 - R4;               //Y1-Y0
      R0 = R0 * r1(ssfr);
      R4 = r4 + r0;               //Y0 + k(Y1-Y0)

//--------extract 2f wave fractional data in r4 into foating point
format--
      r1 = -31;
      r0 = r4;   f0 = float r0 by r1;
      dm(_digi_2f_q) = f0;
//-------------------------------------------------------------------
-------

      M5 = DM(TEMP_M5) ;
      L5 = DM(TEMP_L5);

      RTS;

Make_DAC_Pure_Tones.end:
```

Chapter 11. References

1. Moskowitz, S., *The Development of the Artificial Horizon for Celestial Navigation.* Journal of the Institute of Navigation, 1973. **20**(1): p. 1 - 16.
2. Wrigley, W., *The History of Inertial Navigation.* Journal of Navigation, 1977. **30**(1): p. 61-68.
3. Caron, F., *Of gyroscopes and gaming: The tech behind the Wii MotionPlus*, in *Ars Technica*. 2008.
4. Nield, D., *How Occulus Rift works: Everything you need to know about the VR sensation*, in *Wareable*. 2015.
5. Greenberg, A., *The gyroscopes in your phone could let apps eavesdrop on conversations*, in *Wired*. 2014.
6. Torunbalci, M.M., et al., *Comparison of Two Alternative Silicon-on-Glass Microfabrication Processes for MEMS Inertial Sensors*, in *Eurosensors XXV*. 2011: Athens, Greece.
7. Klaassen, E.H., et al., *Silicon fusion bonding and deep reactive ion etching: A new technology for microstructures.* Sensors and Actuators a-Physical, 1996. **52**(1-3): p. 132-139.
8. Sensing, S. *MEMS Gyroscope*. 2014; Available from: http://www.siliconsensing.com/technology/mems-gyroscope/.
9. Acar, C. and A. Shkel, *MEMS Vibratory Gyroscopes: Structural Approaches to Improve Robustness*. 2009: Springer. 1-256.
10. Gallacher, B.J., et al., *Principles of a Three-Axis Vibrating Gyroscope.* Ieee Transactions on Aerospace and Electronic Systems, 2001. **37**(4): p. 1333-1343.
11. Gallacher, B.J., *Principles of a Micro-Rate Integrating Ring Gyroscope.* Ieee Transactions on Aerospace and Electronic Systems, 2012. **48**(1): p. 658-672.
12. Rozelle, D.M. *The Hemispherical Resonator Gyro: From Wineglass to the Planets*.
13. Bryan, H.G., *On the beats in the vibrations of a revolving cylinder or bell.* Proceedings of the Cambridge Philosophical Society, 1890. **7**(1).
14. Sharma, A., et al. *A high-Q in-plane SOI tuning fork gyroscope*. in *Sensors, 2004. Proceedings of IEEE*. 2004.
15. Loper, E.J. and D.D. Lynch, *Vibratory Rotation Sensor*. 1990: United States.
16. Piyabongkarn, D., R. Rajamani, and M. Greminger, *The development of a MEMS gyroscope for absolute angle measurement.* Control Systems Technology, IEEE Transactions on, 2005. **13**(2): p. 185-195.
17. Prikhodko, I.P., et al., *Foucault pendulum on a chip: Rate integrating silicon MEMS gyroscope.* Sensors and Actuators a-Physical, 2012. **177**: p. 67-78.
18. Georgy, J., et al., *Modeling the Stochastic Drift of a MEMS-Based Gyroscope in Gyro/Odometer/GPS Integrated Navigation.* Intelligent Transportation Systems, IEEE Transactions on, 2010. **11**(4): p. 856-872.
19. Friedland, B. and M.F. Hutton, *Theory and Error Analysis of Vibrating-Member Gyroscope.* IEEE Transactions on Automatic Control, 1978. **23**(4): p. 545-556.
20. Lynch, D.D., *Vibratory Gyro Analysis by the Method of Averaging*, in *II St Petersburg International Conference in Gyroscopic Technology and Navigation*. 1995: St Petersburg. p. 18-26.
21. Painter, C.C. and A.M. Shkel, *Active structural error suppression in MEMS vibratory rate integrating gyroscopes.* Ieee Sensors Journal, 2003. **3**(5): p. 595-606.
22. Gallacher, B.J., et al., *Electrostatic correction of structural imperfections present in a microring gyroscope.* Journal of Microelectromechanical Systems, 2005. **14**(2): p. 221-234.

23. Dong Joon, K. and R.T. M'Closkey, *A systematic method for tuning the dynamics of electrostatically actuated vibratory gyros.* Control Systems Technology, IEEE Transactions on, 2006. **14**(1): p. 69-81.
24. Hu, Z.X., et al. *Precision mode matching of MEMS gyroscope by feedback control*. in *Sensors, 2011 IEEE*. 2011.
25. Xiaolei, W., et al. *Research and experiment on the drive frequency control of the MEMS gyroscope*. in *Mechanic Automation and Control Engineering (MACE), 2011 Second International Conference on*. 2011.
26. IEEE, *IEEE Standard Specification Format Guide and Test Procedure for Coriolis Vibratory Gyros*. 2004.
27. Lawrence, A., *Modern Inertial Technology: Navigation, Guidance and Control*. 1998, New York: Springer.
28. Grewal, M. and A. Andrews, *How Good is Your Gyro?*, in *IEEE Control Systems Magazine*. 2010.
29. Prikhodko, I.P., et al. *Sub-degree-per-hour silicon MEMS rate sensor with 1 million Q-factor*. in *Solid-State Sensors, Actuators and Microsystems Conference (TRANSDUCERS), 2011 16th International*. 2011.
30. Alper, S.E., Y. Temiz, and T. Akin, *A Compact Angular Rate Sensor System Using a Fully Decoupled Silicon-on-Glass MEMS Gyroscope.* Journal of Microelectromechanical Systems, 2008. **17**(6): p. 1418-1429.
31. Zaman, M.F., et al., *A Mode-Matched Silicon-Yaw Tuning-Fork Gyroscope With Subdegree-Per-Hour Allan Deviation Bias Instability.* Journal of Microelectromechanical Systems, 2008. **17**(6): p. 1526-1536.
32. Park, S., R. Horowitz, and C.-W. Tan, *Dynamics and control of a MEMS angle measuring gyroscope.* Sensors and Actuators A: Physical, 2008. **144**(1): p. 56-63.
33. Tatar, E., S.E. Alper, and T. Akin, *Quadrature-Error Compensation and Corresponding Effects on the Performance of Fully Decoupled MEMS Gyroscopes.* Journal of Microelectromechanical Systems, 2012. **21**(3): p. 656-667.
34. Gregory, J.A., J. Cho, and K. Najafi. *Novel mismatch compensation methods for rate-integrating gyroscopes*. in *Position Location and Navigation Symposium (PLANS), 2012 IEEE/ION*. 2012.
35. Painter, C.C. and A.M. Shkel, *Structural and thermal modeling of a z -axis rate integrating gyroscope.* Journal of Micromechanics and Microengineering, 2003. **13**(2): p. 229.
36. Guan, Y., et al., *Acceleration sensitivity of tuning fork gyroscopes: theoretical model, simulation and experimental verification.* Microsystem Technologies, 2014: p. 1-11.
37. Gallacher, B.J., J.S. Burdess, and K.M. Harish, *A control scheme for a MEMS electrostatic resonant gyroscope excited using combined parametric excitation and harmonic forcing.* Journal of Micromechanics and Microengineering, 2006. **16**(2): p. 320-331.
38. Sungsu, P. and R. Horowitz, *Adaptive control for the conventional mode of operation of MEMS gyroscopes.* Microelectromechanical Systems, Journal of, 2003. **12**(1): p. 101-108.
39. Yilmaz, E. and D. Bindel. *Effects of imperfections on solid-wave gyroscope dynamics*. in *SENSORS, 2013 IEEE*. 2013.
40. Johnson, R.S., *Singular Perturbation Theory*. 2009: Springer.
41. Agarwal, A. and J. Lang, *Foundations of Analog and Digital Electronic Circuits*. 2005, San Francisco, CA: Morgan Kaufmann.
42. Gregory, J.A., J. Cho, and K. Najafi, *Characterization and control of a high-Q MEMS inertial sensor using low-cost hardware.* 2012 Ieee/Ion Position Location and Navigation Symposium (Plans), 2012.